The Dissertation Committee for Yue Zhu Certifies that this is the approved version of the following dissertation:

Intercalation Chemistry and Charge Storage in Solution-Processed Layered $MOPO_4$ (M = V, Nb) Hydrates

Committee:

Guihua Yu, Supervisor

Arumugam Manthiram

Deji Akinwande

Gyeong S. Hwang

Intercalation Chemistry and Charge Storage in Solution-Processed Layered $MOPO_4$ (M = V, Nb) Hydrates

by

Yue Zhu

Dissertation

Presented to the Faculty of the Graduate School of

The University of Texas at Austin

in Partial Fulfillment

of the Requirements

for the Degree of

Doctor of Philosophy

The University of Texas at Austin

August 2019

Dedication

To my wife Zenian, my daughter Like and our lovely companion Winter.

Acknowledgements

In the aftermath of writing this dissertation, it behooves me to thank all the people who have made it possible for me to complete it. I would like to express my deepest gratitude to my supervisor Prof. Guihua Yu for his strong support, rigorous training and invaluable guidance throughout my entire doctoral study. Most importantly, I truly appreciate the trust he put in me on taking challenging projects, the freedom he granted me in selecting research topics and the patience he showed when I was slow in progress.

I have been very fortunate to pursue my doctoral degree at UT Austin, where I have the chance to meet many outstanding researchers and excellent peers. My sincere thanks go to Prof. Arumugam Manthiram, Prof. Deji Akinwande, and Prof. Gyeong S. Hwang for kindly serving as my committee members, to Prof. Paulo J. Ferreira and Prof. Yuanyue Liu for their important contributions to our collaborated projects, to Prof. Paul S. Ho for his wonderful last class and support on my fellowship application, and to staff members in Texas Materials Institute for their generous help in accessing research facilities. I would also like to extend my thanks to all present and previous lab members in Prof. Yu's group, including three summer undergraduate students from USTC, for all the joy and pain we have shared in the past five years.

Finally, I want to give my special thanks to several people whose names I prefer to keep in my own heart. Although becoming a scientist used to be my vague childhood dream, it is really these people I have been able to know or know about truly inspired me to take this path, whether I shall succeed or fail in the end.

Abstract

Intercalation Chemistry and Charge Storage in Solution-Processed Layered $MOPO_4$ (M = V, Nb) Hydrates

Yue Zhu, Ph.D.

The University of Texas at Austin, 2019

Supervisor: Guihua Yu

Intercalation chemistry, despite being an old field with more than a century of history, has recently gained renewed interest owing to the rise of two-dimensional (2D) nanomaterials and their associated scientific and technological importance. The relevance of intercalation chemistry to this family of materials includes liquid exfoliation of layered materials, tuning their physical and chemical properties by intercalation, charge storage in thin 2D nanosheets, electrochemical intercalation in 2D heterostructures, etc. Some are old topics demanding fresh understanding in new material systems, and some are unprecedented ideas that will be exciting to explore.

This dissertation examines intercalation chemistry and charge storage in layered $MOPO_4$ (M=V, Nb) hydrates, which is an interesting material system that differs in several unique ways from many previously studied intercalation hosts. This system is also less popular in literature compared with classic ones, such as graphite and transition metal dichalcogenides, but is more structurally complicated and offers more research opportunities. Historically, some aspects of the intercalation product and kinetics regarding the use of a bulky metallocene as intercalation guest remain elusive, and the

charge storage mechanism of small alkali-ions in the presence of interlayer water has not been well understood. This work presents research efforts to answer such open questions in these materials through a combined experimental and theoretical approach. Following a brief overview of intercalation chemistry and its most up to date development (Chapter 1), materials synthesis involving solution processing methods to obtain microcrystals and nanosheets of $MOPO_4$ hydrates is described (Chapter 2). The subsequent in-depth studies are divided into two major parts using either microcrystals or nanosheets as intercalation host. The first part discusses the intercalation of ferrocene into microcrystals of $VOPO_4 \cdot 2H_2O$ in terms of resolving intercalated structures and understanding solvent-dependent kinetics (Chapter 3). The second part details the charge storage in nanosheets of $MOPO_4$ with implications on Li- and Na-ion battery applications (Chapter 4). Finally, key contributions to the intercalation chemistry of the title material system are summarized and possible future directions are provided (Chapter 5).

Table of Contents

List of Tables

List of Figures

Chapter 1: Introduction

Intercalation, in chemistry, refers to the reversible insertion of guest molecules into a host while its structural features are conserved.[1] The intercalation reactions are topotactic in nature and the products, the intercalation compounds, should be distinguished from inclusion (guest species are occluded in the host during preparation) and interstitial compounds (additional atoms occupy empty lattice sites of the host structure).[2, 3] The host can be one- to three-dimensional solids, while two-dimensional (2D) structures consisting of layers held together by weak van der Waals forces, such as graphite or transition metal dichalcogenides (TMDs), are ideal objects for intercalation reactions due to the combination of easy access to the interlayer galleries and high stability of the final products.[4] The history of intercalation chemistry began as early as 1840 when Schafhaeutl studied intercalation of graphite in concentrated sulfuric acid.[5] However, it was from about 1970 to 1990 when the greatest development happened in this field. A famous example is the series of key discoveries that crucially contributed to the birth of the lithium-ion batteries (LIBs).[6]

Despite the long history and the past of its golden days, research in intercalation chemistry has continued because of the utilization of intercalation as a preparative tool to construct new artificial materials.[7] Nowadays, revisiting some of its topics has been further promoted by the recent surge of research interests in 2D layered materials following the discovery of graphene.[8, 9] The indispensable roles of intercalation chemistry in the research of 2D layered materials, as shown in Figure 1.1, lie in the following aspects: (1) Large-scale production of ultrathin nanosheets via liquid exfoliation of layered materials generally relies on intercalation of ions/molecules between the layers to weaken the interlayer attraction.[10] (2) Intercalation emerges as a powerful method to tune

physical or chemical properties of 2D materials by providing the highest possible doping level and being capable of facilely inducing phase change.[11, 12] (3) Applications of 2D nanomaterials in energy storage and conversion beyond their intrinsic materials limitations are possible by employing intercalation as a structural engineering tool.[13, 14]

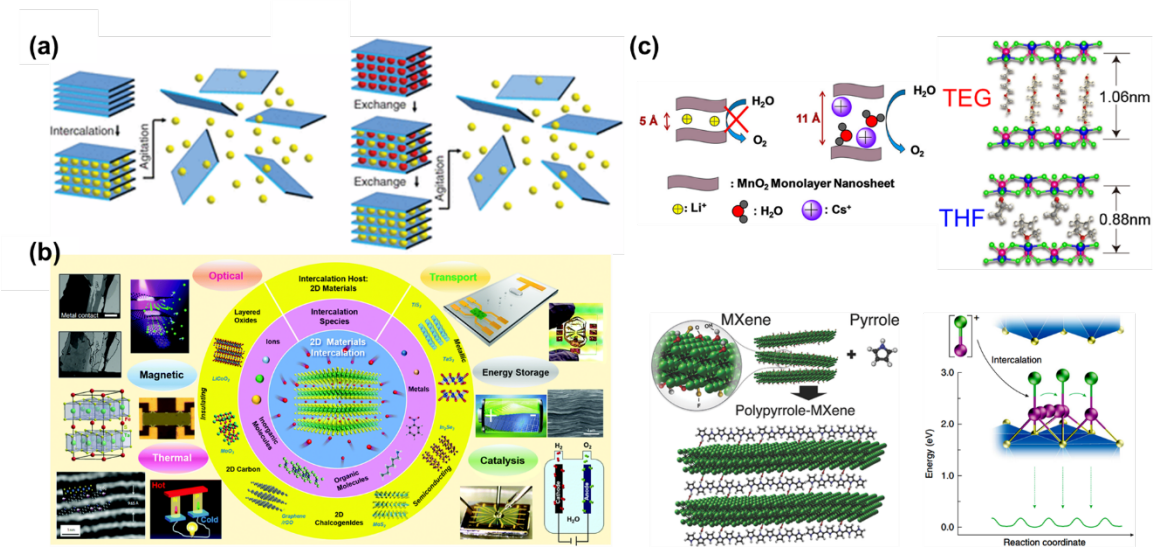

Figure 1.1 Intercalation chemistry in recent research of 2D materials. (a) Exfoliation of layered materials. (b) Physical or chemical tuning 2D nanomaterials by intercalation. (c) Applications of intercalated 2D structures in energy storage and conversion. Reproduced from reference 10, 12 and 14.

The intensive research interests in exploiting 2D materials as electrode materials for electrochemical energy storage (EES) stem from the urgent demand of revolutionary energy storage technologies toward building a sustainable modern society.[15] The great success of LIBs in powering portable electronics has been overshadowed by their limited abilities to barely fulfill the emerging requirement to electrify the transportation sector, such as powering electric vehicles.[16] In the near future, EES systems are also envisioned to undertake the tasks to overhaul the power grid in developed countries and to meet

expected rise in global energy needs by coupling with renewable energy sources such as solar and wind for powering the electrical grid.[17] Meanwhile, the potential bottlenecks in critical metals that currently being used in commercial LIBs emphasize the importance of searching for new electrode materials and charge storage mechanisms in order to lower the cost.[18] In this context, insertion-based materials, though being explored the earliest, are still promising candidates for many reasons. On the one hand, both synthesis of new materials for LIBs and exploration of old materials for beyond-lithium-ion batteries based on intercalation mechanism are viable approaches.[19, 20] On the other hand, opportunities are abundant in engineering existing materials toward modified properties and enhanced performance. For instance, strategies for improving energy storage density often benefit from having materials with a high surface-to-volume ratio, and this is particularly true for electrodes made of ultrathin nanosheets produced from thinning layered materials.[21, 22] Another example is nanostructuring or nanoarchitecting layered materials to shorten the diffusion time (τ) by reducing ion diffusion length (λ) or enhancing their diffusivity (D), according to $\tau = \lambda^2/D$.[23] This benefits power density, the measure of ability to deliver large amounts of energy with high rate capability. From the viewpoint of either materials chemistry or structural engineering, intercalation acts as the underlying fundamental process and serves as the scientific basis on which synthesis, characterization and modeling are conducted and rationalized.

Original research presented in this dissertation was carried out under the heat of utilizing 2D nanomaterials for energy storage. Research is this field covers a very broad spectrum of topics because the span of length scales in energy storage systems is enormous even at laboratory level.[24] As illustrated in Figure 1.2, a comprehensive study of a certain candidate material involves development of its synthetic methodology, characterization and analytics. The synthesis part includes not only production of the

material in the form of desired microscopic morphology, but also fabrication methods to build devices for both fundamental properties study and practical application. In order for theoretical analysis to provide insights into understanding of the underlying, sometimes complicated, physicochemical processes, multimodal characterization tools need to be integrated in a tight feedback loop between experiment and theory.

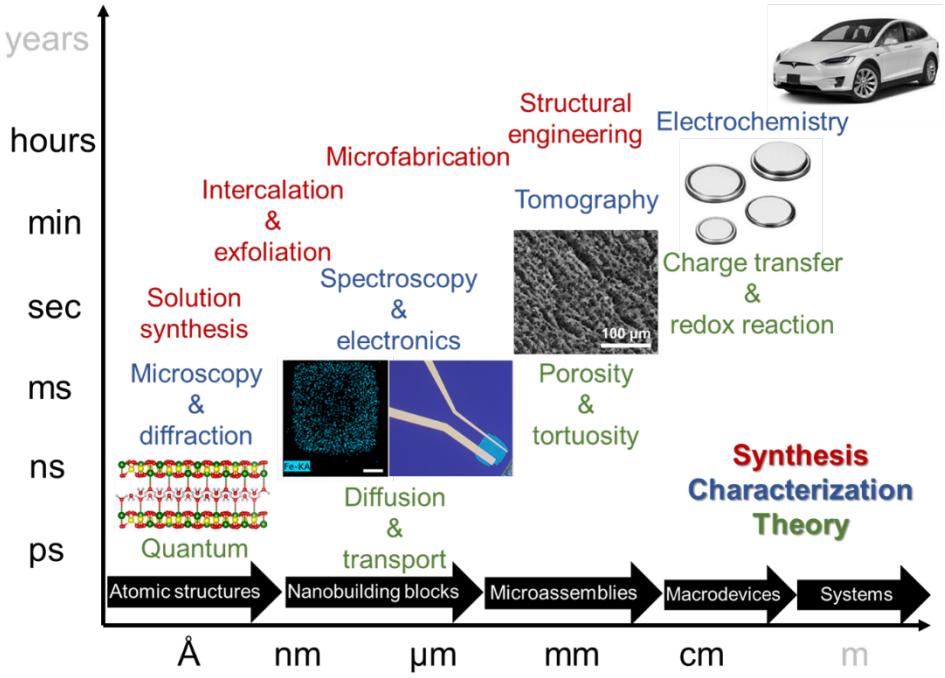

Figure 1.2 Length and time scales in the research of candidate materials for EES systems and typical methodologies from the viewpoint of materials science and engineering.

A broad overview of this dissertation concerning a special type of layered materials, $MOPO_4$ (M=V, Nb) hydrates, is briefed as following. These materials have been utilized as hosts for performing chemical intercalation in the form of microcrystals, and active materials for examining electrochemical intercalation in the form of nanosheets. The former represents a standard approach in studying intercalation

chemistry with complex intercalants, and the latter is closely relevant to EES as Li- and Na-ions are charge carriers. For probing the materials' charge transport/storage properties, it is useful to create single nanosheet devices that are the most clean systems, which also enable in situ characterization.[25, 26] However, this approach requires dedicated fabrication techniques and may suffer from instrument limitations, for instance, the difficulty to measure extremely small current (pA or below) due to low electrical conductivity. Alternatively, it is conventional to probe these properties in macrodevices, e.g., coin cells as adopted in this work, with the convenience of extracting performance data directly relevant to practical application. In the process of fabricating coin cells, structural design of the electrodes constituted by a mass of nanosheets plays a vital role in determining the electrochemical performance. Therefore, the connection between individual nanosheets and their micro- to macro-scale assembly must be treated as an important materials engineering problem. Considering the complexity of an EES system, this dissertation makes no attempt to cover all above aspects in an exhaustive manner. Instead, it focuses more on investigating fundamental intercalation chemistry of the target materials, in which previous studies left questions unanswered and properties unexplored.

Chapter 2 begins with an introduction of the crystal structures and basic properties of hydrated $MOPO_4$ family. While the two family members (M=V or Nb) exhibit many similarities, however, a tiny difference in intralayer interaction between the two results in significantly different morphologies when produced using nearly identical solution-phase synthesis methods. The hydrated $VOPO_4$ was found to be almost always in the form of microcrystals with a strict chemical formula $VOPO_4 \cdot 2H_2O$, whereas $NbOPO_4$ formed different hydrates with varied extent of hydration and several structures based on thin nanosheets. A particular uncommon one is a permanently intercalated structure induced by layer condensation that has never been found in $VOPO_4$.

In chapter 3, solution-phase intercalation of ferrocene, the most representative metallocene, into $VOPO_4 \cdot 2H_2O$ microcrystals is discussed. The intercalation process was first studied comparatively in acetone and 2-propanol, while in latter a much faster intercalation kinetics and phase transformation were observed. After resolving the fully intercalated structure via a combined experimental and theoretical approach, configurations of ferrocene molecules showing an exclusive orientation but different distributions among the $VOPO_4$ layers in the two solvents were clearly unraveled. This intercalation system was further scrutinized in a variety of common solvents with a special focus on primary alcohols, in which intercalation kinetics was found to follow an interesting volcano shape vs the number of carbons. In the attempt to isolate solvent-host interaction, a similar trend was observed in the exfoliation of $VOPO_4 \cdot 2H_2O$ in pure solvents. By modeling of the $VOPO_4$ layers with pre-intercalated solvent molecules, this solvent effects in both intercalation and exfoliation are understood at atomic level as a result of strong solvent-host interaction.

Chapter 4 details the systematic study of charge storage in both exfoliated $VOPO_4$ nanosheets and as synthesized $NbOPO_4$ nanosheets. The intriguing roles of interlayer H_2O molecules in facilitating ion intercalation and restoring structure of the host were analyzed, highlighting superior rate capability and high stability of $VOPO_4$ nanosheets in alkali-ion-based EES. The observed irreversible intercalation/deintercalation processes in $NbOPO_4$ was attributed to the weak interaction between interlayer H_2O molecules and $NbOPO_4$ layers, as well as the mismatch between redox potential of Nb^{5+}/Nb^{4+} and electrochemical window of H_2O. This disadvantageous property of $NbOPO_4$ was unexpectedly found to disappear, in the case of Li-ion intercalation, in the layer-condensed structure with intercalated PO_4 group as interlayer pillar. However, such pillaring effect turned out a failure in the case of Na-ion intercalation possibly due to a

blocking effect of the PO_4 group, leading to an insurmountable diffusion barrier. Nevertheless, the use of intercalation as a structural engineering concept was successfully demonstrated in the interlayer expansion of $VOPO_4$ nanosheets via incorporating small organic molecules for enhanced Na storage.

Finally in chapter 5, a brief summary of this dissertation is provided, together with possible future work based on past experiences in single nanosheet device and on-going efforts on large-scale assembly of nanosheets.

Chapter 2: Solution-phase synthesis of layered $MOPO_4$ hydrates

2.1 Introduction to 2D materials

2D materials, in the broad context of materials science, refer to those with one dimension being nano-sized and the other dimensions much larger, resembling a large but very thin sheet. Reducing the thickness of 2D materials down to a single atom is often possible, and this is particularly true for most well-known materials with layered structures, leading to 2D atomic crystals with high crystal quality and macroscopic continuity.[27] Figure 2.1 gives several representative 2D materials. Following the isolation of graphene via mechanical exfoliation in 2004,[28] this family of materials has rapidly expanded to include members like isomorphs of graphene (e.g. h-BN), elemental materials (e.g. phosphorene), TMDs (e.g. MoS_2), MXenes, metal oxides and phosphates, etc.[29] It should be pointed out that many materials do not have a layered structure but chemical bonds oriented in three dimensions, so thinning this type of materials by cutting these bonds will leave a high density of dangling bonds, which are chemically and energetically unstable. This drawback in top-down approaches (start with a bulk material and make it thinner) is complemented by bottom-up methods (start with the atomic ingredients and assemble them together). For instance, silicene cannot be exfoliated from bulk silicon, instead it must be epitaxially grown on a substrate and generally retains a strong interaction with it.[30] For non-layered 2D materials with single- or few-atomic thickness, the traditional wet-chemical synthesis has proven to be the most promising route toward their mass productions with high-yield.[31, 32] Several types of 2D layered materials possess an intermediate interlayer interaction between the typical van der Waals interaction and covalent interaction due to the presence of extra molecules (mostly H_2O) inside the interlayer space. It is possible to thin down these materials in a top-down

manner, but unlikely to harvest them in the form of monolayer structure. $VOPO_4 \cdot 2H_2O$ studied in this dissertation is a typical example.

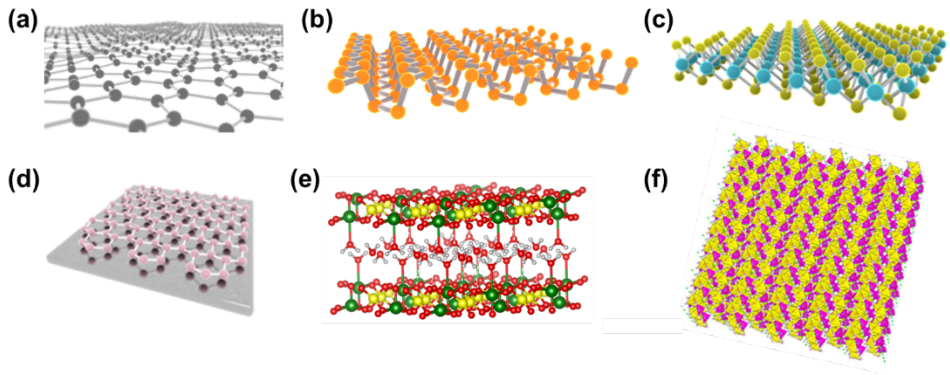

Figure 2.1 Representative 2D materials. (a) The first isolated modern 2D material graphene. (b) A single layer of black phosphorus - phosphorene. (c) A typical compound 2D material MoS_2. (d) Silicene, a monolayer of silicon, grown on a substrate. (e) Layered $VOPO_4$ with interlayer H_2O molecules. (f) Non-layered $LiFePO_4$ made into nanosheet.

Motivations to study 2D materials in reduced dimensionality include removal of or tuning van der Waals interactions, confinement of carries in a plane and increase of surface area-to-volume ratio. The first two are hot and important topics in physics community, and research in these areas lead to many significant scientific discoveries and promising practical applications.[33-35] The larger surface area-to-volume ratio of 2D materials means more contacting reactant and faster reaction when they are exposed to environment. This feature makes 2D materials more reactive than their bulk counterparts, an advantage that can be exploited for building chemical sensors[36] and electrochemical electrodes.[20, 21, 37, 38] The latter will be discussed in more detail in Chapter 4.

2.2 CRYSTAL STRUCTURES AND BASIC PROPERTIES OF $MOPO_4$ HYDRATES

$MOPO_4$ can be considered as a special case of tavorite-structured materials with the general formula $AM(TO_4)X$, where A is typically an alkali or alkaline-earth element, M is a transition metal, T is a p-block element, and X is O, OH, or F.[39] Layered vanadium phosphate, $VOPO_4$ in its α form, is most stable in its hydrated form $VOPO_4 \cdot 2H_2O$ at room temperature. $VOPO_4 \cdot 2H_2O$ crystalizes from V^{5+} containing solutions in phosphoric acid with a space group P4/nmm.[40] The structure consists of 2D layers of distorted VO_6 octahedra and PO_4 tetrahedra connected by shared oxygen atoms and H_2O molecules linking those layers (Figure 2.2a). Two H_2O molecules per $VOPO_4$ unit are incorporated between two adjacent layers. The first H_2O is coordinated to the V atoms to form the distorted VO_6 octahedra, and the second one forms H-bridges either with the upper or lower phosphate oxygens, creating a hydrogen bonding network (Figure 2.2b).[41] Loss of H_2O molecules brings $VOPO_4$ layers together without a noticeable disturbance of the lattice. This is seen as the anhydrous form with layered structure, α_I-$VOPO_4$, being the main dehydration product of $VOPO_4 \cdot 2H_2O$.[42] While α_I-$VOPO_4$ transforms into other polymorphs when heated at high temperature, there exists another layered structure, denoted as α_{II}-$VOPO_4$, that has been synthesized via a solid-state reaction route using a mixture of P_2O_5 and V_2O_5.[43] The two α forms differ in the position of the V atom inside the octahedron: it is on the same side with the P atoms in α_I and on the other side in α_{II} (Figure 2.2c). Layered $VOPO_4 \cdot 2H_2O$ (more precisely α-$VOPO_4 \cdot 2H_2O$), which is based on the crystal structure of α_I-$VOPO_4$, can be conveniently prepared using a simple solution-phase synthesis method.[44] This hydrate has several closely related structural derivatives, including an intermediate dehydrated phase $VOPO_4 \cdot 2H_2O$ with only V coordinating water,[45] a reduced phase $VOHPO_4 \cdot 0.5H_2O$ prepared via reduction of V^{5+} or using V^{4+} precursor,[46, 47] and a partially reduced phase $[H_{0.6}(VO)_3(PO_4)_3(H_2O)_3] \cdot 4H_2O$

converted spontaneously from $VOPO_4 \cdot 2H_2O$ upon standing in air.[48] The last one will be mentioned again in the section discussing synthesis of $VOPO_4 \cdot 2H_2O$.

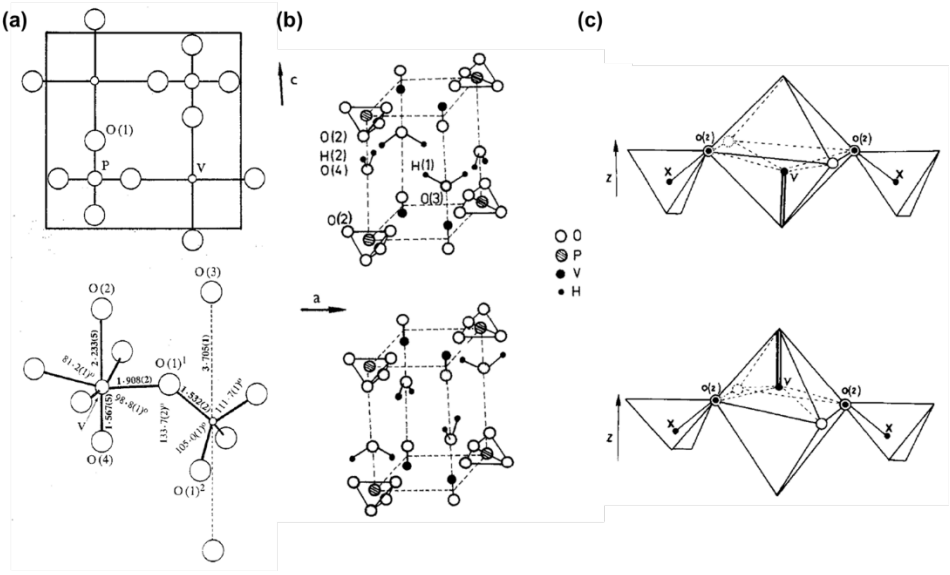

Figure 2.2 Crystal structure of $VOPO_4 \cdot 2H_2O$. (a) A layer of interconnected VO_6 octahedra and PO_4 (top) and associated bond distances and angles (bottom). (b) Two possible orientations of water molecules and corresponding hydrogen bonding networks. (c) Two different layered structures of anhydrous $VOPO_4$. Reproduced from reference 40, 41 and 42.

Compared with $VOPO_4$, literature information is scarce in $NbOPO_4$, despite that the report of its preparation seems even earlier.[49] The crystal structure of anhydrous $NbOPO_4$ follows the α_{II}-$VOPO_4$ type,[50] and the hydrated form is also slightly different from $VOPO_4 \cdot 2H_2O$ with unfixed water content, thus usually written as $NbOPO_4 \cdot nH_2O$.[51] In $MOPO_4$, the metal atom in the distorted MO_6 octahedra shows two types of M-O bonds: a short M=O bond and a M-O bond with bond length longer than a normal single bond (Figure 2.3a). In the V-Nb-Ta series, the differences between the long and short

bonds become smaller, and when the two bond lengths are the same, the incorporation of water is not allowed (no hydrates of α-$TaOPO_4$ have been found).[52] Three types of H_2O molecules have been identified in $NbOPO_4 \cdot nH_2O$: Nb coordinating water (type I) and non-coordinating water (type II) that are also found in $VOPO_4 \cdot 2H_2O$, and a new type of water (type III) existing in void spaces of the dihydrate phase, forming a trihydrate phase ($n \sim 2.8$). In contrast with $VOPO_4 \cdot 2H_2O$, the type II water in the dihydrate phase was proposed to possess an orientation of the H-H vectors perpendicular to the layers (Figure 2.3b). Moreover, the type III water was found to break the interaction between the type I water and the layer, causing increased mobility of H_2O molecules in the trihydrate phase.[52]

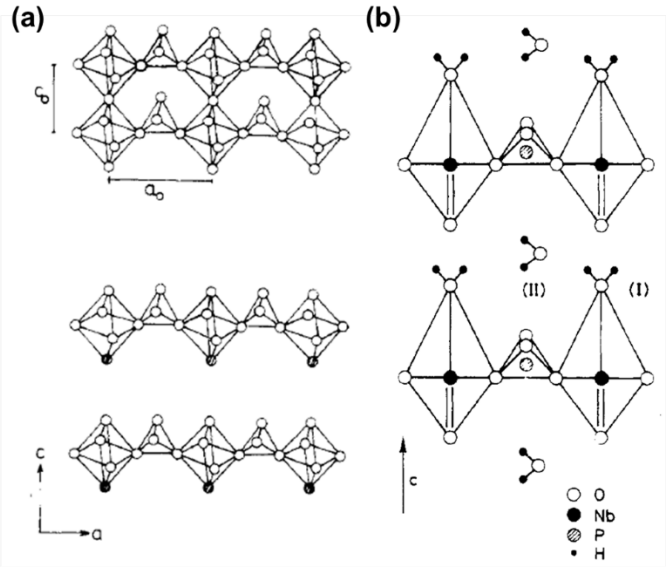

Figure 2.3 (a) Crystal structure of $MOPO_4$ (top) and two kinds of M-O bonds after cleaving the layers (bottom). (b) Coordinated H_2O (type I) and non-coordinated H_2O (type II) in $NbOPO_4 \cdot nH_2O$. Reproduced from reference 51 and 52.

Compounds with the general formula $MOPO_4$ discussed so far represent a group of layered materials which are able to accommodate guest species into the interlayer space. The formation of the hydrates itself is such an example with intercalation of a neutral species, namely H_2O molecules. $VOPO_4$ forms a monohydrate, a dihydrate, and a highly hydrated phase only when in contact with water (Figure 2.4a). The dehydration to anhydrous and rehydration to hydrates are reversible, and each phase has its own characteristic interlayer distance. Unlike in $VOPO_4$ that transitions between the different hydrates are shape, $NbOPO_4$ forms the hydrates in a more continuous manner with less change in the interlayer distance.[51]

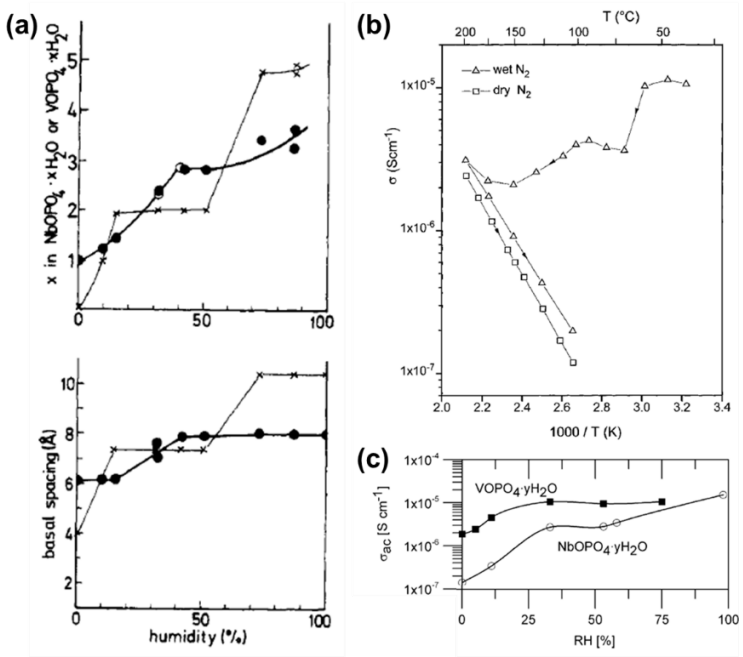

Figure 2.4 (a) Intercalation of water as a function of relative humidity (RH) at 25 °C: water content (top) and basal spacing (bottom) in $VOPO_4$ (●) and $NbOPO_4$ (X). (b) Dynamic conductivity of $VOPO_4 \cdot 2H_2O$ during heating and cooling cycles (arrows show the direction of temperature changes). (c) Conductivity of $MOPO_4$ hydrates as a function of RH at 20 °C. Reproduced from reference 51, 53 and 54.

Conductivity measurements indicate that $VOPO_4 \cdot 2H_2O$ is a mixed protonic-electronic conductor, and the protonic component dominates at room temperature.[53] The proton conduction decreases with increasing temperature due to the loss of interlayer water, and the overall conductivity starts to increase with increasing temperature once the $VOPO_4$ becomes anhydrous, indicating its main carriers are now electronic. In a reversible cooling cycle, the conductivity shows an Arrhenius type behavior with a higher activation energy under dry condition (Figure 2.4b). At approximately room temperature, the hydrates of $VOPO_4$ were measured to be generally more conductive than those of $NbOPO_4$ due to lower contribution from the electronic component in the latter (Figure 2.4c).[54]

An interesting and unique intercalation compound of $NbOPO_4$ was discovered as a phosphoric acid intercalated structure during the synthesis of hydrated $NbOPO_4$.[51] The layered acid niobium phosphate, with chemical formula $Nb_2(OH)_2(HPO_4)(PO_4)_2 \cdot 4.4H_2O$, was proposed to be composed of $Nb(OH)_2PO_4$ layers that are connected by H_3PO_4 molecules. The interlayer phosphoric acid was found to be stable even under intensive washing or extraction with boiling water, indicating formation of strong bonding between the intercalated molecules and the layers. The exact structure of this compound was not reported but a very similar phase with general formula $ANb_2(OH)_2(PO_4)_3 \cdot nH_2O$ (A=Na or K) has been synthesized.[55] This structure is understood by translation of the layers of $NbO(H_2O)PO_4$ by (½, ½, 0), leading to the superposition of NbO_6 octahedra with coordinating H_2O molecules facing each other along the *c* axis (Figure 2.5a). Connecting two adjacent layers is thus possible by linking these octahedra with a phosphate group to replace the H_2O molecules, forming a three-dimensional structure with correct stoichiometry. On the other hand, the structure of $Nb_2(OH)_2(HPO_4)(PO_4)_2 \cdot 4.4H_2O$ does not share the layer translation but is instead formed by combining every two layers of

$NbO(H_2O)PO_4$ with PO_4 group in such a way that the downward octahedra are connected to downward octahedra and upward octahedra to the upward octahedra (details will be given in next section). No stable structure following either layer condensation was found for $VOPO_4$, however, a closely related one has been reported in a layer-condensed structure assisted with intercalated organic molecules.[56] An compound with chemical formula $Na_2(MoOPO_4)_2(HPO_4)_3 \cdot 2H_2O$ sharing exactly the same structure with $ANb_2(OH)_2(PO_4)_3 \cdot nH_2O$ has also been reported (Figure 2.5b).[57] This type of three-dimensional framework possesses large cavities to accommodate the incorporated alkali-ions and water molecules, which are also exchangeable with other ions and molecules.

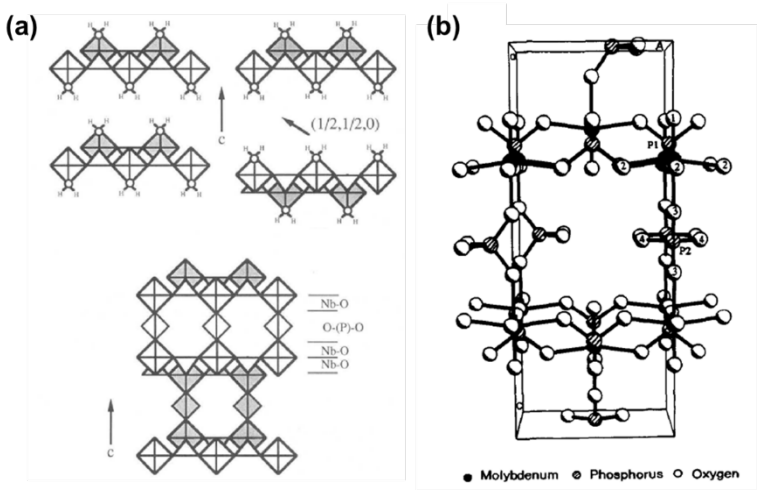

Figure 2.5 (a) Schematic illustration of the formation of $NaNb_2(OH)_2(PO_4)_3 \cdot nH_2O$ from condensing layers of $NbO(H_2O)PO_4$. (b) Unit cell of $Na_2(MoOPO_4)_2(HPO_4)_3 \cdot 2H_2O$ showing the same bridging of phosphate groups. Reproduced from reference 55 and 57.

2.3 MATERIALS SYNTHESIS

Preparation of anhydrous $MOPO_4$ was conventionally achieved via high temperature solid-state reaction route, and their hydrates were usually synthesized in

aqueous solution, from which H_2O molecules were incorporated in situ. Despite the simplicity of the recipes used in these solution-phase syntheses, much less effort has been put into understanding of the reaction processes themselves, as previous studies focused more on structural identification of the final products. In this dissertation, syntheses of $MOPO_4$ hydrates were carried out in a systematic manner, emphasizing important but less discussed aspects concerning mechanism, kinetics, role of additive, phase-control, etc.

Characterization techniques routinely used in this work were provided by lab equipment and facilities in Texas Materials Institute at UT Austin, including scanning and scanning transmission electron microscopy (SEM/STEM, Hitachi S-5500), X-ray diffraction (XRD, Rigaku MiniFlex 600), transmission electron microscopy (TEM, JEOL 2010F), energy-dispersive X-ray spectroscopy (EDS, Quanta 600), atomic force microscopy (Park Scientific Instruments XE-100), Fourier-transform infrared spectroscopy (FTIR, Thermo Scientific Nicolet iS 5), thermogravimetric analysis (TGA, PerkinElmer TGA 4000), Raman spectroscopy (WITec alpha300), and X-ray photoelectron spectroscopy (XPS, Kratos Axis Ultra DLD).

Characterization techniques involving external collaboration include TEM (FEI Titan Themis) located at the International Iberian Nanotechnology Laboratory and X-ray absorption spectroscopy (XAS) at the USTC National Synchrotron Radiation Laboratory.

Other minor characterization techniques, if any, will be introduced wherever appropriate.

2.3.1 Synthesis of $VOPO_4 \cdot 2H_2O$

The widely used synthesis method for $VOPO_4 \cdot 2H_2O$ was originally reported by Ladwig.[44] Preparation of $VOPO_4 \cdot 2H_2O$ in this work follows this method with slight

modification. Briefly, a solution containing 1.0 g V_2O_5 (a rust solid), 5.0 mL H_3PO_4 (85%), 10.0 mL HNO_3 (70%) and 25.0 mL H_2O was heated to reflux at 115 °C. After 24 h, the resulting bright yellow precipitate was collected by centrifugation, washed three times with acetone, followed by drying in the open air overnight. Water washing should be avoided as it was found to cause defective XRD pattern and partially dissolve the final product. The product is consisted of square-shaped microcrystals reflecting the tetragonal crystal structure (Figure 2.6a). The nominal chemical equation of this reaction is given by equation below.

$$V_2O_5 + 2H_3PO_4 + H_2O \longrightarrow 2VOPO_4{\cdot}2H_2O$$

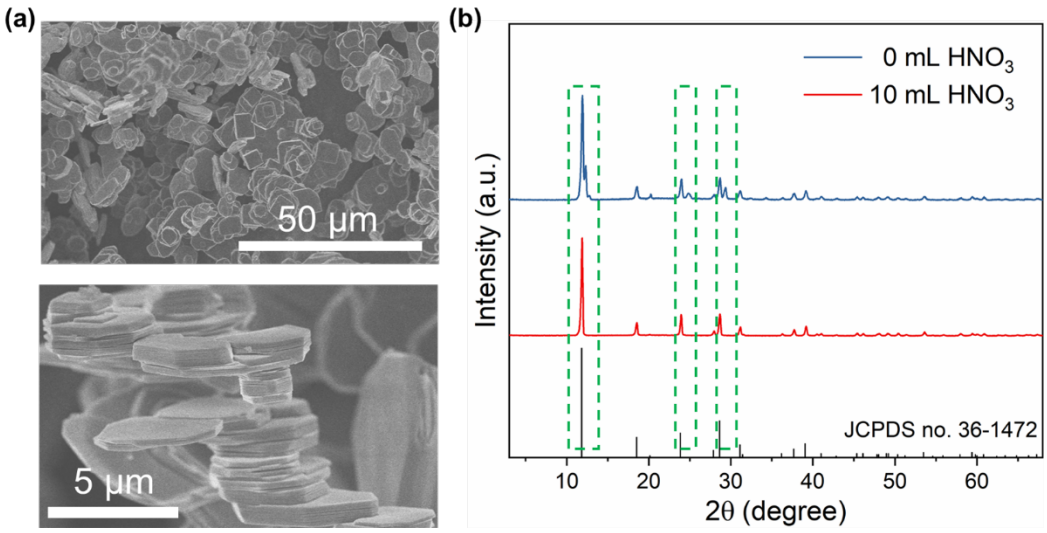

Figure 2.6 Synthesis of $VOPO_4{\cdot}2H_2O$. (a) SEM images showing morphology of the product synthesized with HNO_3. (b) XRD patterns of the products synthesized with and without HNO_3. Regions showing extra peaks are highlighted in dashed green squares.

Although HNO_3 does not participate in the reaction directly, previous studies reported that it could prevent V^{5+} from deoxidizing to V^{4+} during the synthesis.[58] A series

of control experiments with various amount of HNO_3 but the same total volume of the reaction solution were conducted. It was found that replacing all HNO_3 by H_2O led to a greenish product, probably caused by the presence of V^{4+} that is charge balanced by H^+. Extra peaks can be spotted in XRD pattern of this product, indicating existence of phase impurity (Figure 2.6b). In addition to the effect on the phase, HNO_3 was observed to greatly accelerate the reaction rate and increase the product yield. With its presence, the rust-colored mixture turned into bright yellow rapidly, and more so when the amount of HNO_3 increased (Figure 2.7a). The influence of HNO_3 is most obvious at about 5 mL, above which phase impurity is no longer seen. Beyond this point the reaction characteristics only depend weakly on the amount of HNO_3. However, 30 mL HNO_3 was found to retard the reaction rate possibly due to lack of H_2O in the reaction solution, as the formation of $VOPO_4{\cdot}2H_2O$ also requires structural water. The crystal growth is much faster in the *a*-*b* plane than along the *c* axis, however, the growth of lateral size tends to cease after 16 h while no such trend in the thickness in the case of synthesis with 10 mL HNO_3 (Figure 2.7b).

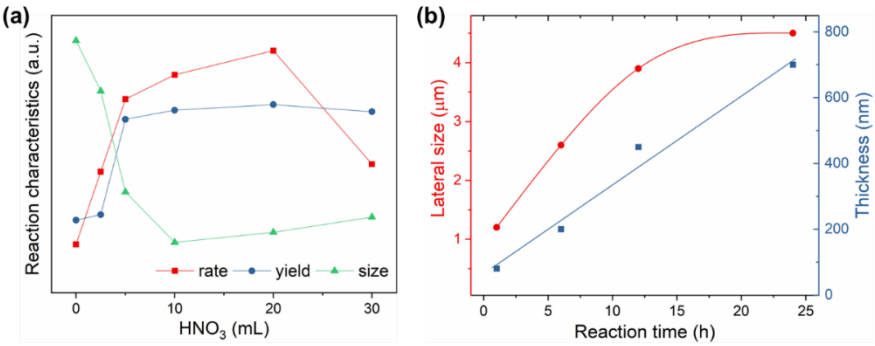

Figure 2.7 Effect of key parameters in synthesis of $VOPO_4{\cdot}2H_2O$. (a) Dependence of reaction rate, yield and product size on the amount of HNO_3. Reaction characteristics are normalized for illustration purpose. (b) Time-dependent size evolution of the product with 10 mL HNO_3.

There was no discussion on the detailed reaction mechanism in literature. Possible key steps to consider include dissolution of V_2O_5 solid into soluble V^{5+} species and subsequent interaction with PO_4^{3-} to constitute the 2D $VOPO_4$ layered network. However, further control and additional synthesis experiments indicate the reaction may be more complicated than expected. For instance, HNO_3 alone does not seem to dissolve V_2O_5 at all under the same reaction conditions. It is also possible to obtain phase pure $VOPO_4 \cdot 2H_2O$ using another vanadium precursor without using HNO_3. A summary of all synthetic methods explored in this work is given below (Table 2.1).

Precursor	Additive	Temperature	Morphology	Phase*
V_2O_5	None	115 °C	Microcrystals	**1+2**
V_2O_5	HNO_3	115 °C	Microcrystals	**1**
V_2O_5	HNO_3	R.T.	Nanosheets	**1**
V_2O_5	HCl	115 °C	Microcrystals	**1+2**
V_2O_5	HCl	R.T.	Nanosheets	**1+2**
V_2O_5	H_2SO_4	115 °C	Microcrystals	**1**
$NaVO_3$	HNO_3	R.T.	Nanosheets	**1**
$NaVO_3$	HCl	R.T.	Nanosheets	**1**
$VOSO_4$	HNO_3	115 °C	Microcrystals	**1**
$VOSO_4$	HNO_3	R.T.	Nanosheets	**1+2**
$VOSO_4$	H_2O_2	R.T.	Nanosheets	**2**

Table 2.1 Summary of synthetic methods using different vanadium precursors, additives and heating conditions (R.T. stands for room temperature). *1 represents the phase of $VOPO_4 \cdot 2H_2O$, and 2 represents the phase of $[H_{0.6}(VO)_3(PO_4)_3(H_2O)_3] \cdot 4H_2O$.

The choice of vanadium precursor has a huge impact on the product phase. The reaction using V_2O_5 proceeds at both low and high temperatures (slow at room temperature and fast above 100 °C), and the purity of the phase is guaranteed when sufficient HNO_3 is added. H_2SO_4 with strong oxidation ability plays a similar role as HNO_3, however, HCl without such ability does not. The possible influence of evaporation of HCl at high temperature is excluded as room temperature synthesis neither succeeds to yield the pure phase. The synthesis using $NaVO_3$ proceeds very rapidly in the presence of acid even at room temperature, possibly due to the fact that the precursor is soluble in water. Unlike the case of V_2O_5, no deoxidation of V^{5+} happens and HCl is able to produce phase pure $VOPO_4{\cdot}2H_2O$. In the synthesis using $VOSO_4$, an oxidizer is need to convert V^{4+} to V^{5+}, and again HNO_3 is able to serve this role but high temperature is necessary to eliminate phase impurity. Temperature also affects the morphology of the final product. Microcrystals are the typical product synthesized at high temperature (115 °C), while nanosheets with sub-100 nm thickness are usually harvested at room temperature. Perhaps the most interesting product is the one obtained by using $VOSO_4$ as vanadium precursor and H_2O_2 as oxidizer. The resulting dark green product in the form of thin nanosheets with very high aspect ratio (Figure 2.8a) can be indexed to $[H_{0.6}(VO)_3(PO_4)_3(H_2O)_3]{\cdot}4H_2O$, which was previously prepared from V_2O_5 and H_3PO_4 with a small amount of reducing agent under hydrothermally conditions.[48]

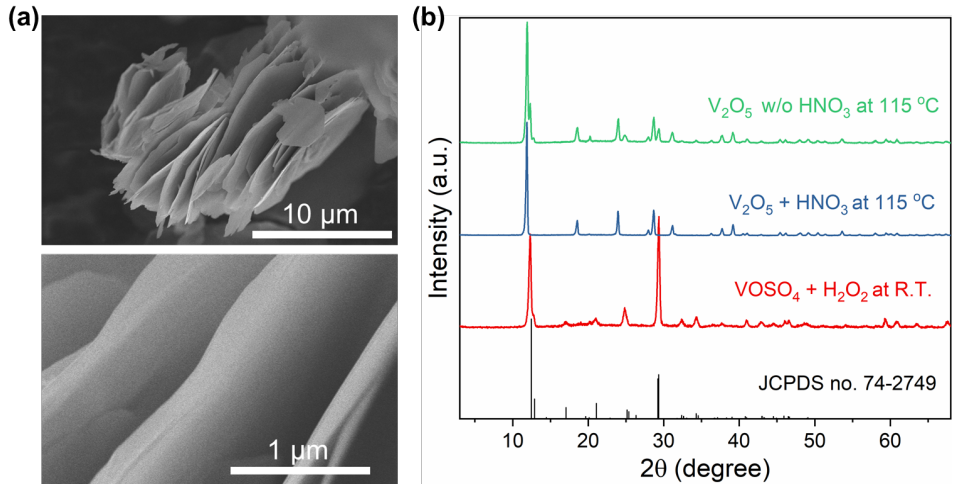

Figure 2.8 Product obtained using $VOSO_4$ as vanadium precursor and H_2O_2 as oxidizer. (a) SEM images showing the morphology of thin nanosheets. (b) XRD pattern of the product matching to $[H_{0.6}(VO)_3(PO_4)_3(H_2O)_3]\cdot 4H_2O$, which is responsible for the extra peaks observed in the product synthesized from V_2O_5 without HNO_3.

Comparing the XRD patterns of products synthesized at various conditions (Figure 2.8b), it is clear that the green product synthesized from $VOSO_4$ and H_2O_2 is a side-product in the synthesis using V_2O_5 without HNO_3. It is also likely the impurity found in all products with mixed phases, and the deoxidation of V^{5+} or the incomplete oxidation of V^{4+} is the fundamental reason for the formation of this partially reduced phase with respect to $VOPO_4\cdot 2H_2O$. In fact, the phases of $[H_{0.6}(VO)_3(PO_4)_3(H_2O)_3]\cdot 4H_2O$ and $VOPO_4\cdot 2H_2O$ are closely related because the *c* and *b* axes of the former are $\sqrt{2}\times a$ and $\sqrt{2}\times 3a$, where *a* in the *a*-unit cell dimension in the latter.[48] In fact, the initial bright yellow $VOPO_4\cdot 2H_2O$ powder was found to slowly turn green within a month, indicating the formation of the green phase that is thermodynamically more stable under ambient conditions.

2.3.2 Synthesis of $NbOPO_4 \cdot nH_2O$ and $Nb_2(OH)_2(HPO_4)(PO_4)_2 \cdot 1.7H_2O$

Research in synthesis of $NbOPO_4$ hydrates has been less popular than that of $VOPO_4$ hydrates, possibly due to the fact that previously well-established methods involves using HF to dissolve Nb_2O_5 or Nb metal as precursors.[51, 52] In this work, a water soluble Nb precursor, niobium (V) oxalate $Nb(C_2HO_4)_5$ was used to conduct all syntheses under similar conditions as in synthesis of $VOPO_4 \cdot 2H_2O$. Briefly, 1.25 g $Nb(C_2HO_4)_5$ (a white powder) was first dissolved in a 9.0 mL mixed solution containing H_2O and HNO_3 (70%) with volume ratio varied between 9:0 (pure water) to 0:9 (pure HNO_3), then 1.0 mL H_3PO_4 (85%) was added and the whole solution was heated to reflux at 115 °C. In a set of control experiments, a combination of 5 mL H_2O/HNO_3 and 5 mL H_3PO_4 was used. After 16 h, or other specified reaction time, the resulting white product was collected by centrifugation, washed three times with water and/or acetone, followed by drying in the open air overnight. The oxalate is a possible source of impurity, but it is likely to remain in the solution or decompose in the presence of HNO_3.[59] The (unbalanced) chemical equation of this reaction, assuming simple hydrates as the end product, is given by equation below.

$$Nb(C_2HO_4)_5 + H_3PO_4 + H_2O \longrightarrow NbOPO_4 \cdot nH_2O + C_2H_2O_4 \text{ (or } CO_2 + H_2O)$$

Compared with the synthesis of $VOPO_4 \cdot 2H_2O$, the reactions were found to be faster in this case due to high water solubility of the niobium precursor. In the absence of HNO_3, the clear solution turned cloudy even before T reached the preset value (115 °C), indicating the formation of solid product. Despite the fast reaction kinetics, the final product was found to possess the morphology of thin nanosheets (Figure 2.9a). Doubling the precursor concentration did not alter the morphology or the phase, instead, led to a product with less interlayer water. The difference in water content resulted in a noticeable peak shift in XRD (Figure 2.9b), corresponding to a change of interlayer distance. The

specific numbers of H_2O per $NbOPO_4$ unit were experimentally measured by TGA, from which two non-integers 2.5 and 1.7 were determined (Figure 2.9c).

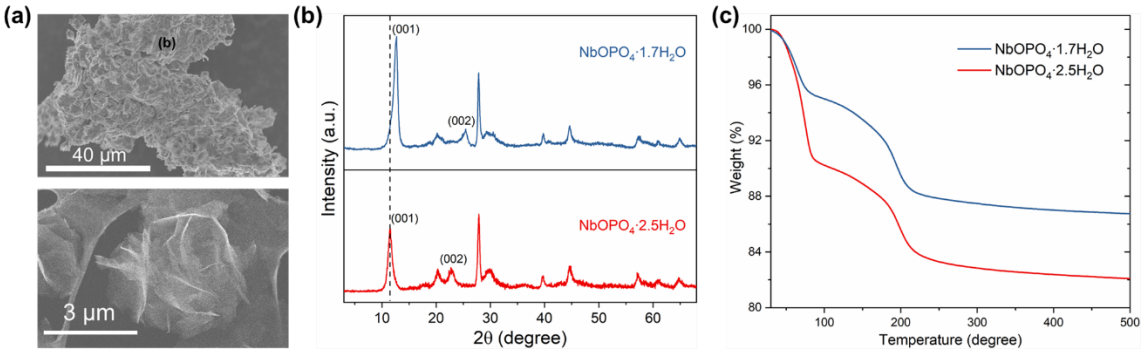

Figure 2.9 Product synthesized using $Nb(C_2HO_4)_5$ and H_3PO_4 without HNO_3. (a) SEM images showing the typical morphology of as synthesized $NbOPO_4{\cdot}nH_2O$. (b) XRD patterns of two products exhibiting the same phase but different interlayer distances. (c) TGA curves of the two products showing difference in water content.

As in the case of $VOPO_4{\cdot}2H_2O$, addition of HNO_3 is able to further accelerate the synthesis. In a mixed solution of H_2O and HNO_3 with volume ratio 8:1, the reaction was observed to proceed even at room temperature. In a wide range of H_2O/HNO_3 ratios (7:2 to 2:7), the reaction solution turned into a white gel within a few minutes after adding H_3PO_4 (Figure 2.10a), indicating the formation of a space spanning or percolating network constructed from the solid product containing the solvent. After refluxing and washing with water, the product usually remained in the gel state with significant retention of water inside. The gel was then freeze-dried to remove the water content without collapse of its microscopic structure. A highly porous solid consisting of individual nanosheets with micrometer lateral size was revealed (Figure 2.10b and c). XRD indicated the phase was similar to the above described $NbOPO_4{\cdot}nH_2O$. Therefore,

the product synthesized in this case can be considered a three-dimensional macroscopic assembly as a result of fast reaction kinetics.

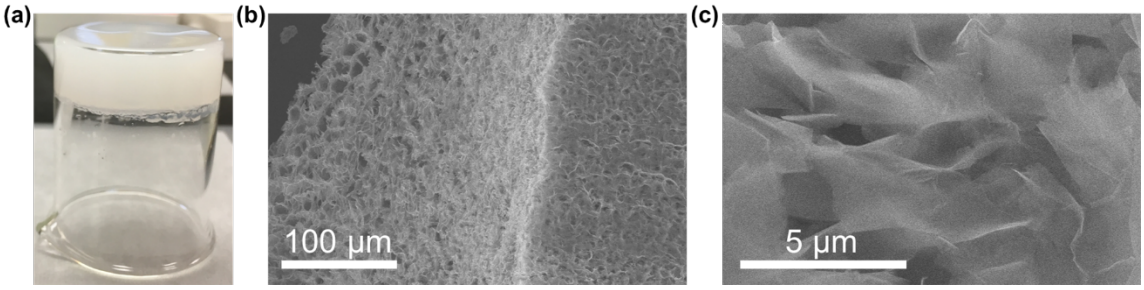

Figure 2.10 Product synthesized using $Nb(C_2HO_4)_5$ and H_3PO_4 in the presence of HNO_3. (a) Digital image showing the gel product obtained at room temperature. (b) SEM image showing the porous structure of the gel after refluxing, washing and freeze-drying. (c) High-magnification SEM image showing nanosheets as the backbone of the structure.

Besides the influence on reaction kinetics, HNO_3 also affects the phase of the final product at low H_2O/HNO_3 ratios. For instance, when pure HNO_3 was used (H_2O/HNO_3 = 0:9), a white solid precipitate instead of gel was formed upon adding H_3PO_4. The subsequent reflux heating led to a product with the similar nanosheets morphology of $NbOPO_4{\cdot}nH_2O$ (Figure 2.11a), but a very different crystal structure. It turned out the phase could be indexed perfectly to that of the previously reported $Nb_2(OH)_2(HPO_4)(PO_4)_2{\cdot}4.4H_2O$ (Figure 2.11b), namely $NbOPO_4$ intercalated with PO_4 group. TGA of this product exhibited two distinct dehydration steps (Figure 2.11c). The significant weight loss beyond 200 °C, which was not observed in $NbOPO_4{\cdot}nH_2O$, was attributed to the loss of OH groups from the interacted phosphate.[60] The final chemical formula was thus determined to be $Nb_2(OH)_2(HPO_4)(PO_4)_2{\cdot}1.7H_2O$.

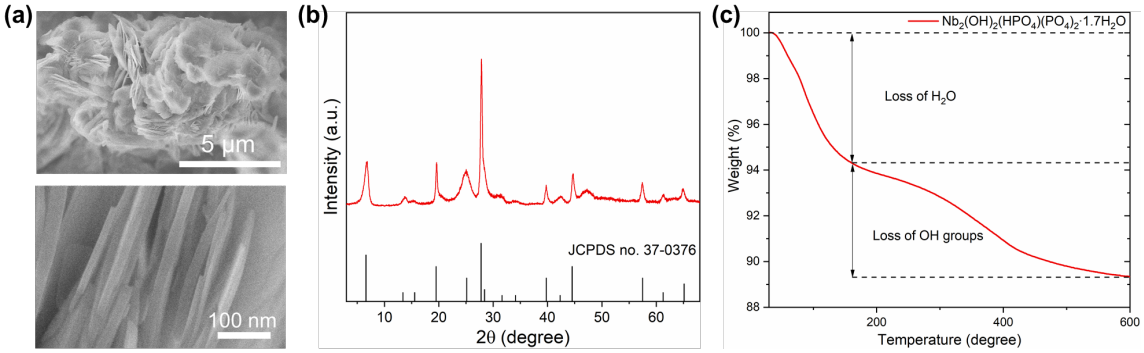

Figure 2.11 Product synthesized using $Nb(C_2HO_4)_5$ and H_3PO_4 in pure HNO_3. (a) SEM images showing the nanosheets morphology. (b) XRD pattern of the product matching to the phase of PO_4 group intercalated $NbOPO_4$. (c) TGA of the product revealing its chemical formula to be $Nb_2(OH)_2(HPO_4)(PO_4)_2{\cdot}1.7H_2O$.

The crystal structure of $Nb_2(OH)_2(HPO_4)(PO_4)_2{\cdot}1.7H_2O$, if different from that of $ANb_2(OH)_2(PO_4)_3{\cdot}nH_2O$, must be resolved. Clearly, it is structure derived from previously discussed $NbOPO_4{\cdot}nH_2O$, whose exact structure under current synthesis conditions is not quite understood. Unlike $VOPO_4{\cdot}2H_2O$ with a highly ordered structure, the loose arrangements of H_2O molecules in $NbOPO_4{\cdot}nH_2O$ and its derivative lead to inadequate quality of their diffraction patterns for Rietveld refinement. Therefore, first-principles density-functional theory (DFT) calculations were carried out to model this system based on the known structure of anhydrous α_{II}-$NbOPO_4$. In the first step, the structure of $NbOPO_4{\cdot}2H_2O$ was calculated by stacking identical α_{II}-$NbOPO_4$ layers along the *c*-axis, including two H_2O molecules following the previous study.[52] The calculation result shows that, the H-H vectors of the non-coordinated water possess a certain orientation to form hydrogen bonding with Nb=O instead of perpendicular to the layers (Figure 2.12a). An interlayer distance of 7.23 Å can be concluded from this structure, an expected value between 7.00 Å and 7.69 Å that were experimentally determined from the

XRD patterns of $NbOPO_4 \cdot 1.7H_2O$ and $NbOPO_4 \cdot 2.5H_2O$. In the process to connect adjacent layers of $NbOPO_4$ in order to construct the structure of $Nb_2(OH)_2(HPO_4)(PO_4)_2 \cdot 1.7H_2O$ with correct stoichiometry, it was found that the same layer translation in $ANb_2(OH)_2(PO_4)_3 \cdot nH_2O$ could not be applied to α_{II}-$NbOPO_4$ due to significant steric hindrance. The structure construction without layer translation was only possible when layers of α_I-$NbOPO_4$ and α_{II}-$NbOPO_4$ were connected in a layer-by-layer manner (Figure 2.12b). Transition between α_I-$NbOPO_4$ and α_{II}-$NbOPO_4$ is nearly impossible at low temperature when the layers are already formed. However, in the solution-phase synthesis where $NbOPO_4$ layers are formed via a bottom-up assembly of molecular precursors, it is possible to generate both types of layers when the driving force for layer condensation is strong. The final calculated structure without considering H_2O molecules (since all Nb atoms are saturated thus the H_2O molecules are mostly free water inside the structure) exhibits a simulated XRD pattern very close to the experimental one (Figure 2.12c), validating the proposed structure construction. The obvious mismatch of relative intensities among certain diffraction peaks is probably caused by the thin thickness of the product with large area ratio between basal plane and edge planes.

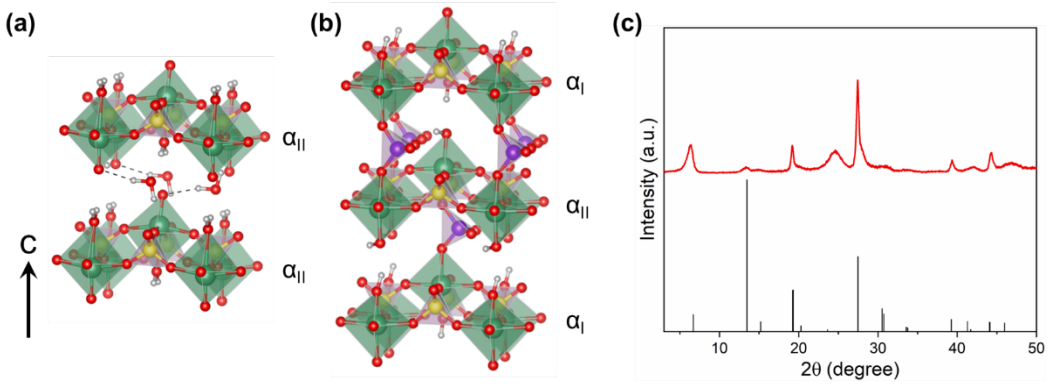

Figure 2.12 DFT calculations for $NbOPO_4$ system. (a) Structure of calculated $NbOPO_4 \cdot 2H_2O$ based on stacking layers of α_{II}-$NbOPO_4$. (b) Proposed structure of $Nb_2(OH)_2(HPO_4)(PO_4)_2 \cdot 1.7H_2O$ with PO_4 groups (highlighted in purple color) connecting layers of α_I-$NbOPO_4$ and α_{II}-$NbOPO_4$. (c) XRD patterns of experimental product and predicted structure by DFT calculation shown in (b).

To understand the formation mechanism of the phosphate intercalated structure, time-dependent phase evolution of the product was probed by ex situ XRD. Under the normal synthesis conditions with 1 mL H_3PO_4, the initially formed white precipitate, which was found to be amorphous, converted to the intercalated phase from the simple $NbOPO_4 \cdot nH_2O$ phase via a two-phase mechanism (Figure 2.13a). The process thus involved the formation of 2D $NbOPO_4$ network as a first step, followed by the gradual intercalation of phosphate group toward a complete phase transformation. In the case of 5 mL H_3PO_4, the reaction proceeded via a single-phase-to-single-phase mechanism, showing a continuous shift in the peak associated with the intercalation of phosphate group (Figure 2.12b). This is understood as the layer condensation is slower than the growth in *a*-*b* plane and higher H_3PO_4 concentration is likely to diminish such difference.

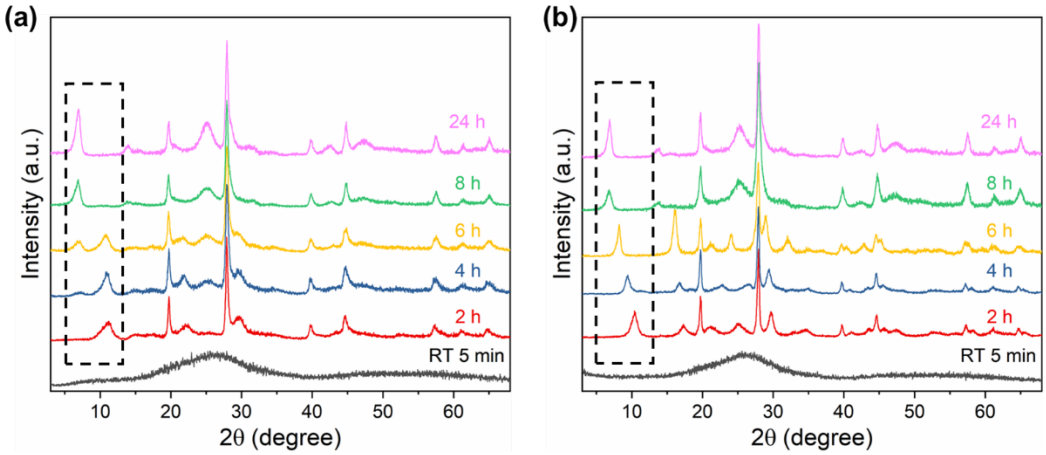

Figure 2.13 Effect of H_3PO_4 concentration in time-dependent phase evolution during synthesis of $Nb_2(OH)_2(HPO_4)(PO_4)_2{\cdot}1.7H_2O$. (a) In 9 mL pure HNO_3 and 1 mL H_3PO_4. (b) In 5 mL pure HNO_3 and 5 mL H_3PO_4. Peaks associated with the intercalation of phosphate group are highlighted in dashed black squares.

The synthetic method for $NbOPO_4$ hydrates developed in this work needs to be rationalized with understanding of the solution chemistry of niobium oxalate in acidic solutions. Niobium oxalate was previously used as a precursor to synthesize Nb_2O_5, and the molecular states of aqueous niobium oxalate solutions were found to depend mainly on the solution pH. According to a previous investigation using Raman spectroscopy,[61] dissolving niobium oxalate in aqueous solution generates two niobium oxalate ionic species, $[NbO(C_2O_4)_3]^{3-}$ and $[NbO(C_2O_4)_2H_2O]^-$, and the equilibrium of the two is largely affect by H^+ concentration according to equation below.

$$[NbO(C_2O_4)_3]^{3-} + H_3O^+ \leftrightarrow [NbO(C_2O_4)_2H_2O]^- + HC_2O_4^-$$

The ionic species $[NbO(C_2O_4)_2H_2O]^-$ is an important intermediate as it forms a dimeric $[Nb_2O_4(OH)_2(C_2O_4)_2]^{2-}$ in the presence of OH^-, and its further polymerization in the basic solution leads to the formation of hydrated Nb_2O_5.[62] In acidic solution, a similar

polymerization is expected with phosphate groups serving as the linking nodes to form the 2D $NbOPO_4$ layers (Figure 2.14a). The role of HNO_3 in synthesis of $NbOPO_4$ hydrates is thus simply to provide H^+, which critically determines the reaction kinetics and the phase of the final product (Figure 2.14b). Larger HNO_3/H_2O ratio, namely higher concentration of H^+ or lower pH, promotes faster the formation of the $NbOPO_4$ layer and more complete layer condensation. The gel product is an intermediate product possessing a loosely condensed structure without permanent PO_4 bonding to the layers, while the $Nb_2(OH)_2(HPO_4)(PO_4)_2 \cdot 1.7H_2O$ represents a fully condensed structure with PO_4 intercalating into and bonding with the layers.

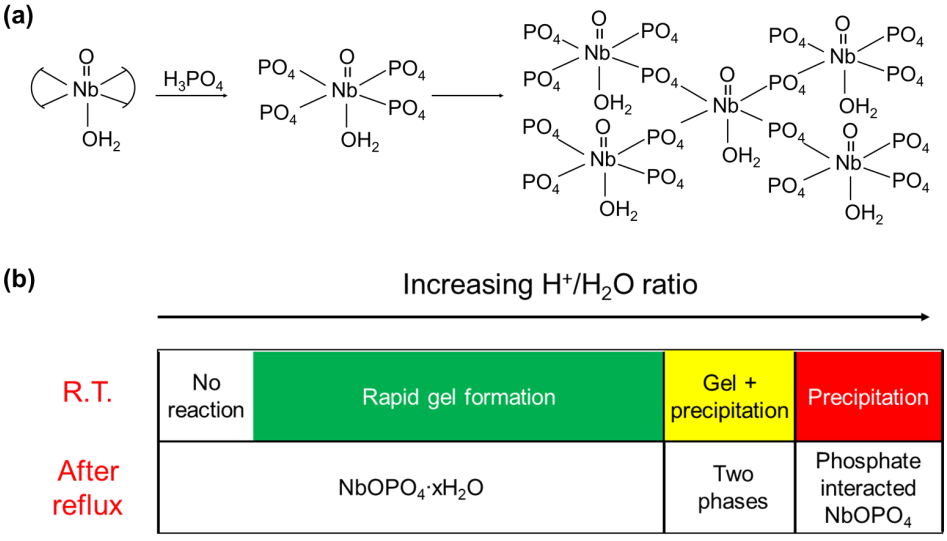

Figure 2.14 Summary of synthesis of $NbOPO_4$ hydrates using $Nb(C_2HO_4)_5$ as precursor. (a) Schematics showing the polymerization of $[NbO(C_2O_4)_2H_2O]^-$ into a 2D network in the presence of H_3PO_4. (b) Summary of synthesis of various $NbOPO_4$ hydrates using $Nb(C_2HO_4)_5$ as precursor.

2.4 CONCLUSION

Production of $MOPO_4$ (M=V, Nb) hydrates can be conveniently achieved via solution-phase synthesis route with proper precursors in aqueous solution. V_2O_5 is the most widely used vanadium precursor to obtain the structurally stable layered dihydrate $VOPO_4 \cdot 2H_2O$, provided sufficient HNO_3 is present. This reaction proceeds slowly at room temperature, but rapidly to form microcrystals under reflux conditions. It is also possible to carry out the synthesis using water soluble precursors, such as $NaVO_3$ and $VOSO_4$. In these cases, the reactions proceed rapidly at room temperature in the presence of acid for the former and oxidizer for the latter. Nanosheets are the typical products in both cases due to the low reaction temperature. For $VOSO_4$, both high temperature and a strong oxidizer are required to form the correct dihydrate phase. The use of H_2O_2 at room temperature leads to the isolation of a pure phase, $[H_{0.6}(VO)_3(PO_4)_3(H_2O)_3] \cdot 4H_2O$, that commonly coexists with $VOPO_4 \cdot 2H_2O$ when the synthesis is not optimized. This phase is thermodynamically more stable than $VOPO_4 \cdot 2H_2O$, as the latter gradually converts to the partially reduced phase in the open air.

In synthesis of $NbOPO_4$ hydrates, water soluble $Nb(C_2HO_4)_5$ has been shown to be a great replacement of Nb_2O_5, which was the most widely used niobium precursor in previously studies. In the absence of HNO_3, the reaction proceeds rapidly at reflux temperature and leads to products in the form of nanosheets. In addition to the difference in morphology, the product also differs from $VOPO_4 \cdot 2H_2O$ in its various possible hydration states depending on the precursor concentration used in synthesis. In the presence of HNO_3, the reaction kinetics is significantly accelerated, and the reflux products include a nanosheets-based gel and a new layered structure intercalated with PO_4 group as the ratio of H^+/H_2O in reaction solution increases. No such intercalated structure has ever been found in $VOPO_4$ hydrates, possibly due to strong interaction

between the coordinated H_2O and the vanadium atom that prevents the formation of V-PO_4 bonds inside the interlayer space.

Chapter 3: Ferrocene intercalation chemistry in $VOPO_4 \cdot 2H_2O$*

3.1 INTRODUCTION AND HISTORICAL REMARKS

Layered vanadium phosphates, including anhydrous α_I-$VOPO_4$ and $VOPO_4 \cdot 2H_2O$, have a very rich intercalation chemistry due to their open interlayer space and the possibility of vanadium to exist in multiple oxidation states.[63] $VOPO_4 \cdot 2H_2O$ itself can be considered as a product from intercalation of water into α_I-$VOPO_4$.[64] The interlayer distance of $VOPO_4 \cdot 2H_2O$ (7.41 Å) is larger than that of α_I-$VOPO_4$ (4.11 Å), making intercalation reactions occur easier in $VOPO_4 \cdot 2H_2O$, which has been extensively studied as an intercalation host. Intercalation reactions of $VOPO_4 \cdot 2H_2O$ can be divided into two groups depending on whether the oxidation state of vanadium changes. The first group involves intercalation of Lewis bases which form covalent bonds with vanadium atom in the host layer without redox process. Typical intercalants in this group include alcohols,[65, 66] amines,[67, 68] aldehydes and ketones,[69, 70] heterocyclic N-donors,[71, 72] carboxylic acids,[73] etc. The second group involves the reduction of vanadium with concomitant intercalation of cations. This type of reactions can be carried out in the presence of a reducing agent,[74] and intercalation of a variety of cations including alkali-, alkaline-earth-, transition metal cations,[75] H^+,[76] NH_4^+,[77] and even large organic ammonium cations,[78] has been successful.

A special case of the redox intercalation reactions of layered materials is the incorporation of metallocenes which behave as pseudo-alkali metals and transfer an

*This chapter is reproduced from following manuscripts published or submitted:
Y. Zhu, Y. Qian, Z. Ju, L. Peng, G. Yu, "Solvent-Dependent Intercalation and Molecular Configurations in Metallocene-Layered Crystal Superlattices", *Nano Lett.* 2018, 18, 6071.
Y. Zhu, Y. Ji, Z. Ju, K. Yu, P. J. Ferreira, Y. Liu, G. Yu, "Ultrafast Intercalation Enabled by Strong Solvent-Host Interaction: Understanding of Solvent Effect at Atomic Level", *Angew. Chem. Int. Ed.* submitted.
Y. Zhu carried out the experimental work and wrote the manuscripts.

electron per molecule to the hosts.[79] The metallocenes are a class of organometallics composed of a metal ion sandwiched between a pair of cyclopentadienyl rings. Intercalation of these bulky molecules follows charge transfer mechanism with complete ionization of the metallocenes, namely reduction of vanadium is accompanied by their oxidation. Ferrocene (fc) is the prototype of metallocenes and its high ionization potential renders it only a few redox intercalation hosts,[80-82] including $VOPO_4 \cdot 2H_2O$. Because of its large size, intercalation of ferrocene into $VOPO_4 \cdot 2H_2O$ induces loss of interlayer water and the whole process follows the reaction equation below.

$$VOPO_4 \cdot 2H_2O + xfc \longrightarrow fc_xVOPO_4 \cdot (2\text{-}y)H_2O + yH_2O$$

An intriguing question to ask in such intercalation system is that, what orientation of the metallocene will be, which was once a subject of unresolved debate for many years. Incomplete intercalation and poor crystallinity of the final products usually imposed significant challenges in analyzing the intercalated structures. Past research effort has been focused on layered TMDs, and most studies concluded the guest resided with its principal molecular axis parallel to the layers based on X-ray/neutron diffraction and solid state nuclear magnetic resonance experiments.[83, 84] For intercalation of ferrocene into $VOPO_4 \cdot 2H_2O$, previous studies in this specific intercalant-host pair drew no cogent or even contradictory conclusions. The first study of this intercalation reaction was performed in acetone solution, showing a relatively low extent of intercalation (x = 0.12) and two basal spacings (9.9 and 8.5 Å),[81] which were attributed to two possible orientations of interlayer residing ferrocene in a later study.[85] In another report, ferrocene with principal axis perpendicular to $VOPO_4$ lattice planes was concluded.[86]

The content discussed in this chapter covers every important aspect of ferrocene intercalation into layered $VOPO_4 \cdot 2H_2O$ by taking into account the influence of solvent. Revisiting this old intercalation system is important, as organic intercalation as a general

structural engineering strategy for layered materials has been recently demonstrated in many functional device applications.[14, 87, 88] In particular, artificial superlattices consisting of alternating organic−inorganic layers offer unparalleled opportunities beyond the reach of existing materials.[89, 90] Forming these hybrid materials can be achieved via controlled intercalation of organic molecules into inorganic layered hosts, which is a complex course involving multiple physicochemical processes. In solution phase, it is further complicated by interaction of solvent molecules with the intercalant and/or host. This part of research is motivated by the lack of systematic studies in this system to address fundamental aspects, such as configuration of the intercalant, structural alteration of the host, thermodynamics and kinetics, effect of medium, and so forth, that are crucially related to the intercalation process.

Perhaps the most significant novelty of this work lies in the attempt to understand solvent effects in intercalation chemistry. In a broad context, solvent effects are ubiquitous in all areas of chemistry involving solution phase reactions. In many cases, solvent effects can be interpreted by treating the solvent as a macroscopic continuum characterized by its macroscopic physical properties.[91] However, this convenient approach may fall short in analyzing reactions that proceed in extremely confined space, for instance, intercalation between layers with a few nm or even sub-nm separation.[92] In this context, a solvent is more realistic to be considered as a discontinuum which consists of individual molecules defined and depicted by their molecular properties and atomic interactions. Therefore, it is imperative to understand solvent effects at a molecular level or below. Solvent effects in intercalation chemistry emerges as an important topic recently owing to the growing interest in production of ultrathin nanosheets via liquid exfoliation of layered materials,[10] as well as the exploration of solvent-assisted charge transport for energy storage applicaitons.[93] In both cases, solvent-host interaction has

been found to play a critical role in reversing the thermodynamic inhibitions to attain otherwise impossible equilibrium states.[94, 95] However, much less attention has been paid to the kinetic effects brought by the solvent. In particular, the transient role of solvent molecules in terms of their molecular level interaction with and atomic level structural alteration to the host has not been well understood.[96]

3.2 SOLVENT-DEPENDENT INTERCALATION AND MOLECULAR CONFIGURATIONS

In this part, intercalation of ferrocene into layered $VOPO_4 \cdot 2H_2O$ was investigated in two solvents (acetone and 2-propanol), exhibiting strong solvent-dependent kinetics and phase evolution. Molecular configurations of ferrocene molecules were unraveled to show an exclusive orientation of ferrocene but different arrangements among the layers in the two solvents. Resolving the intercalated structures was possible thanks to a combined experimental and theoretical approach.

$VOPO_4 \cdot 2H_2O$ microcrystals were synthesized according to the previously described method with further modifications to improve shape regularity and size uniformity. Specifically, a mixture of V_2O_5 (2 g), H_3PO_4 (85%, 12 mL), HNO_3 (70%, 15 mL) and H_2O (40 mL) was refluxed at 130 °C for 20 h. Variation in the extent of intercalation partially depends on dimensions of the host material. Therefore, all intercalation reactions were carried out in a single batch of $VOPO_4 \cdot 2H_2O$ microcrystals with average size about 3 μm and thickness about 500 nm (Figure 3.1a).

All intercalation reactions were carried out in capped glass vials at room temperature, unless otherwise stated. In a typical reaction, 300 mg ferrocene was first dissolved in 30 mL 2-propanol or acetone. The solution was added with 100 mg $VOPO_4 \cdot 2H_2O$ powder and the mixture was then subject to mild stirring (350 rpm), upon

which the original yellow powder turned into green (rapidly in 2-propanol and slowly in acetone). After desired intercalation time was reached, the product powder was collected by centrifugation, washed with the same solvent (5 x 50 mL), and dried in air for at least 24 h before any characterization.

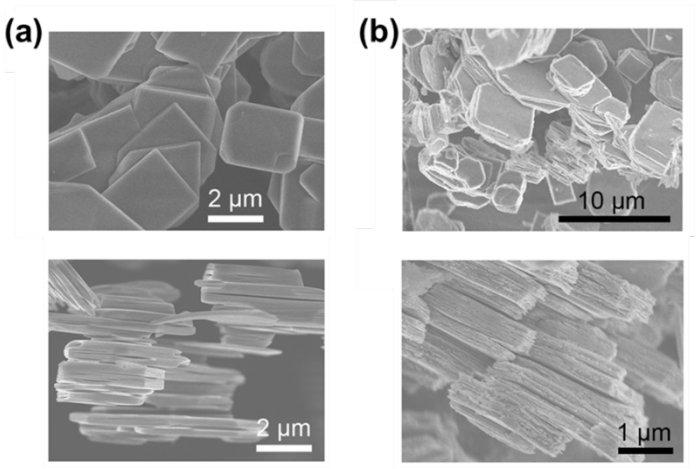

Figure 3.1 Influence of intercalation on morphology. (a) SEM images of as synthesized $VOPO_4 \cdot 2H_2O$ microcrystals. (b) SEM images showing the microcrystals after ferrocene intercalation.

The intercalation process induces no significant morphology change but a clear edge roughening (Figure 3.1b). The incorporation of ferrocene into $VOPO_4$ layers is evident by the detection of Fe element using EDS (Figure 3.2a) and characteristic stretching bands of ferrocene [$\nu(sp^2$ C-H stretch) = 3110 cm^{-1} and ν(C=C) = 1417 cm^{-1}] using FTIR (Figure 3.2b), respectively. Another convincing evidence comes from TEM cross-sectional view of the intercalated sample that was prepared by sonication of microcrystals into thin nanosheets, some of which showed rolled edges for imaging. An

interlayer distance of 9.9 Å (only two significant figures due to relatively poor quality of the image) is determined (Figure 3.2c), larger than that of $VOPO_4 \cdot 2H_2O$ (7.41 Å).

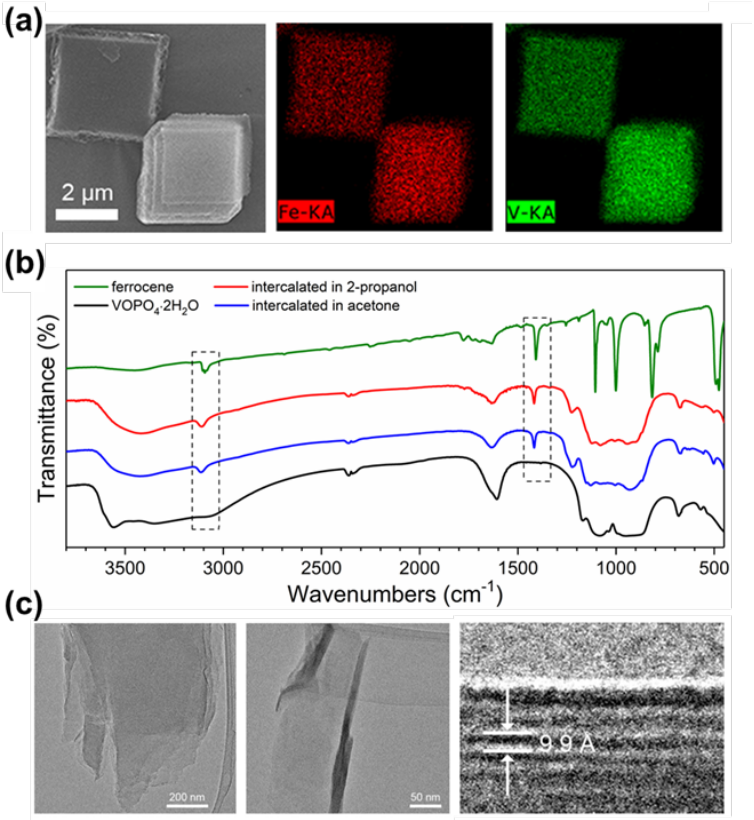

Figure 3.2 Characterization of ferrocene intercalated $VOPO_4$. (a) EDS elemental mapping of intercalated microcrystals. (b) FTIR spectra of ferrocene, $VOPO_4 \cdot 2H_2O$ and intercalation products. Characteristic bands of ferrocene are highlighted in dashed squares. (c) TEM images of the intercalation product.

Differences in phase evolution between the two solvents are revealed by ex situ XRD measurements. The patterns of intercalation products obtained at various time intervals (Figure 3.3) share a similar shift of the (001) peak of $VOPO_4 \cdot 2H_2O$ ($2\theta = 11.9°$) to higher angle with gradual decrease of intensity. However, two low angle peaks

observed in acetone manifest the most striking difference compared to a single peak in 2-propanol. Assuming the appearance of low angle peak is a result of enlarged interlayer distance, peak position of the single peak in 2-propanol (9.04°) gives a value of 9.77 Å according to Bragg's law, matching reasonably well with the one directly measured from TEM. It is also noted that intercalation in 2-propanol is more rapid and considered to attain completion between 12 h to 24 h, judging by disappearing of the shifted (001) peak, whereas in acetone this point lies beyond 48 h.

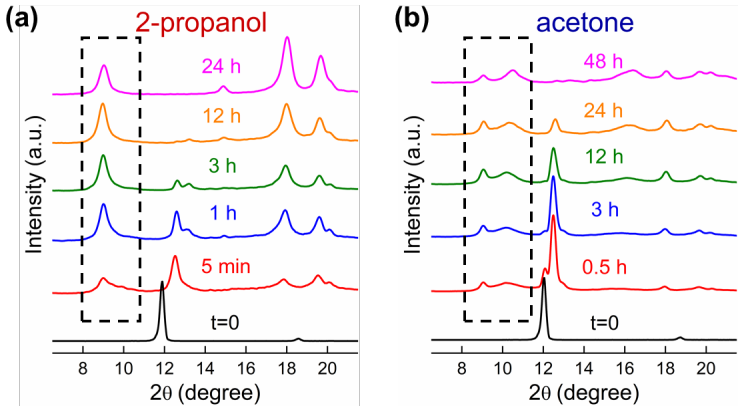

Figure 3.3 Time-dependent XRD patterns of the products when intercalated in (a) 2-propanol and (b) acetone. Intercalation-induced peaks are highlighted in dashed rectangles.

All intercalation products exhibit enhanced thermal stability compared to the starting materials, as revealed by TGA (Figure 3.4). Upon heating in air, $VOPO_4{\cdot}2H_2O$ loses its interlayer water molecules in two well-resolved steps, while ferrocene undergoes sublimation below 200 °C. All intercalation products start with an initial dehydration step up to ~ 200 °C, followed by decomposition of intercalated ferrocene until ~ 600 °C, at which most samples attain maximum weight loss except for those with short intercalation time in acetone, possibly due to low intake of ferrocene. The weight gain at the end may

be due to oxidation of ferrocene decomposition products. Attempt to calculate the amount of intercalated ferrocene by assuming several possible end products at either maximum or final weight loss, however, was not successful. In all cases, the calculation usually overestimated the value significantly. Therefore, the decomposition behavior of ferrocene-intercalated $VOPO_4$ is nontrivial.

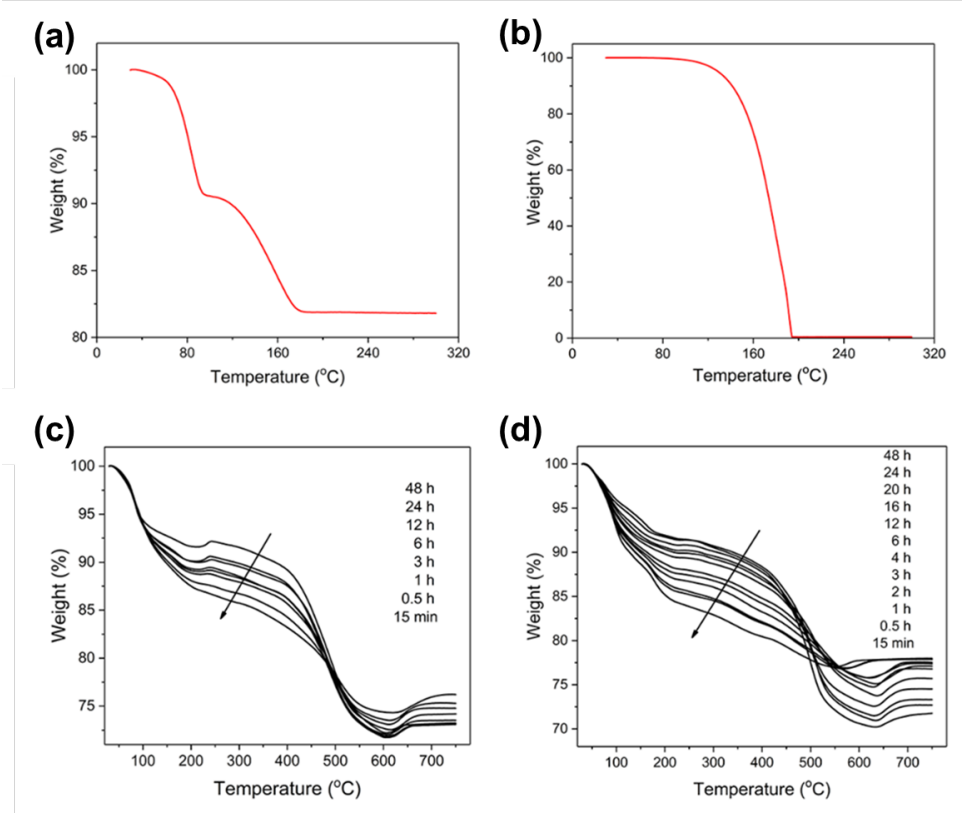

Figure 3.4 TGA curves of (a) $VOPO_4 \cdot 2H_2O$, (b) ferrocene, and intercalation products with various reaction times in (c) 2-propanol and (d) acetone.

To quantitively analyze reaction rate, intercalation kinetics is studied by plotting extent of reaction (α) vs time.[97] Given the complexity shown in XRD and TGA measurements, the amount of intercalated ferrocene was evaluated directly using EDS as the atomic ratio of Fe to V (denoted as fc/$VOPO_4$). All intercalated samples for EDS

were prepared by drop-casting their acetone solutions to form a dense film individually. In a typical measurement, at least three areas containing a large quantity of microcrystals were scanned and an average value was generated. The accuracy of this method using EDS was confirmed by inductively coupled plasma mass spectrometry. Then α was calculated as the ratio of experimental intercalated ferrocene to its maximum theoretical value, which is 0.5 ferrocene per $VOPO_4$ unit (the reason will be clear later in structural analysis). From the plot of intercalated ferrocene vs time (Figure 3.5a), it is immediately obvious that intercalation kinetics is much faster in 2-propanol. The apparent deceleratory shape of the two curves excludes the Avrami-Erofeyev solid-state kinetics model, which features a sigmoidal shape as shown in previous studies on TMDs.[96] This indicates that ferrocene intake at the edge of $VOPO_4 \cdot 2H_2O$ (nucleation) is rather rapid compared to the diffusion of ferrocene inside the $VOPO_4$ layers (nuclei growth). Therefore, the overall intercalation process is diffusion controlled. In this context, together with the 2D structure of $VOPO_4 \cdot 2H_2O$, the well-established 2D diffusion model with integral form $(1 - \alpha) \ln(1 - \alpha) + \alpha = kt$ is adopted to describe the intercalation kinetics (Figure 3.5b).[97] The first few points from both cases are able to produce a straight line, validating the applied model. Slopes of the two lines, corresponding to the rate constant k, manifest a 3.7 times faster intercalation rate in 2-propanol, at least in the initial stage. The deviations from the model after 1 h in 2-propanol and 6 h in acetone probably imply that the intercalation is no longer diffusion controlled. Interestingly, in both cases deviations begin at very close $fc/VOPO_4$ values, indicating a common cause for the retardation.

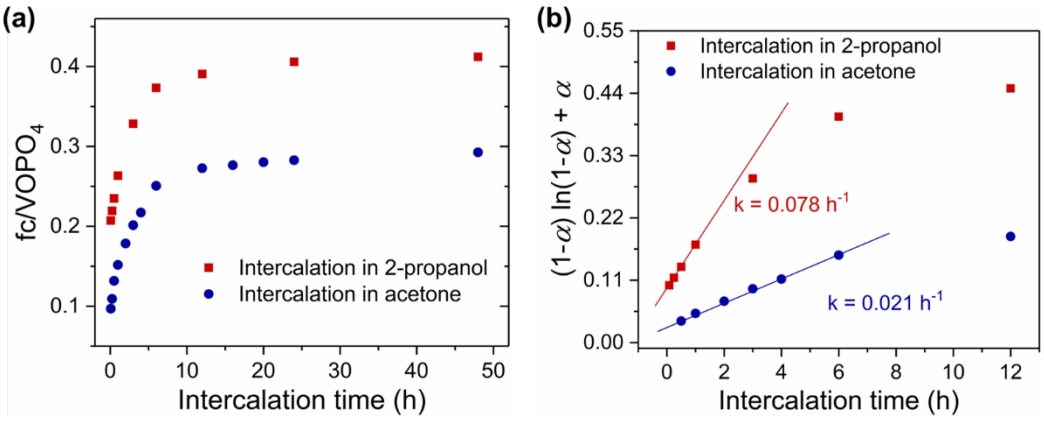

Figure 3.5 Analysis of intercalation kinetics. (a) Plot of intercalated ferrocene vs time, where fc/$VOPO_4$ is the Fe/V ratio determined by EDS. (b) Kinetic modeling using 2D diffusion model, as plotted by (1 - α) ln(1 - α) + α vs time, where α, the extent of reaction, is calculated as $\frac{fc/VOPO_4}{0.5}$.

In order to unravel the configuration of intercalated ferrocene, the interplay of its location and associated steric hindrance is first surveyed. For better illustration purpose, the crystal structure of $VOPO_4 \cdot 2H_2O$ is simplified to display bonds inside the interlayer only (Figure 3.6a). In the meanwhile, as the size of ferrocene (~ 6 Å) is comparable to the lattice parameter of $VOPO_4 \cdot 2H_2O$ (a = b = 6.2 Å), the ferrocene molecule is simplified accordingly with consideration of its shape. The accommodation of ferrocene into $VOPO_4$ is then attempted with minimum possible steric hindrance. By directly inserting ferrocene molecules into $VOPO_4$ layers (Figure 3.6b), it is impossible to avoid significant steric hindrance (highlighted by red dashed rectangles) regardless of its orientation. However, if adjacent $VOPO_4$ layers are shifted by half unit (Figure 3.6c), ferrocene molecules can be fit in without suffering any previous steric hindrance. This intuitive reasoning, after furhter taking into account of the crystallographic symmetry of

$VOPO_4 \cdot 2H_2O$, leads to a layer sliding by half unit in both *a* and *b* directions, namely a (½, ½, 0) layer transition is concluded.

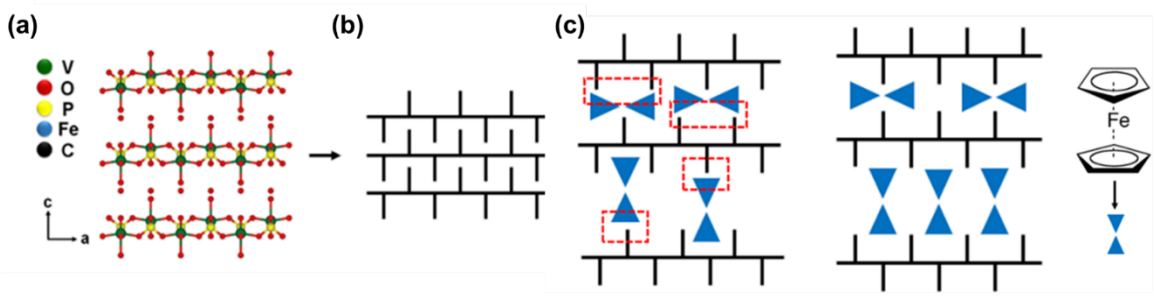

Figure 3.6 Consideration of steric hindrance in ferrocene-$VOPO_4$. (a) Cross-sectional view of $VOPO_4 \cdot 2H_2O$ crystal structure, and (b) its simplified form. (c) Accommodation of ferrocene without any change in $VOPO_4$ (left) and with layer translation in *a* direction by half unit (right).

The orientation of ferrocene is then determined using first-principles calculations, which are helpful tools for the in-depth understanding of what happens on the atomic and electronic scale for the organic−inorganic hybrid structures.[98] In order to predict the most stable structure, various parallel and vertical ferrocene intercalated $VOPO_4$ models are proposed with above mentioned layer translation included (Figure 3.7). First-principles calculations based on the DFT were performed within generalized gradient approximation (GGA). Core electron states were represented by the projector augmented-wave method as implemented in the Vienna *ab initio* simulation package (VASP).[99] The Perdew–Burke–Ernzerhof (PBE)[100] exchange correlation functional and a plane wave representation for the wave function with a cut-off energy of 450 eV were used. The atomic positions and cell parameters were fully relaxed to obtain the total energy and optimized cell structure.

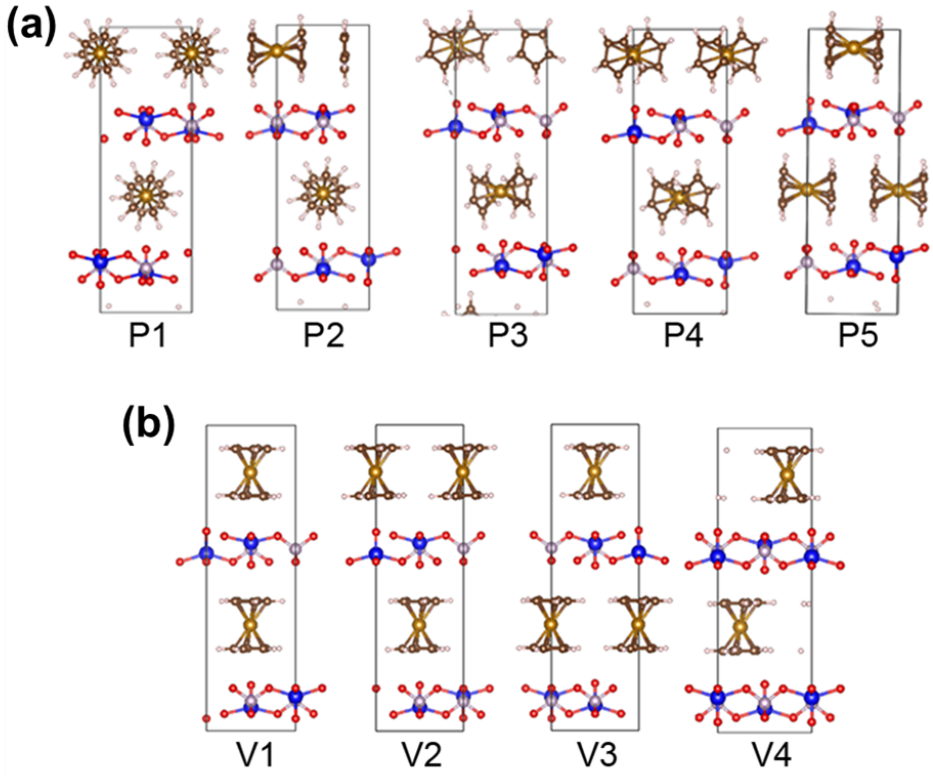

Figure 3.7 Selected configurations that subject to DFT calculation. (a) Five models with parallel orientation of ferrocene and (b) four models with vertical orientation.

As shown by the calculation results of above configurations (Table 3.1), vertical orientations with principal axis of ferrocene perpendicular to $VOPO_4$ lattice planes result in larger expansions in *c*-axis than parallel ones. Considering the largest experimental *c*-axis expansion (corresponds to the peak in 2-propanol or the left peak in acetone that located at $2\theta = 9.04°$) to be 19.5 Å, vertical orientations with overlarge expansions are easily ruled out. In contrast, parallel orientations induce smaller interlayer expansions that are close to the experimetnal value. This type of configurations also promotes a π-π interaction among the cyclopentadienyl planes, which provides a additional stabilization energy for the intercalated structure.[89]

	Model 1	Model 2	Model 3	Model 4	Model 5
			Parallel		
a-axis	6.25	6.30	6.35	6.40	6.30
c-axis	19.5	19.5	19.8	19.5	19.8
			Vertical		
a-axis	6.30	6.25	6.25	6.31	
c-axis	21.7	22.0	22.0	20.5	

Table 3.1 Calculated lattice parameters of each model (Å).

Besides the comparison in *c*-axis, the number of possible models can be further narrowed down by examining the lattice parameter in *a*-axis. The invariant (200) peak (2θ = 28.6°) throughout the whole intercalation indicates there is no change of lattice constant (Figure 3.8). This value of 6.23 Å in *a*-axis, together with above calculated 19.5 Å in *c*-axis, declares the best match to be model P1 in Figure 3.7 and Table 3.1.

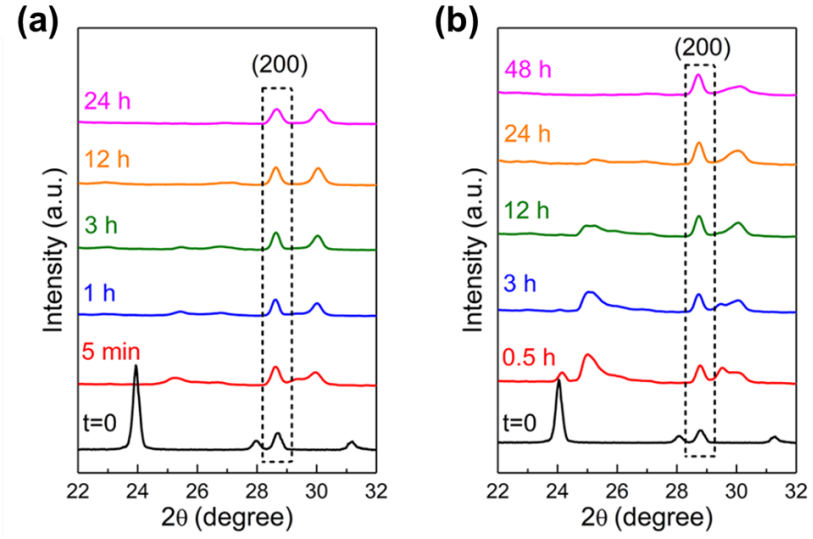

Figure 3.8 Time-dependent XRD patterns in (a) 2-propanol and (b) acetone with extended 2θ range. (200) peaks are highlighted by dashed rectangles.

The final input from the DFT calculations is the enthalpies of all selected models, among which P1 shows the most negative value, concluding its highest possibility as the most stable configuration.

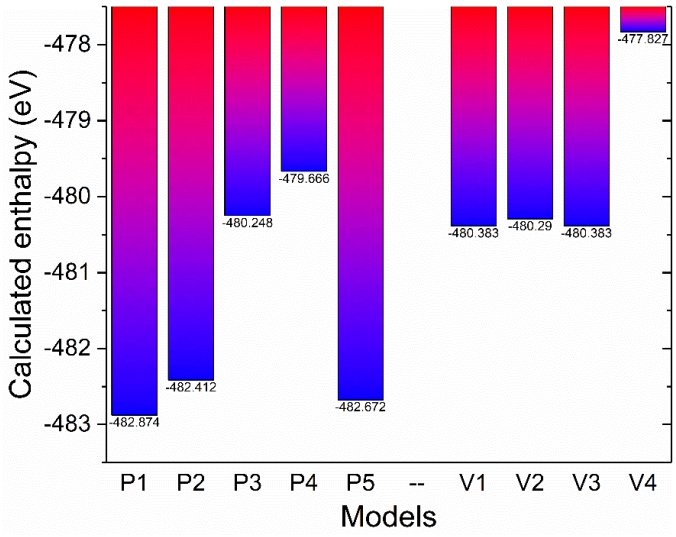

Figure 3.9 Calculated enthalpy of each model (eV).

To summarize all above structural derivation and calculation results, the final resolved structure of ferrocene intercalated $VOPO_4$ requires a (½, ½, 0) layer translation and total removal of interlayer water molecules in the original $VOPO_4 \cdot 2H_2O$ (Figure 3.10a), leading to a chemical formula $fc_{0.5}VOPO_4$ assuming complete intercalation. A perfect match can be seen between the XRD pattern simulated from this structure and that of 24 h product in 2-propanol (Figure 3.10b). Indeed, the intercalation product after 48 h in 2-propanol was determined to be $fc_{0.42}VOPO_4$ according to EDS, close to the theoretical formula. At this point, the intercalation in 2-propanol can be clearly understood as a single-phase-to-single-phase transformation.

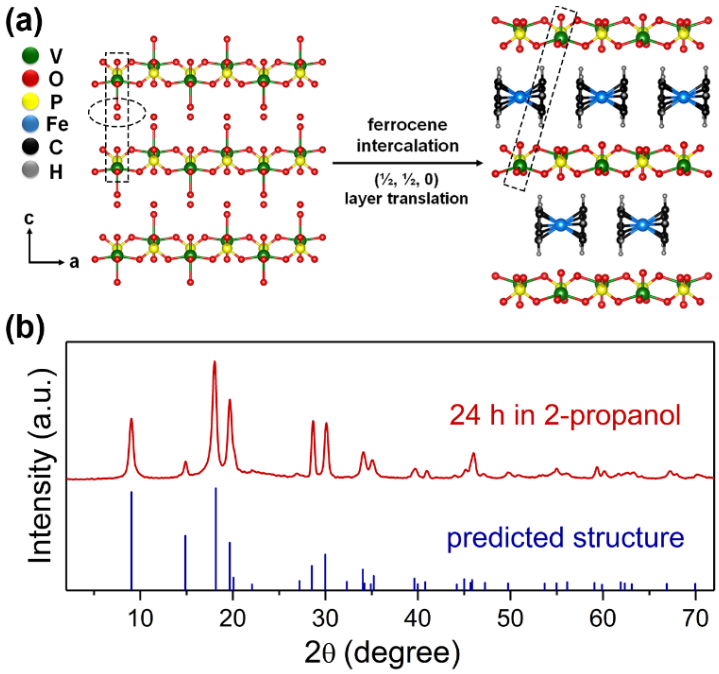

Figure 3.10 Resolved strucutre of fc-$VOPO_4$. (a) Schematic illustration of ferrocene intercalating into $VOPO_4 \cdot 2H_2O$ (layer translation is highlighted in dashed rectangle; interlayer H_2O molecules are highlighted in dashed oval). (b) XRD patterns of experimental product and predicted structure by DFT calculations.

The evidently slower intercalation kinetics in acetone suggests possible existence of intermediate products, which can be described by staging phenomenon.[92] A zoom-in plot of the time-dependent XRD patterns in acetone displays a stationary peak, which is now understood as the fully intercalated structure (stage 1 compound), and a broad peak that shifts gradually toward higher angle with noticeable peak narrowing (Figure 3.11a). The latter is recognized as a result of stage disordering and can be quantitatively analyzed by the Hendricks-Teller (HT) theory,[101] which describes the oscillatory variation in linewidth with diffraction order if there exists a random stacking sequence of two interlayer distances. Taking the XRD pattern at 12 h as an example (Figure 3.11b), the

broad peak sandwiched between peak 1 (fully intercalated layers) and peak 2 (partially dehydrated $VOPO_4$, non-intercalated layers) is as result of a random arrangement of these two layers.

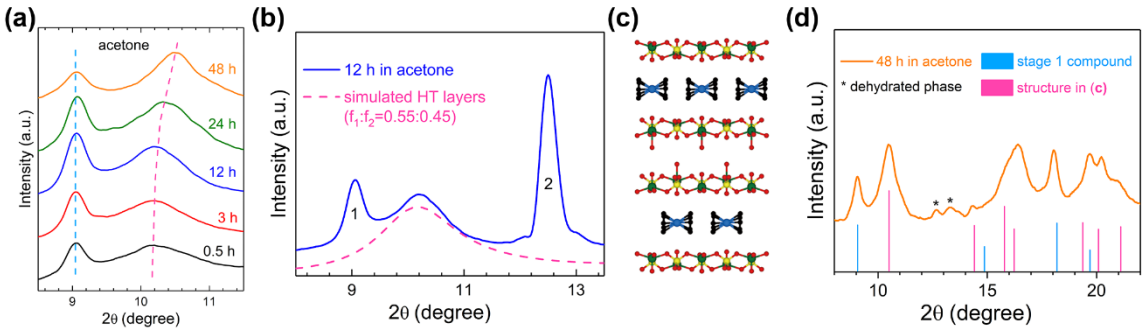

Figure 3.11 Interpretation of XRD patterns in acetone. (a) Time-dependent XRD patterns zoom-in at low-angle region. (b) Simulated XRD pattern of HT layers at 12 h. (c) Structure of stage 2 intercalated compound (hydrogen atoms are omitted for clarity). (d) XRD patterns of experimental product and calculated structure.

The detailed calculation procedures[102] using HT theory are quoted as follows. Define $f^{(1)}$ and $f^{(2)}$ as the fractions of layers with the interlayer distance d_1 and d_2, and the X-ray phase shift $\emptyset$ occurring between successive layers is given by $\emptyset = (4\pi d/\lambda)\sin\theta$. Then the dependence of the scattered intensity on Bragg angle is given by

$$I_{av} = |V_L|^2 \frac{1 - C^2}{1 - 2C\cos\overline{\emptyset} + C^2}$$

where C and $\overline{\emptyset}$ are calculated as

$$C = f^{(1)}\cos\left(\emptyset^{(1)} - \overline{\emptyset}\right) + f^{(2)}\cos\left(\emptyset^{(2)} - \overline{\emptyset}\right)$$

$$\overline{\emptyset} = \tan^{-1}\frac{f^{(1)}\sin\emptyset^{(1)} + f^{(2)}\sin\emptyset^{(2)}}{f^{(1)}\cos\emptyset^{(1)} + f^{(2)}\cos\emptyset^{(2)}}$$

The layer form factor V_L is a slowly varying function of diffraction angle and does not significantly affect the computed basal-plane linewidths or positions.

A reasonably good match between the HT-modelled pattern and the experimental one is found by assigning fractions of intercalated layers (f_1) and non-intercalated layers (f_2) with a ratio of 0.55:0.45. Peaks at other time intervals can be calculated likewise. As intercalation proceeds, such layer disordering would undergo a disorder-order transition, forming an ordered intermediate structure, which turns out to be stage 2 compound with alternative intercalated and non-intercalated layers (Figure 3.11c). At 48 h, the experimental XRD pattern is already resolvable mainly to be the sum of two patterns belonging to stage 1 and stage 2 compounds (Figure 3.11d). Therefore, the presence of two intercalation-induced peaks in acetone has been successfully explained.

It is intriguing to observe the co-existence of stage 1 and stage 2 compounds in acetone throughout the whole intercalation. This is even true when intercalation time was extended to one month. More interestingly, though quite stable at room temperature, the intercalation product in acetone was converted to pure stage 2 compound when mildly heated at 50 °C (Figure 3.12). A straightforward interpretation is that the stage 2 compound is thermodynamically more stable. As increase in the basal spacing of the layered host lattice imposes one of the most significant energy penalties during intercalation, the stage 2 compound with less extent of interlayer expansion is thus energetically favorable compared with the stage 1 compound. The energy difference between the two compounds may be further increased when taking into consideration of the repulsion of positively charged ferrocenium ions in adjacent layers, which is present in the stage 1 compound but absent in the stage 2 compound. If stage 1 compound is indeed thermodynamically less stable, its rapid formation in 2-propanol must be due to kinetic reasons.

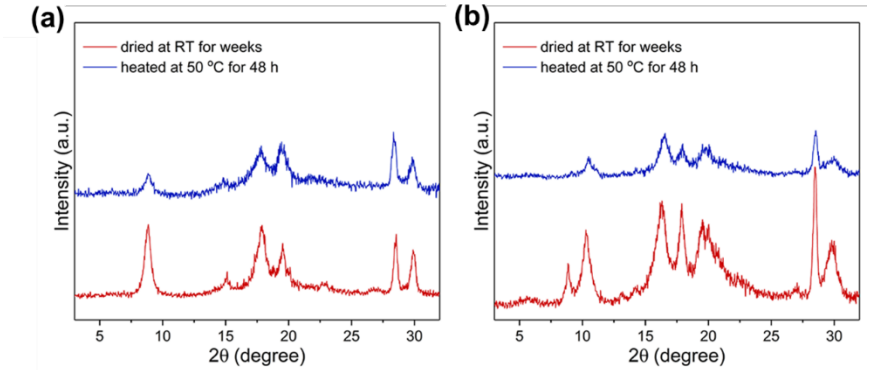

Figure 3.12 XRD patterns showing effect of aging and heating in intercalation product obtained in (a) 2-propanol and (b) acetone.

Another possibility in above energetics consideration is that a portion of the intercalated ferrocene in 2-propanol may have not been oxidized, thus the strong electrostatic repulsion mentioned above will be partially alleviated. This seems to be true according to XPS measurements (Figure 3.13), which reveal that, despite higher V^{4+}/V^{5+} ratio in the 2-propanol intercalation product as expected from higher extent of intercalation, there is a large amount of intercalated ferrocene that has not been oxidized. However, the conclusion is questionable as it is well known that XPS only probes surficial oxidation states and cannot account for redox reactions occurring within the bulk of the microcrystals.

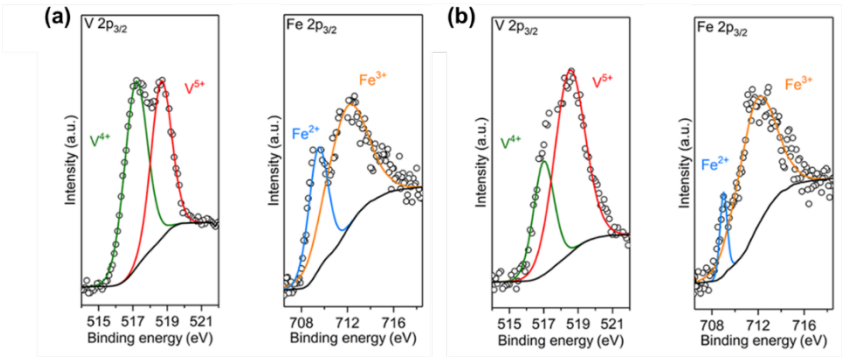

Figure 3.13 XPS spectra of intercalation product in (a) 2-propanol and (b) acetone.

The origin for the observed much faster intercalation kinetics in 2-propanol remains elusive. Both 2-propanol and acetone cannot be incorporated into $VOPO_4 \cdot 2H_2O$ alone under current intercalation conditions, excluding the possiblity of forming stable pre-expanded hosts by solvent molecules.[70] In considering solvent-host interaction, 2-propanol is known to effectively exfoliate $VOPO_4 \cdot 2H_2O$ under sonication,[103] thus it may lower the energy needed for layer sliding, which plays an important role in exfoliation of layered materials,[104] as well as in the formation of intercalated products. The solvent-host interaction may also be electronic in nature. For example, a recent study reveals that relative difference in electronegativity between solvents and TMDs is able to drive the transfer of electrons from or to the hosts, affecting their intrinsic properties.[105] This may be highly relevant in current ferrocene-$VOPO_4$ system, which features a redox intercalation mechanism involving electron transfer. Another possible angle to consider is solvent-intercalant interaction, such as desolvation of ferrocene as a prerequisite before intercalating into $VOPO_4 \cdot 2H_2O$ host. In this regard, a higher solvation energy may lead to a slower intercalation rate. Finally, for the pre-existing water molecules in the host, though unlikely to interact with ferrocene, their removal to allow the proceeding of intercalation may be affected by solvent. A more complete picture revealing the role of solvent requires understanding of intercalation product in the initial stage, where in situ characterizaiton will be the most suitable probing methodology.[106]

To conclude, we have investigated the unique solvent-dependent intercalation of ferrocene into layered $VOPO_4 \cdot 2H_2O$. From a thermodynamic point of view (Figure 3.14), the overall intercalation process involves a net release of energy resulted from summation of the ionization potential of ferrocene, the electron affinity of $VOPO_4$ host, and the electrostatic energy of the charge-separated intercalant-host pair. Kinetically, different solvents drive this process along distinct pathways, as demonstrated by 2-propanol and

acetone employed in this work. This solvent effect, though attracted little attention in previous studies, is hypothesized to play a critical role in several kinetically important steps, such as desolvation, layer sliding and electron transfer, during the intercalation. The observed solvent-dependence also leads to a verdict on the orientation of intercalated ferrocene molecules.

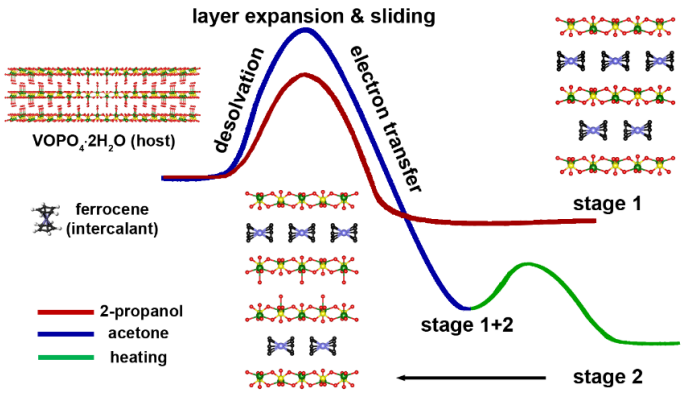

Figure 3.14 Solvent-dependent kinetic and thermodynamic diagram for ferrocene intercalation into $VOPO_4 \cdot 2H_2O$.

3.3 Ultrafast Intercalation Enabled by Strong Solvent-Host Interaction

In this part, investigation of ferrocene intercalation into $VOPO_4 \cdot 2H_2O$ was extended to a variety of common solvents with a special focus on primary alcohols. From methanol to 1-hexnaol, intercalation rate was observed to peak in 1-propanol. Interestingly, similar kinetics of exfoliation was also found under the same conditions of intercalation without ferrocene. The correlation between intercalation and exfoliation was understood at atomic level via DFT calculations, which revealed the possible joint roles of pre-intercalated solvent may have played in intralayer interactions, interlayer expansion and layer sliding.

The essence of this part of research is to explain solvent effects on the kinetics of ferrocene intercalation into $VOPO_4 \cdot 2H_2O$. This intercalation system differs from many previous studies on solvent effects in terms of the size of the intercalant. While intercalation of small cations is usually accompanied by solvent co-intercalation as a result of strong solvation,[107, 108] ferrocene has a much larger size that excludes such possibility. This feature largely eliminates the complexity from solvent-guest interaction, while any displaying solvent effect is likely due to solvent-host interaction only.

The synthesis of $VOPO_4 \cdot 2H_2O$ microcrystals and the room-temperature intercalation reactions were carried out in a similar way as in previous section. A special note in this study is that for solvents with relatively high boiling point, acetone was used as the washing solvent to collect product powder for the purpose of thorough drying. In all of the products (denoted as fc-$VOPO_4$ as before), a dilation of the host is usually observed (Figure 3.15a) by SEM. A typical high-resolution cross-sectional TEM image of the fully intercalated structure is shown in Figure 3.15b, from which a layer separation of 9.79 Å (vs 7.41 Å $VOPO_4 \cdot 2H_2O$) is determined. Due to the intercalation induced (½, ½, 0) layer transition concluded previously, the unit cell of fc-$VOPO_4$ consists of two non-overlapping layers of ferrocene (B and B′) sandwiched between three $VOPO_4$ layers (A, A′ and A), twice as large as that in $VOPO_4 \cdot 2H_2O$. The phase change probed by XRD shows that the lines representing basal planes shift to lower angles after intercalation (Figure 3.15c). The calculated interlayer distance based on the (002) peak ($2\theta = 9.04°$) in fc-$VOPO_4$ matches well with the value obtained from TEM. The observation of the yellow $VOPO_4 \cdot 2H_2O$ powder turning green indicates the intercalation is a redox process.[79] As plotted in Figure 3.15d, V K-edge X-ray absorption near-edge spectra recorded by synchrotron-based XAS suggests the reduction of V^{5+} to V^{4+} following the pre-edge peak shift after intercalation.[109] Similarly, Figure 3.15e plots the pre-edge peak

shift in Fe K-edge spectra. In ferrocene and ferrocene derivatives, it has been previously reported that the pre-edge peaks are affected by both substituents at the cyclopentadienyl ring and the oxidation state of Fe.[110] In this study, the pre-edge peak shift is unambiguously attributed to the oxidation of Fe^{2+} to Fe^{3+} with concomitant reduction of vanadium.

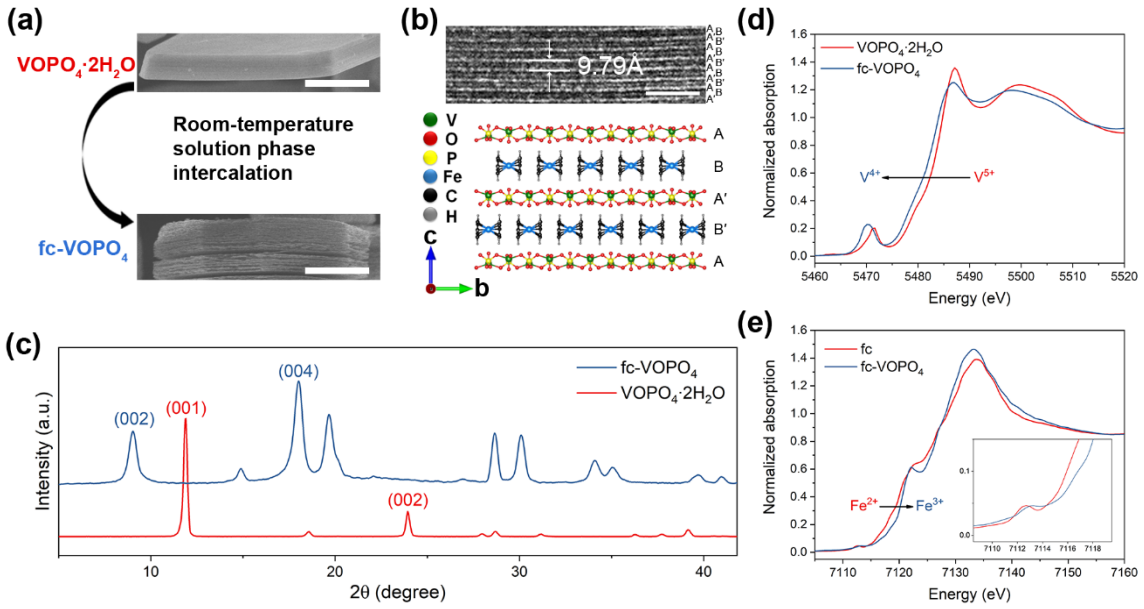

Figure 3.15 (a) Representative SEM images of $VOPO_4{\cdot}2H_2O$ microcrystals before and after intercalation. Scale bar: 1 μm. (b) Cross-sectional TEM image of fc-$VOPO_4$ showing the interlayer distance and corresponding schematic atomic structure. Scale bar: 5 nm. (c) Powder XRD patterns of $VOPO_4{\cdot}2H_2O$ and fc-$VOPO_4$. (d), (e) V K-edge and Fe K-edge X-ray absorption near-edge spectra before and after intercalation.

The rate of solution color change associated with the charge transfer mechanism has also shown the importance of solvent in the intercalation process. In a variety of common solvents, the reaction has been found to differ significantly in the rate of color change, thus proceed to drastically different extent. For a fixed 48 h intercalation time,

the intercalated phases identified by XRD span from non-intercalated (e.g. in DMSO) to fully intercalated (e.g. in 1-propanol) with many intermediate ones (Figure 3.16a). These products are compared quantitatively in terms of extent of intercalation, which was previously defined as the amount of intercalated ferrocene per $VOPO_4$ unit (denoted as fc/$VOPO_4$) and was experimentally determined as Fe/V atomic ratio by EDS. In the plot of fc/$VOPO_4$ with respect to polarity, which was an important factor previously discussed in solution phase intercalation,[7] no clear trend could be straightforwardly spotted (Figure 3.16b). The same is true when other common physical properties, for example, dielectric constant, are considered. Therefore, other factors from chemical or structural aspects are almost certainly involved. Primary alcohols from methanol to 1-hexanol are chosen to explore the observed solvent effects in detail for their generally high extent of intercalation as well as a non-monotonic curve in plotting fc/$VOPO_4$ vs the number of carbon (Cn).

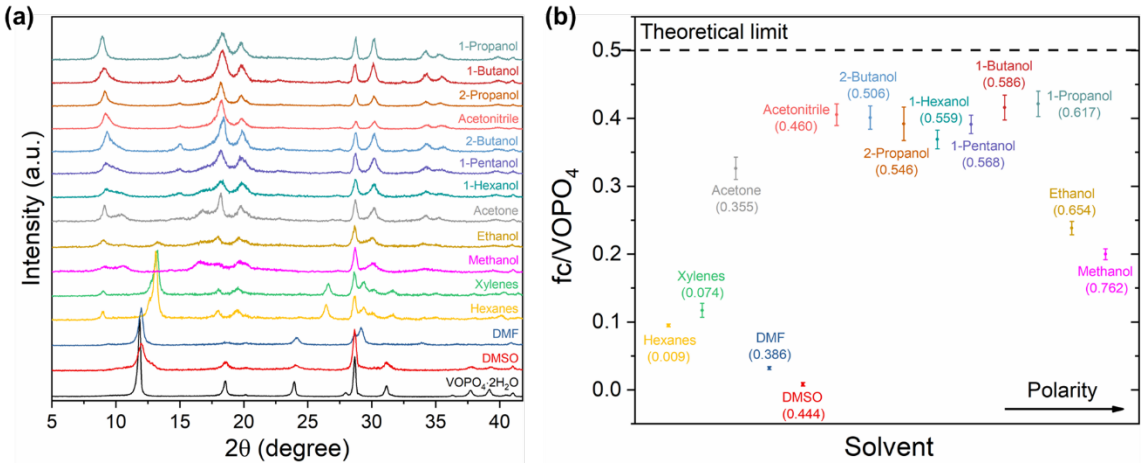

Figure 3.16 (a) Powder XRD patterns of fc-VOPO4 obtained in various solvents after 48 h intercalation. (b) Summary of extent of intercalation in various solvents. The solvents are arranged in the order of increasing polarity (number in the bracket) from left to right.

The solvent dependence of the intercalation in primary alcohols is best illustrated in kinetic plot of fc/$VOPO_4$ vs time (Figure 3.17), from which several solvents showing similar long-time extent of intercalation can be differentiated.

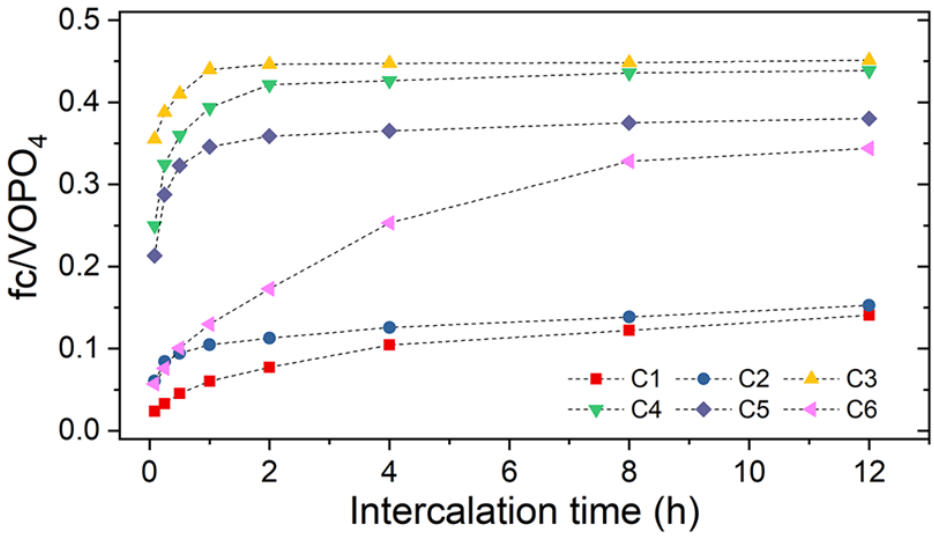

Figure 3.17 Intercalation kinetics in primary alcohols from C1 to C6.

The six primary alcohols fall into three groups based on their effectiveness (extent of intercalation) and efficiency (intercalation rate): 1-propanol (C3), 1-butanol (C4) and 1-pentanol (C5) belong to a group with both high effectiveness and efficiency; 1-hexanol (C6) itself is a group showing high effectiveness but low efficiency; methanol (C1) and ethanol (C2) form a group with both low effectiveness and efficiency. In accordance with the EDS measurements, phase evolutions in each solvent probed by ex situ XRD also confirm the same trend in kinetics (Figure 3.18). In particular, 1-propanol manifests an impressively ultrafast intercalation process in which a complete phase transformation is attained within 5 min. The phase evolution in ethanol is peculiar as the peaks associated

with ferrocene intercalation are not as clear as in other cases. It seems that intercalation of ferrocene in ethanol leads to a product with very poor crystallinity.

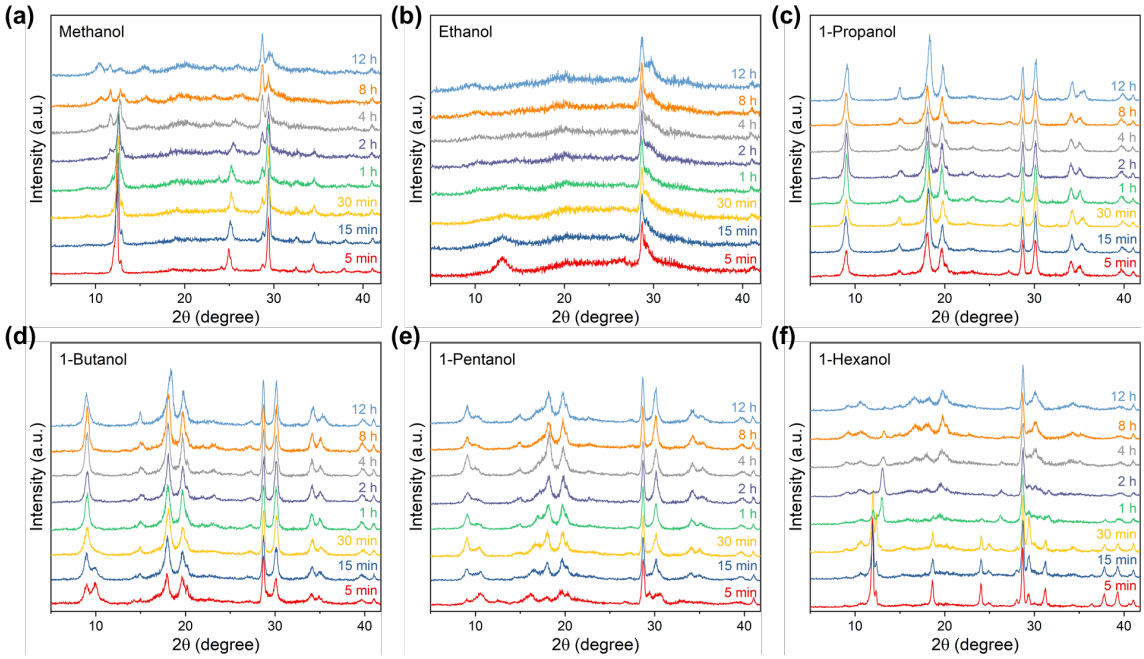

Figure 3.18 Time-dependent XRD patterns of the intercalated structures in all six tested primary alcohols.

The intercalation mode is revealed in slow solvents by elemental mapping of a microcrystal at the early stage of intercalation (1 h in 1-hexanol) and corresponding line scan (Figure 3.19a), showing a clear 2D diffusion pattern with less ferrocene distribution in the center of the microcrystal. The same elemental mapping taken at a later stage (4 h in 1-hexanol) shows a uniform distribution of ferrocene in the whole microcrystal, although the intercalation has not yet reached completion (Figure 3.19b). This implies that the intercalation is no longer diffusion controlled but limited by other steps, for instance, the ferrocene intake at the edge of the host.

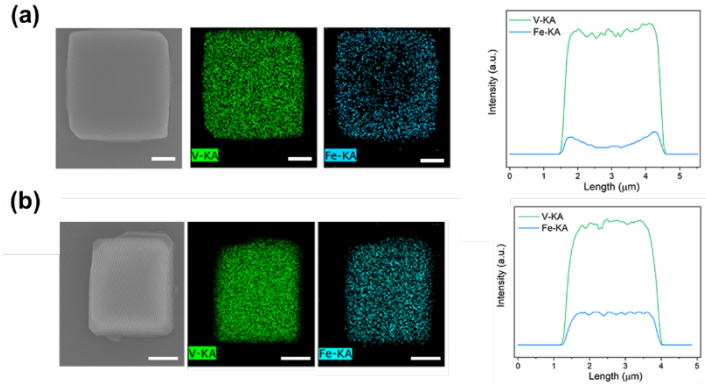

Figure 3.19 EDS elemental mapping and line scan over the center of a microcrystal after (a) 1 h intercalation in 1-hexanol and (b) 4 h intercalation in 1-hexanol. Scale bar: 1 μm.

The same classic 2D diffusion model used in last section can be used to calculate relative rate constants (Figure 3.20a) and quantitatively compare the intercalation kinetics among the solvents. It should be noted that, the 2D diffusion model holds only for the initial period of intercalation. The fitting for ethanol may seem unreasonable due to its initial high efficiency but overall low effectiveness. Despite the complexity in the overall process, the volcano shape of the (initial) intercalation rate vs Cn plot (Figure 3.20b) peaking at C3 (80 times faster than C1) is rather intriguing.

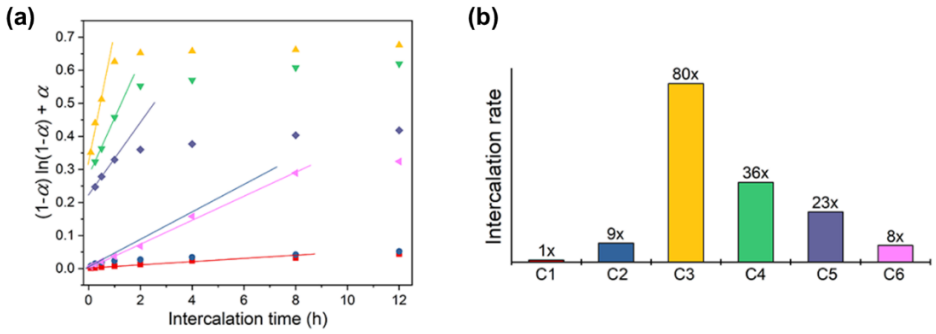

Figure 3.20 (a) Kinetic modeling using 2D diffusion model, as plotted by $(1-\alpha)\ln(1-\alpha)+\alpha$ vs time, where α is defined by $\frac{fc/VOPO_4}{0.5}$. (b) Comparison of relative rate constants in primary alcohols normalized with respect to methanol (C1).

To explore possible solvent-host interaction that may exist in this study, $VOPO_4 \cdot 2H_2O$ microcrystals were stirred in pure solvents following exactly the same conditions as the intercalation. Surprisingly, color fading was observed and, in some cases, very rapid even under such mild stirring (Figure 3.21), indicating exfoliation as a possible result of the solvent-host interaction.

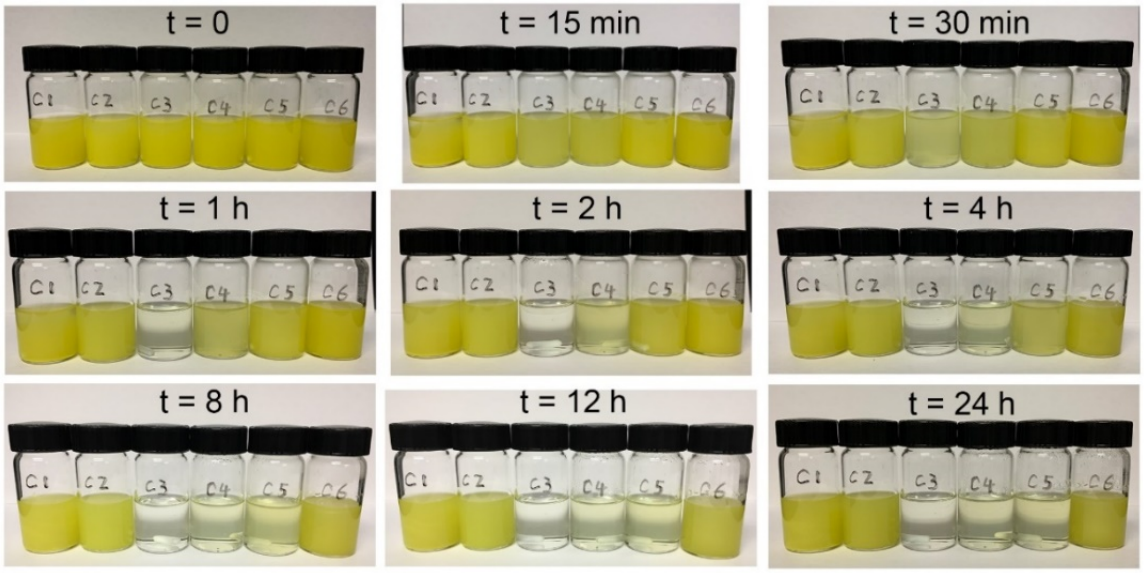

Figure 3.21 Digital photos taken at various time intervals in the process of stirring $VOPO_4 \cdot 2H_2O$ in primary alcohols without ferrocene.

After specified stirring time was reached, the solution was centrifuged at 3000 rpm for 30 min, and the upper solution was collected, leaving bottom particles to be completely dried and weighed. Indeed, the upper solution extracted from 1-proanol after stirring for 30 min contains a product displaying typical nanosheets morphology with thin thickness (Figure 3.22a). Products with similar morphology could also be found in all primary alcohols after stirring for 24 h (Figure 3.22b).

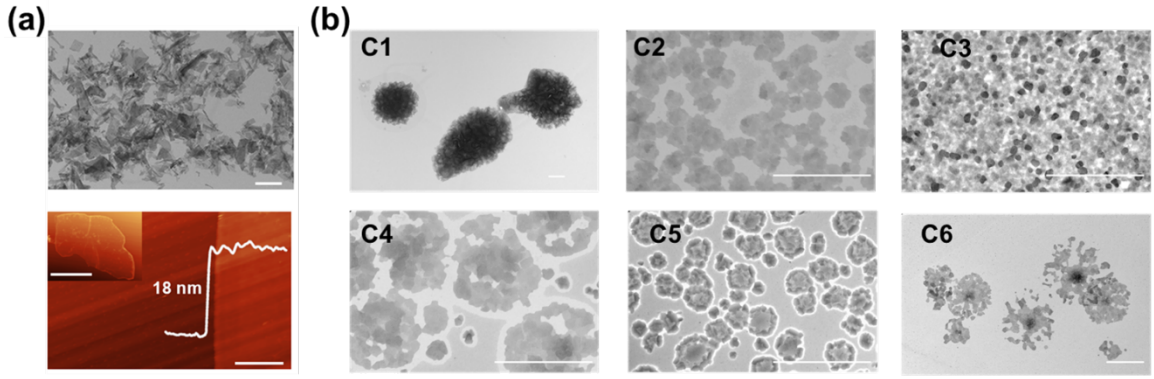

Figure 3.22 Exfoliation of $VOPO_4 \cdot 2H_2O$ in pure solvents (a) Top: SEM image of thin nanosheets found after stirring $VOPO_4 \cdot 2H_2O$ in C3 for 30 min. Scale bar: 1 μm. Bottom: AFM height profiling of an exfoliated nanosheet. Scale bar: 100 nm. Inset: AFM image of the whole nanosheet. Scale bar: 500 nm. (b) SEM images of thin nanosheets found after stirring $VOPO_4 \cdot 2H_2O$ in primary alcohols for 24 h. Scale bar: 1 μm.

The noticeable difference in the rate of color fading leads to a similar kinetic plot for the exfoliation process (Figure 3.23), where extent of exfoliation refers to the weight percentage of exfoliated $VOPO_4 \cdot 2H_2O$ with respect to the total $VOPO_4 \cdot 2H_2O$ added to the stirring solution, and the weight of exfoliated $VOPO_4 \cdot 2H_2O$ can be calculated by subtracting the weight of bottom particles (unexfoliated microcrystals) from the total mass. Interestingly, the plot of exfoliation kinetics shares some striking similarities with that of intercalation kinetics: the solvents (C3, C4 and C5) that are effective and efficient in intercalation also appear to be so in exfoliation, implying a strong correlation between the two processes.

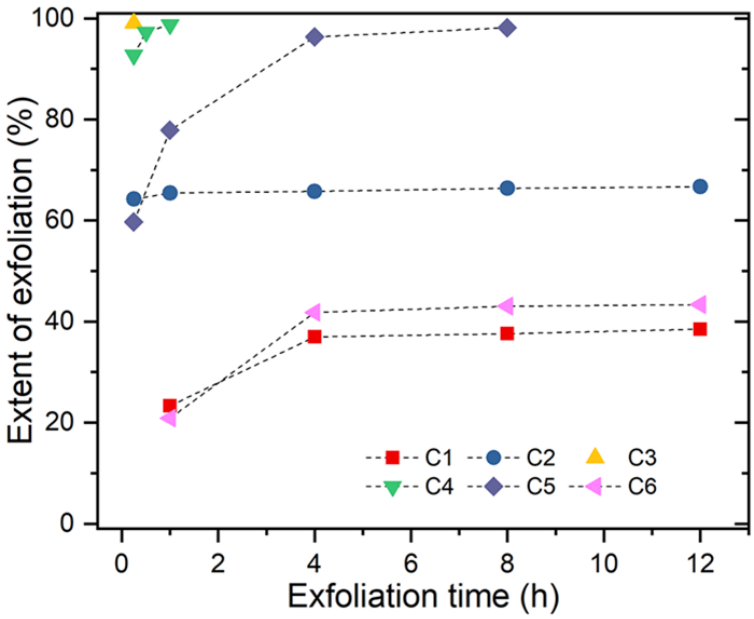

Figure 3.23 Exfoliation kinetics in the same primary alcohols used in intercalation.

In analyzing solution phase intercalation, it is useful to consider it as a three-body (host, solvent and guest) system where interaction between either two bodies may be significant for the kinetics of overall process. For a hydrate host like $VOPO_4 \cdot 2H_2O$, the situation is trickier as the interlayer is pre-intercalated with H_2O molecules, adding an even higher degree of complexity. As the intercalation of ferrocene requires removal of interlayer H_2O, it is natural to consider whether this process is the rate-limiting step, thus the kinetic analysis will be reduced to solvent-H_2O interaction. To prove or disprove this point, gas-phase intercalation was carried out in a home-built CVD system where a vacuum pump was used to both dehydrate $VOPO_4 \cdot 2H_2O$ and carry ferrocene gas flow (due to sublimation) toward $VOPO_4 \cdot 2H_2O$ (Figure 3.24a). The phase evolutions during dehydration and dehydration/intercalation were probed by performing ex situ XRD on product powders without any washing procedure. It has been found that under the same vacuum condition, the intercalation does not keep pace with the dehydration and the latter

is apparently faster, indicating H_2O removal is unlike the key kinetic step during intercalation (Figure 3.24b and c).

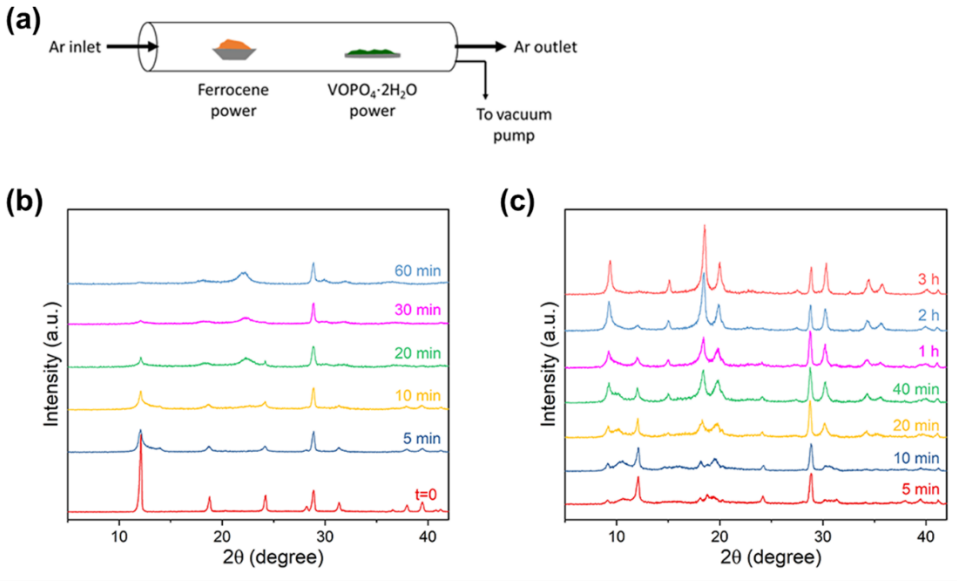

Figure 3.24 (a) Experimental setup for gas phase intercalation. Time-dependent XRD patterns of (b) dehydrated (pure $VOPO_4 \cdot 2H_2O$ only) and (c) intercalated structures (with ferrocene).

Intake of solvent molecules into a layered material is germane to its exfoliation in this solvent.[111, 112] Therefore, the kinetics of solute (guest) intercalation is likely to be dictated by the solvent-host interaction. In intercalation of ferrocene into $VOPO_4 \cdot 2H_2O$, however, the event of solvent intake is probably transient, as there is no experimental evidence for any intermediate structures caused solely by solvent molecules (in situ)[96] or solvent co-intercalation in the final products (ex situ, as shown in section 3.2). It is hypothesized that for large intercalants like ferrocene, its solution phase intercalation into a layered host is initiated by pre-intercalation of solvent molecules but not in the form of

bimolecular configuration that was previously found under microwave field or heating condition.[65, 113] It is further considered that, the exfoliation of $VOPO_4 \cdot 2H_2O$, though possible under conditions used in this study, is not a step prior to ferrocene intercalation. Namely, the intercalation does not proceed via exfoliation-restacking mechanism.[114] This is because neither exfoliated nanosheet was detected in the intercalation process, nor adding ferrocene to exfoliated nanosheets solution was able to produce a similar product as in direct intercalation.

First-principles DFT calculations were carried out to unravel above proposed solvent pre-intercalated structures. All theoretical simulations were based on spin-polarized density functional theory calculations implemented by the Vienna ab initio simulation package (VASP).[115] The exchange-correlation functional adopted the formula of Perdew-Burke-Ernzerhof in the framework of the generalized gradient approximation.[100] The projected augmented wave method[116] with a cutoff energy of 520 eV was set to solve the wavefunction at the ground state. Meanwhile, empricial Grimme method (DFT-D3)[117] was used to consider the weak van der Waals interaction in the systems. The convergence thresholds of total energy and force were 10^{-4} eV and -0.05 eV/Å, respectively. Moreover, the Gaussian smearing with a width of 0.05 eV was used to accelerate the electron occupations. Gamma-centered Monkhorst-Pack method[118] was used to sample a 5x5x4 mesh in the reciprocal space.

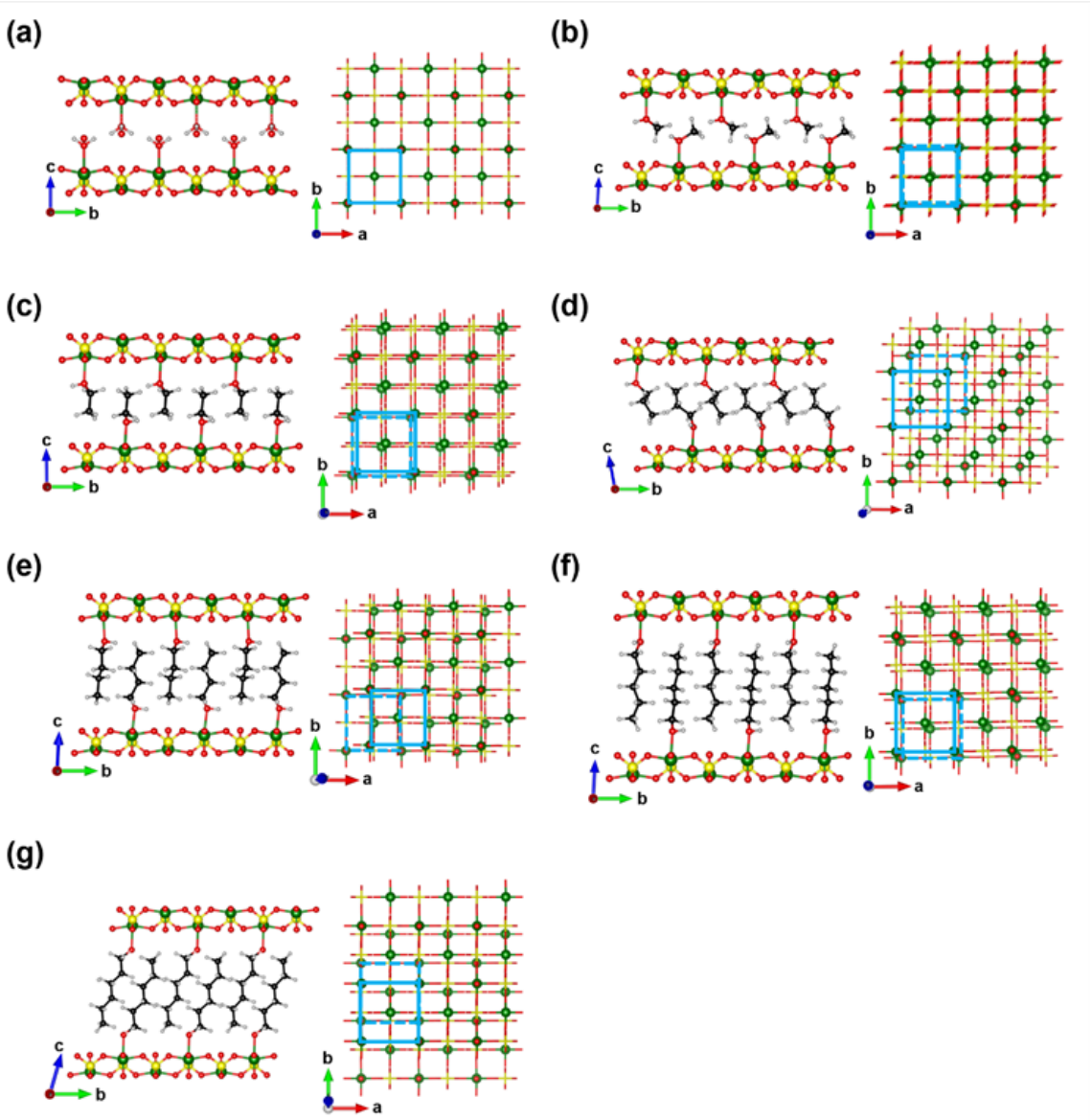

Figure 3.25 Theoretical modeling of (a) $VOPO_4 \cdot 2H_2O$ and (b)~(g) solvent-intercalated structures in the order of C1~C6 with monomolecular configuration viewed along the *a*-*b* plane and resulting layer sliding (solid blue square vs dashed blue square) viewed along the *c* axis.

It has been found that the intake of solvent molecules, in most cases, is energetic-favorable to replace original interlayer water, forming monomolecular configuration. Such accommodation of solvent molecules introduces structural alterations to the host, such as expansion of interlayer distance and sliding between two adjacent planes. The calculated structures and detailed results for all six primary alcohols, together with those in the original structure of $VOPO_4 \cdot 2H_2O$, are summarized in Figure 3.25 and Table 3.2.

	Layer-layer interaction (eV)	Host-solvent interaction (eV/mol)	Solvent-solvent interaction (eV/mol)	Interlayer distance (Å)
$VOPO_4 \cdot 2H_2O$	-109.98	-1.621	-0.3546	7.41
C1	-109.93	-1.979	-0.1342	7.64
C2	-109.91	-1.965	-0.1339	9.03
C3	-109.92	-1.825	-0.1602	9.72
C4	-109.90	-1.654	-0.2257	11.6
C5	-109.89	-1.553	-0.2586	13.0
C6	-109.93	-1.452	-0.3902	13.9
fc-$VOPO_4$	N.A.	N.A.	N.A.	9.77

Table 3.2 Intralayer interactions and interlayer distances in $VOPO_4$ related structures.

Figure 3.26a shows the interactions (normalized with respect to $VOPO_4 \cdot 2H_2O$) between adjacent $VOPO_4$ layers, layer and intercalated solvent, and solvents molecules themselves. Layer-layer interaction is seen to be invariant across all cases, suggesting that layer stability is mainly dictated by the guest-guest interaction, which increases from C1 to C6 as expected from the nature of van der Waals interactions between the alkyl chains. Noticeably, the guest-guest interactions for C1~C5 are substantially smaller than that in

$VOPO_4{\cdot}2H_2O$, in which the H_2O molecules are interacted through hydrogen bonding.[41] The host-guest interaction, namely strength of the V-O bond, decreases as the number of carbon increases, with C1~C3 showing higher values than that in $VOPO_4{\cdot}2H_2O$. Summation of the two interactions gives the tendency of exfoliation as higher host-guest interaction (easier to intercalate into layers) and lower guest-guest interaction (easier to separate layers) tend to push the process forward. However, methanol with the highest exfoliation tendency exhibits unexpected low effectiveness experimentally.

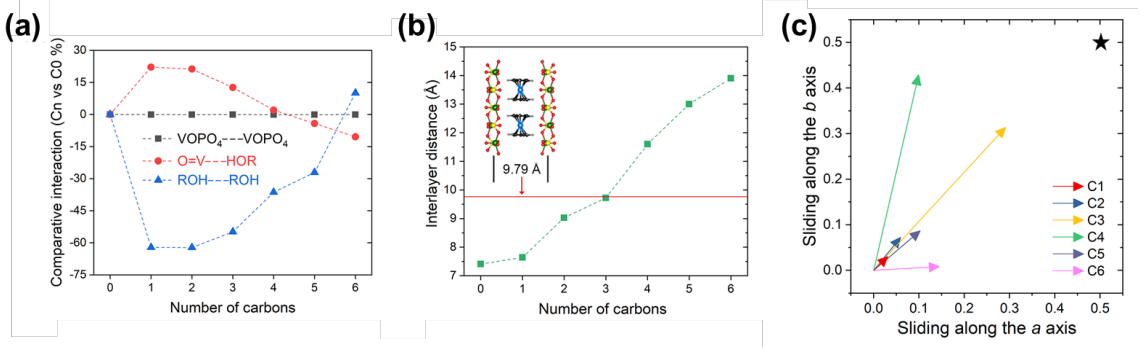

Figure 3.26 (a) Normalized interactions between two adjacent layers, layer and solvent, and solvent molecules compared with $VOPO_4{\cdot}2H_2O$ (denoted as C0, and H_2O is considered as intercalated solvent). (b) Calculated interlayer distances. Inset: interlayer distance of fc-$VOPO_4$. (c) Quantitative representation of layer sliding induced by solvent intercalation. Black star: required layer transition in the formation of fc-$VOPO_4$.

Change of interlayer distance as a result of solvent pre-intercalation has huge impact on subsequent ferrocene intercalation, for which the required interlayer expansion imposes perhaps the largest energy barrier.[79] As shown in Figure 3.26b, based on the monolayer configuration, intake of primary alcohols has been shown to enlarge the separation between adjacent $VOPO_4$ layers in the order of increasing length of carbon chain. For C1 and C2, the resulting expansion is below the required value to

accommodate ferrocene (red line). This could be a viable explanation for the slow intercalation kinetics in these two solvents. C6 exhibits similar poor exfoliation power as C1, however, intercalation of ferrocene proceeds more rapidly in C6 due to the larger interlayer expansion by solvent pre-intercalation.

Figure 3.26c compares the sliding between adjacent layers as a consequence of guest-guest interaction. The magnitude of sliding is seen to be smallest in C1, and largest in C3 and C4. As sliding energy barrier needs to be overcome in layer separation,[119] the small magnitude of sliding in C1 could be a plausible explanation for its substantially weak exfoliation power. In contrast, the top speed in both exfoliation and intercalation in C3 is originated from the large magnitude of sliding and the direction matching to the required sliding in forming fc-$VOPO_4$ (black star). It should be pointed out that, such solvent effect may be less significant or even insignificant when the exfoliation is aided with external forces. For instance, $VOPO_4{\cdot}2H_2O$ has been shown to be completely exfoliated indiscriminately in C1, C2 and C3 under strong ultrasonication.[103]

In summary, the rate of ferrocene intercalation into $VOPO_4{\cdot}2H_2O$ has been shown to follow a volcano shape vs the number of carbons in primary alcohols (C1~C6), among which 1-propanol (C3) promotes an ultrafast intercalation featuring complete phase transformation within 5 min. The trend is almost consistent with that in the exfoliation of $VOPO_4{\cdot}2H_2O$, especially in the solvents (C3~C5) that are highly effective/efficient for the intercalation. Pre-intercalated solvent molecules between $VOPO_4$ layers with monomolecular configuration has been proposed to correlate the strong solvent-host interaction and the fast intercalation. The solvent effect is understood as the sum of intralayer interactions (tendency for exfoliation), interlayer expansion (requirement for intercalation) and layer sliding (a necessity in both exfoliation and intercalation).

3.4 CONCLUSION

Intercalation of ferrocene in $VOPO_4 \cdot 2H_2O$ undergoes as a redox topotactic reaction with electron transfer from ferrocene to the $VOPO_4$ layers, which are also expanded during the process due to the large size of the intercalant. This particular pair of host-guest exemplify an interesting intercalation system showing strong solvent dependent intercalation kinetics. The solution-phase intercalation studied in acetone and 2-propanol brings a deeper understanding of the intercalation pathways and associated intercalated structures, which were either uncovered or wrongly interpreted in previous studies. Offering features like tunable composition/structure and possible dual electrochemical activity, this model organic−inorganic superlattice represents a huge family of artificial materials that can benefit from wide choices of organic intercalants, meriting their feasibilities in many technological applications. Fundamentally, the observed solvent-influenced interplay between kinetic and thermodynamic processes could potentially attract broad research interests into materials engineering enabled by controlled intercalation. The extended study in primary alcohols, where influence of solvents in intercalation and exfoliation kinetics is understood at atomic level, not only shows the intriguing solvent effects in solution-phase intercalation involving strong solvent-host interaction, but also highlights the possibility of achieving ultrafast intercalation by rational selection of solvent.

Chapter 4: Alkali-ion storage in $MOPO_4$*

4.1 Introduction to 2D Layered materials for electrochemical energy storage

2D layered materials provide planar diffusion channels for storing charge-carrying ions between their layers, rendering them potential electrode materials for EES devices. Despite such structural advantage, the practical performance of 2D materials is not always satisfactory, and sometimes is largely restrained by their intrinsic properties. Many factors need to be considered when evaluating the potential of a 2D layered material for EES, including charge storage capability, kinetics of intercalation of charge-carrying ions, reversibility of the intercalation process, electrical conductivity, cost of the materials, etc.

Layered $VOPO_4$ system has long been used as a platform for studying intercalation chemistry as already introduced in Chapter 3. It has also emerged as one of the most promising alternative cathode materials for rechargeable lithium batteries because of its stable layered structure that can facilitate Li-ion transport process, high redox potential due to the inductive effect of strong P–O covalent bonds, and low cost and environmental friendliness.[120] Research on the electrochemical properties of layered $VOPO_4$ was initiated in $VOPO_4 \cdot 2H_2O$,[58, 121] and has been later focused on the anhydrous form α_I-$LiVOPO_4$.[122-124] The dihydrate form, despite its wide-open structure with a larger interlayer distance and a higher conductivity than that of anhydrous form, has been

* This chapter includes contents from following manuscripts published:
Y. Zhu, L. Peng, D. Chen, G. Yu, "Intercalation Pseudocapacitance in Ultrathin $VOPO_4$ Nanosheets: Toward High-Rate Alkali-Ion-Based Electrochemical Energy Storage", *Nano Lett.* 2016, 16, 742.
L. Peng†, Y. Zhu†, X. Peng, Z. Fang, W. Chu, Y. Wang, Y. Xie, Y. Li, J. Cha, G. Yu, "Effective Interlayer Engineering of Two-Dimensional $VOPO_4$ Nanosheets via Controlled Organic Intercalation for Improving Alkali Ion Storage", *Nano Lett.* 2017, 17, 6273 (†equal contribution).
Y. Zhu participated in the experimental work and the preparation of manuscripts.

previously shown to exhibit moderate specific capacity but very limited cycling stability.[58, 125]

Exfoliating 2D layered materials into few-layered or monolayered nanosheets can effectively expose interior area with maximum possible active sites, and the size reduction provides better adhesion with electrode, higher contact area with electrolyte, shortened pathways for electronic and Li-ion transport, and better accommodation of strain induced by intercalation/deintercalation processes.[126] Accessible interlayer space of 2D materials offers abundant electrochemical active sites on which most energy storage systems rely entirely for their performance. As a rule of thumb, a larger interlayer space provides higher accessibility and a lower diffusion barrier, a guideline especially useful in engineering materials for transport and storage of large ions. This idea has been pioneered by several studies on interlayer-expanded 2D materials for sodium-ion batteries (SIBs).[127, 128] It is soon realized that this concept aligns well with intercalation chemistry as many guest molecules enlarge the interlayer distance of the hosts during this process. Therefore, expanding interlayer space of 2D materials by means of intercalation serves as another effective structural engineering approach.

This chapter reports the exploration of $MOPO_4$ as a charge storage host. The electrochemical properties have been investigated in the nanosheets of $MOPO_4$ hydrates with benefits from above mentioned nanostructuring and interlayer architecting strategies. As presented in Chapter 2, while the as-synthesized $NbOPO_4$ hydrates are intrinsically nanosheets in morphology, effective exfoliaiton method for producing $VOPO_4{\cdot}2H_2O$ nanosheets from the as-synthesized microcrystals is required. Solution-phase exfoliation described in Chapter 3 provides valuable insights into the search for suitable exfoliaiton solvents. Among many commonly available alcohols, 2-propanol has been identified as the best candidate to serve this role.

4.2 INTERCALATION PSEUDOCAPACITANCE IN EXFOLIATED $VOPO_4$ NANOSHEETS

Pseudocapacitance arises when reversible redox reactions occur at or near the surface of a material in contact with an electrolyte, or when these reactions are not limited by solid-state ion diffusion. A classic example for pseudocapacitance is hydrous RuO_2, in which the storage of protons from the electrolyte resulted in a faradaic charge-transfer reaction on the electrode.[129] Inspiringly, during the past few years, a dramatic expansion in exploring materials that combine high energy/power density and long cycle life was witnessed in the energy storage field.[130] In particular, several materials were reported to possess pseudocapacitive charge storage that is not a diffusion-controlled process.[131, 132] This mechanism is named intercalation pseudocapacitance, in which ions intercalate into the tunnels or layers of a redox-active material accompanied by a faradaic charge-transfer with no crystallographic phase change.[17] It should be pointed out that in intercalation pseudocapacitance, the process kinetics is surface-controlled so that the overall behavior seems capacitive. Nevertheless, unlike conventional surface involved pseudocapacitance in supercapacitors, charge storage occurs inside the material for intercalation pseudocapacitance.

One intriguing feature provided by intercalation pseudocapacitive mechanism is the superior fast charge/discharge processes, which show great promise toward high-rate electrodes in LIBs. Very recently, this concept has been demonstrated in SIBs with TiO_2 nanomaterials.[133] So far, intercalation pseudocapacitive mechanism has been intensively explored in anode materials for LIBs and SIBs while report on cathode materials has been very limited. Here, we report the study of intercalation pseudocapacitance in a cathode material, $VOPO_4$ nanosheets exfoliated from bulk $VOPO_4 \cdot 2H_2O$, for alkali-ion based electrochemical energy storage. In contrast to bulk $VOPO_4$ materials studied previously, exfoliated $VOPO_4$ nanosheets do not suffer capacity decay and have much better rate

capability than the bulk counterpart in LIBs. We further demonstrate that pseudocapacitance dominates the charge storage process in $VOPO_4$ nanosheets cathode, contributing crucially to the excellent rate capability and long-term stability. We also extend the current application to SIBs, which has not been reported previously on this material. Meanwhile, these 2D $VOPO_4$ nanosheets represent a great platform for studying fundamental charge storage mechanism.

The morphology and structure characterization of as-synthesized bulk $VOPO_4{\cdot}2H_2O$ microcrystals and exfoliated $VOPO_4$ nanosheets are shown in Figure 4.1. The specific sample was synthesized using a mixture of V_2O_5 (4.8 g), H_3PO_4 (85%, 26.6 ml) and H_2O (115.4 ml) that was refluxed at 110 °C for 16 h (noted HNO_3 was not used as its role was not quite understood at the time when this study was carried out). To obtain exfoliated $VOPO_4$ nanosheets, bulk $VOPO_4{\cdot}2H_2O$ microcrystals were first ground to approximately 1 μm in size and then dispersed in 2-propanol with concentration about 2 mg/mL. The yellow dispersion was ultrasonicated in water baht for 30 min, during which color of the dispersion became faded, indicating successful formation of $VOPO_4$ nanosheets. Top-view scanning SEM image indicates bulk $VOPO_4{\cdot}2H_2O$ has a square shape with lateral size about 10 μm (Figure 4.1a). Side-view SEM image shows one single microcrystal with thickness about 1 μm, and more interestingly, it possesses lamellar structure with many tightly stacked layers (Figure 4.1b). This layering structure features an ideal framework for intercalation pseudocapacitive mechanism as the rigid equatorial planes do not reconstruct, namely there is no crystallographic phase change, during intercalation/deintercalation. Unlike 2D TMDs, for example MoS_2, in which layers are coupled by van del Waals forces and exfoliation usually requires significant effort,[134] weak hydrogen bonding in $VOPO_4{\cdot}2H_2O$ makes it much easier to exfoliate and corresponding thin nanosheets can be harvested in large quantity. For example, mild

heating (< 90°C) in alcohol is able to supply the energy to break the hydrogen bonds and homogeneous solutions containing the delaminated nanosheets can be obtained.[113] Here, our simple ultrasonication method is able to produce free-standing $VOPO_4$ nanosheets in 2-propanol. SEM image indicates the products after ultrasonication (drop-casted on SiO_2/Si substrate) have much thinner thickness (less than 10 nm) compared to the microcrystals (Figure 4.1c), and they show clearly sheet-like morphology with a lateral size of ~1 μm. Given the fact that no surfactant was added during ultrasonication, those nanosheets tended to form clusters. However, single nanosheets could be observed on diluted solution drop-casted on lacey carbon grid, as shown in the STEM image (Figure 4.1d). The nearly transparent feature of the nanosheets implies their ultrathin thickness.

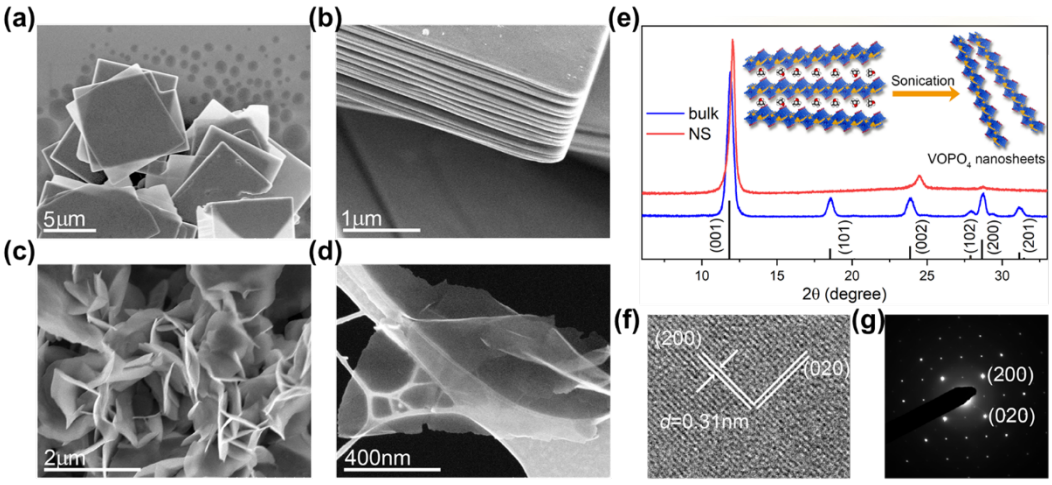

Figure 4.1 Morphological and structural characterization of $VOPO_4$ samples. (a) Top-view SEM images of as-synthesized $VOPO_4 \cdot 2H_2O$ microcrystals. (b) Side-view SEM image of one single microcrystal. (c) SEM image of exfoliated $VOPO_4$ nanosheets. (d) STEM image of one single free-standing $VOPO_4$ nanosheet. (e) XRD patterns of as-synthesized $VOPO_4 \cdot 2H_2O$ (bulk) and exfoliated $VOPO_4$ nanosheets (NS). Inset scheme shows the 2-propanol assisted exfoliation process. (f,g) High resolution TEM image and associated SAED pattern of the exfoliated $VOPO_4$ nanosheets.

The subtle structural change before and after the exfoliation could be revealed by XRD characterization, which was performed on powders of bulk $VOPO_4{\cdot}2H_2O$ microcrystals and exfoliated nanosheets drop-casted on glass substrate (Figure 4.1e). The XRD pattern of bulk $VOPO_4{\cdot}2H_2O$ microcrystals can be readily indexed into the tetragonal $VOPO_4{\cdot}2H_2O$ with the standard JCPDS card no. 84-0111 ($VOPO_4{\cdot}2H_2O$, space group *P*4/nmm). The XRD pattern of exfoliated nanosheets shows that only (00*l*) basal plane lines can be clearly observed, while (*h*0*l*) lines can no longer be seen. In the meanwhile, all the basal plane lines shift to higher angles in an unremarkable way, indicating a slight decrease of interlayer distance possibly due to loss of a small amount of interlayer H_2O molecules. The structural crystallinity of the exfoliated $VOPO_4$ nanosheets is revealed by TEM. High-resolution TEM image (Figure 4.1f) and selected area electron diffraction (SAED) pattern (Figure 4.1g) demonstrate the single crystalline nature of the nanosheets. The lattice spacing of 0.31 nm could be assigned to (200) crystal plane, matching the SAED pattern. Besides, the two planes of (200) and (020) in SAED pattern show 90° orientation angle, consistent with tetragonal crystal structure identified in the XRD pattern. The successful exfoliation in 2-propanol is now understood as a result of strong solvent-host interaction existed between $VOPO_4{\cdot}2H_2O$ and alcohols as detailed in Chapter 3. Compared with primary alcohols, 2-propanol is an effective but less efficient exfoliation solvent. This is advantageous if controlled exfoliation is needed. The solvent selection also takes ease of processing into consideration. In this regard, the low boiling point of 2-propanol makes it the best choice.

Previous investigations have been mainly devoted to oxides as electrode intercalation compounds for LIBs.[6] MOXO compounds (M = Ti, V, Nb, Mo; X = S, P, As), as a subgroup of tavorite-structured materials, offer open 2D or 3D frameworks that are suitable for lithium intercalation process. In particular, $VOPO_4$ is an attractive

cathode candidate with theoretical capacity of 166 mAh/g for one lithium insertion[135] and it can potentially reach higher energy density than $LiFePO_4$.[136] Earlier studies have shown that $VOPO_4 \cdot 2H_2O$ exhibited poor capacity renteion in LIBs, which was hypothesized to be caused by oxidation of interlayer H_2O moleclues.[58] However, the large microcrystals used in those studies may not be stable in the electrochemical test environment or during the electrochemical processes. Thus, the exfoliated nanosheets serve as a good control sample to verify the capacity degradation mechanism.

The $VOPO_4$ nanosheets electrode was prepared by adding Super P carbon and sodium carboxymethyl cellulose (CMC) directly into aforementioned 2-propanol dispersion after ultrasonication (weight ratio of $VOPO_4$: Super P: CMC = 80: 15: 5). While heated to remove excess 2-propanol, the mixture was thoroughly mixed in a Thinky centrifugal mixer to form a homogenous slurry, which was then casted on aluminum foil and dried in vacuum in the open air for 12 hrs. The bulk $VOPO_4 \cdot 2H_2O$ electrode was prepared by adding ground microcrystals, Super P carbon in CMC aqueous solution (the same weight ratio as nanosheets electrode), followed by similar mixing, casting and drying procedures. The typical mass loading was about 1.0 mg/cm^2. CR2032 coin cells were assembled inside an Ar-filled glove box using metallic Li/Na as anode. For lithium cells, Celgard 2500 was used as the separator, and Selectilyte A6 (Battery grade, BASF) was used as the electrolyte. For sodium cells, Waltman glassy fiber was used as the separator, and 1 M $NaClO_4$ dissolved in propylene carbonate with 2% fluoroethylene carbonate additive was used as the electrolyte. Electrochemical characterization was performed on LANHE battery cycler (CT2001A) and Bio-logic potentiostat (VMP3). All the coin cells were first charged/discharged at 0.1C once before further tests.

Indeed, the cell assembled from microcrystals electrode quickly loses nearly all its capacity in less than 25 cycles at 0.1C rate (Figure 4.2a). In contrast, the cell assembled from nanosheets electrode is able to maintain its capacity at the same rate. The electrochemical behavior of nanosheets electrode in potentiodynamic mode (0.02 mV/s) exhibits a multi-step intercalation process in the cyclic voltammetric (CV) profile (Figure 4.2b), similar with previous study on bulk $VOPO_4 \cdot 2H_2O$.[58] This seems to indicate the loss of water is unlike to be significant during the exfoliaiton of microcrystals into nanosheets.

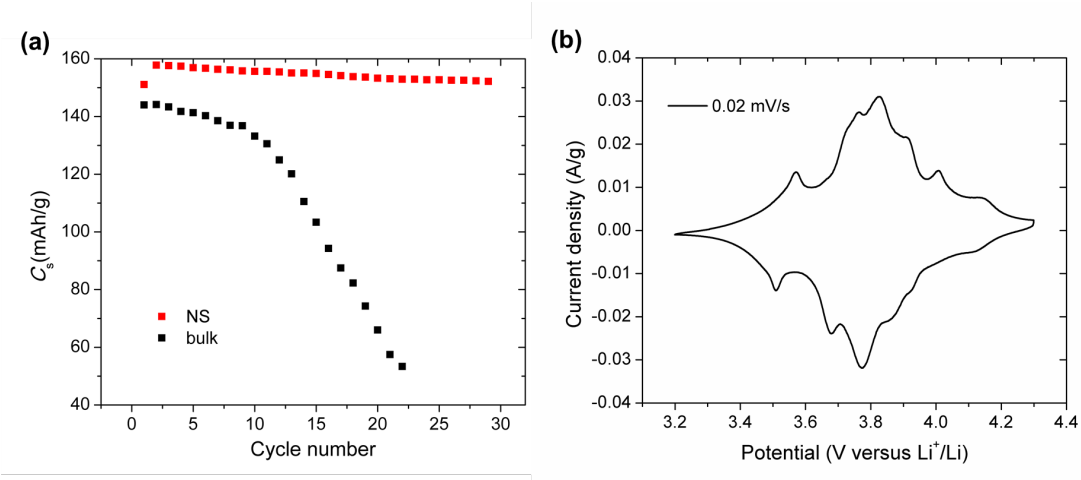

Figure 4.2 (a) Comparison of electrochemical stability in lithium cells between electrodes made from bulk microcrystals (black) and nanosheets (red), both were tested at 0.1C rate. (b) Cyclic voltammetric profile of nanosheets electrode at scan rate of 0.02 mV/s.

The observed multiple peaks in CV are also reflected in the charge/discharge profiles, in which at least three voltage plateaus can be seen at slow discharge rates, for example 0.1C (Figure 4.3). At a higher rate (0.1 mV/s), nanosheets and microcrystals electrodes show large differences (Figure 4.4a). The redox peak profile of nanosheets is much more symmetric and sharper than that of microcrystals and individual peaks can

still be resolved, while the latter only shows two broad bumps. Moreoever, for nanosheets electrode, the polarization between the charge/discharge curves is small (~130 mV), while for microcrystals electrode, the value is much larger (~320 mV). Both demonstrate that the redox kinetics is much better in nanosheets electrode. This can be explained as larger surface-to-volume ratio as a result of 2D thin nanosheet morphology compared to its bulk counterpart.

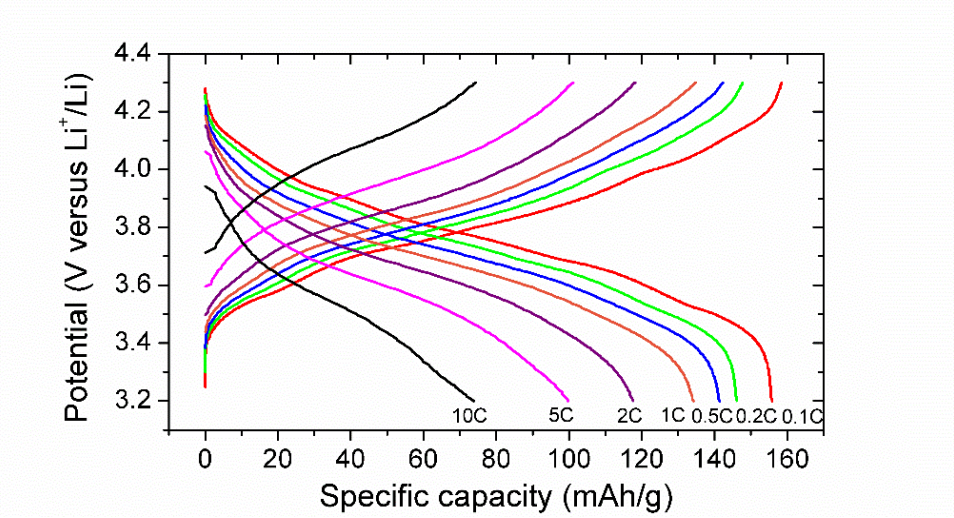

Figure 4.3 Charge/discharge profiles of the $VOPO_4$ nanosheets electrode in lithium cells at various current rates from 0.1C to 10C.

Such improved redox kinetics may contribute to the high capacity at high current densities, i.e. superior rate and cycling performance compared to bulk counterparts. This is clearly seen in the rate performance of the $VOPO_4$ nanosheets electrode versus the $VOPO_4 \cdot 2H_2O$ microcrystals electrode (Figure 4.4b). At relatively low current density of 0.1C, both electrodes deliver comparable reversible capacities, for instance, ca. 154 (93% of the theoretical value) and 141 mAh/g for nanosheets electrode and microcrystals electrode, respectively. However, the cell assembled from microcrystals electrode loses

nearly half of the initial capacity in less than 10 cycles at 0.1C rate. In contrast, the cell assembled from nanosheets electrode exhibits distinctly stable electrochemial performance, maintaining its capacity at the same rate. Impressively, the nanosheets electrode is able to deliver reversible capacities of 154, 146, 141, 133, 118, 99 and 74 mAh/g at C rate of 0.1, 0.2, 0.5, 1, 2, 5 and 10, respectively, while microcrystals electrode only delivers less than 70 mAh/g at 0.2C rate and is barely rechargeable at the current rate higher than 5C. In addition, the average reversible capacity of nanosheets reaches approximately 100 mAh/g at a current rate of 5C and is sustained for 500 cycles with no obvious capacity decay (Figure 4.4c).

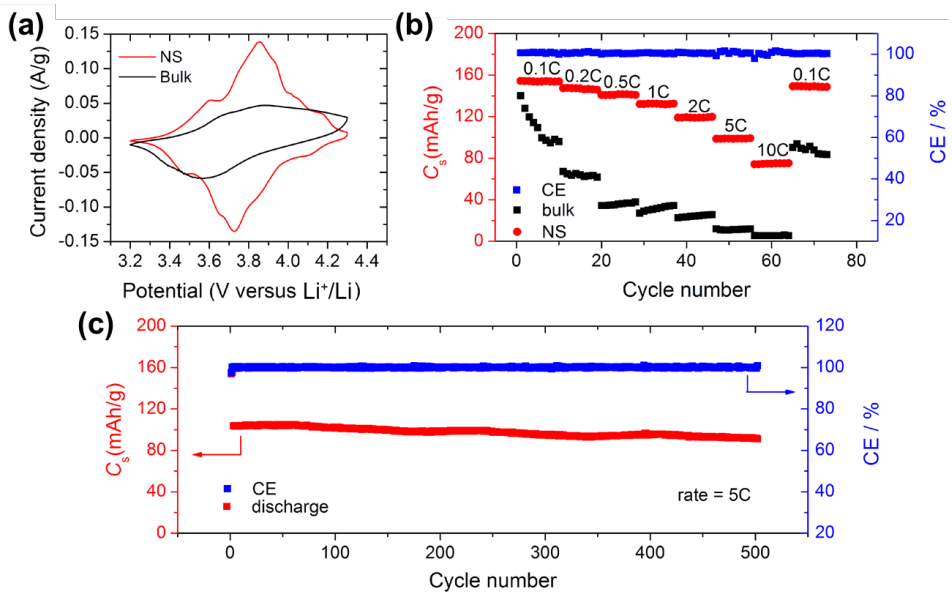

Figure 4.4 Electrochemical performance of the $VOPO_4$ nanosheets electrode in lithium cells. (a) Cyclic voltammetric profiles of $VOPO_4$ nanosheets (NS, red) and $VOPO_4 \cdot 2H_2O$ microcrystals (bulk, black) at a fixed scan rate of 0.1 mV/s. (b) Rate capabilities at the C rate ranging from 0.1~10C. (c) Specific capacity (*C*s) retention at 5C rate and corresponding Coulombic efficiency (CE).

To search for the possible reasons for the improved rate capability and cycling stability of the nanosheets electrode, systematic CV measurements were carried out in lithium cells. The CV curves at various scan rates from 0.02 to 2 mV/s display similar shapes and a gradual broadening of the peaks can be observed (Figure 4.5a). For an electrochemical energy storage device, several processes could contribution to the total stored charge and they can be characterized by analyzing the CV data at various sweep rates according to $i = av^b$, where the measured current i obeys a power law relationship with the sweep rate υ and a and b are adjustable parameters. In particular, the b-value of 0.5 indicates a total diffusion-controlled process, whereas 1.0 represents a capacitive process.[137] By plotting log i vs log υ, b-values of 0.86 and 0.92 as the slopes are determined for cathodic and anodic peaks (Figure 4.5b), indicating that the majority of the current at the peak potential is capacitive.

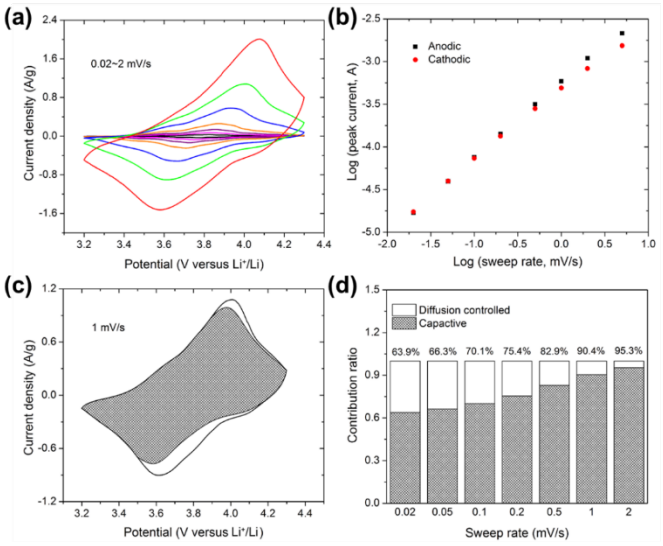

Figure 4.5 (a) CV curves at various scan rates, from 0.02 to 2 mV/s. (b) Determination of the b-values using the relationship between peak current and scan rate. (c) Separation of the capacitive and diffusion currents at a scan rate of 1 mV/s. (d) Contribution ratio of the capacitive and diffusion-controlled processes at various scan rates.

The total capacitive contribution at a certain scan rate could be quantified by separating the specific contribution from the capacitive and diffusion-controlled processes at a particular voltage according to[137]

$$i(\mathrm{V}) = k_1 v + k_2 v^{1/2}$$

where k_1 and k_2 are constants for a given potential. By plotting $i(\mathrm{V})/v^{1/2}$ vs. $v^{1/2}$, k_1 is determined as the slope, therefore capacitive and diffusion currents can be obtained. For example, at scan rate 1 mV/s (Figure 4.5c), ~90% of the total current, namely the capacity, is capacitive in nature. In the cathodic sweep, the diffusion-controlled process appears during the initial Li^+ intercalation and mostly at the peak voltage of 3.6 V. In the anodic sweep, nearly all of the diffusion-controlled contributions occur at around the peak voltage. Both demonstrate that the diffusion process is only significant at regions corresponding to the redox reaction between V^{5+}/V^{4+}.[138] Similarly, contribution ratios between the two different processes at other scan rates are calculated likewise (Figure 4.5d). The quantitative analysis shows that the capacitive contribution gradually improves with increasing the scan rate. It is interesting to note at very low scan rate, for example 0.02 mV/s, capacitive contribution is already significant (~64%). On the other hand, it is very likely that capacitive contribution in microcrystals electrode would be minimum, as indicated by the low specific capacity at relatively high C rate. For $VOPO_4$ nanosheets, both the calculated *b*-value and capacitive contribution clearly demonstrate the unique characteristic behavior as a result of intercalation pseudocapacitance, which is quite different from charge storage mechanism in classical electrode materials, for example $LiFePO_4$.[139] Combined with the prior structural characterization, it can be concluded that charge storage in $VOPO_4$ nanosheets mainly follows intercalation pseudocapacitive mechanism.

SIBs represent potential alternatives to LIBs for large-scale energy storage due to their low cost and resource abundance.[140] Inspired by the superior rate performance and cycling stability in lithium cells, the same CV measurements and kinetic analysis were performed in sodium cells (Figure 4.6). Comparing the kinetics in lithium and sodium cells, several differences can be spotted. Firstly, the calculated *b*-values for cathodic and anodic peaks in sodium cells are 0.68 and 0.71, smaller than those in lithium cells, but still larger than 0.5. This indicates a mixture of diffusion-controlled and capacitive processes. Secondly, for sodium cells, the capacitive contribution at low scan rate (0.02 mV/s) is significantly smaller than that in lithium cells at the same scan rate. Thirdly, polarization between the charge/discharge curves is rather high, even at low scan rate (340 mV at 0.02 mV/s). All above observations conclude a relatively inferior kinetics in the sodium cells and this can be understood as the transport of Na-ion suffers from a higher diffusion barrier, which is commonly observed for the sodium version of many Li-ion intercalation materials[141-143] and supported by theoretical calculations.[144, 145] Despite such an obvious disadvantage, the calculated *b*-values in our $VOPO_4$ nanosheets still signify reasonable rate performance resulted from large capacitive contributions as shown at high scan rates.

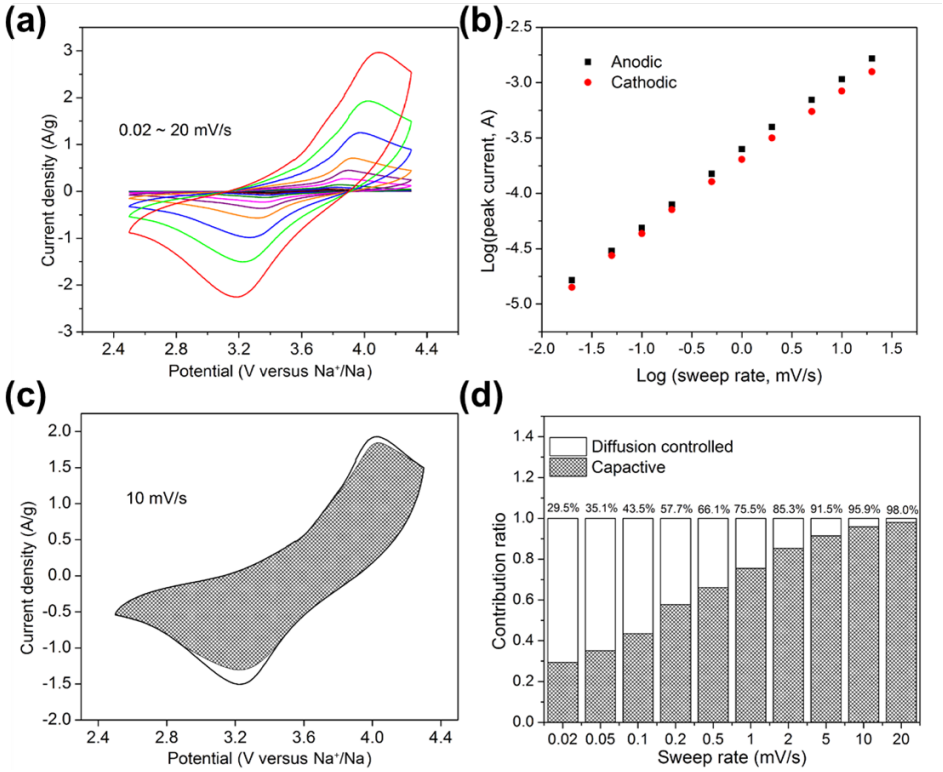

Figure 4.6 Kinetic analysis of the electrochemical properties of $VOPO_4$ nanosheets electrode in sodium cells. (a) CV curves at various scan rates, from 0.02 to 20 mV/s. (b) Determination of the *b*-values using the relationship between peak current and scan rate. (c) Separation of the capacitive and diffusion currents at a scan rate of 10 mV/s. (d) Contribution ratio of the capacitive and diffusion-controlled processes at various scan rates.

Though $VOPO_4$ system has been previously exploited as cathode materials for LIBs, there has been no report on its application in SIBs. As shown in the charge/discharge profiles (Figure 4.7a), $VOPO_4$ nanosheets electrode is able to deliver capacities of 136, 127, 114, 101, 87, 70 and 48 mAh/g at C rate of 0.1, 0.2, 0.5, 1, 2, 5 and 10, respectively (Figure 4.7b). All the values are less than those in lithium cells at the same C rate, as expected from the kinetic analysis. However, the capacities are still

superior than those of the cell made from microcrystals, especially at high C rates (Figure 4.7d). For example, after 5C rate, the latter shows almost zero capacity and cannot recover any capacity when C rate changes back to 0.1C after 10C rate. A slight capacity drop occurs in the rate performance test when the C rate changes back to 0.1C (Figure 4.7b), which is not observed in the case of lithium cell. This electrochemical instability is more noticeable in the cycling test, in which the initial capacity of nanosheets reaches approximately 73 mAh/g at a current rate of 5C and the capacity retention is 73% after 500 cycles (Figure 4.7c).

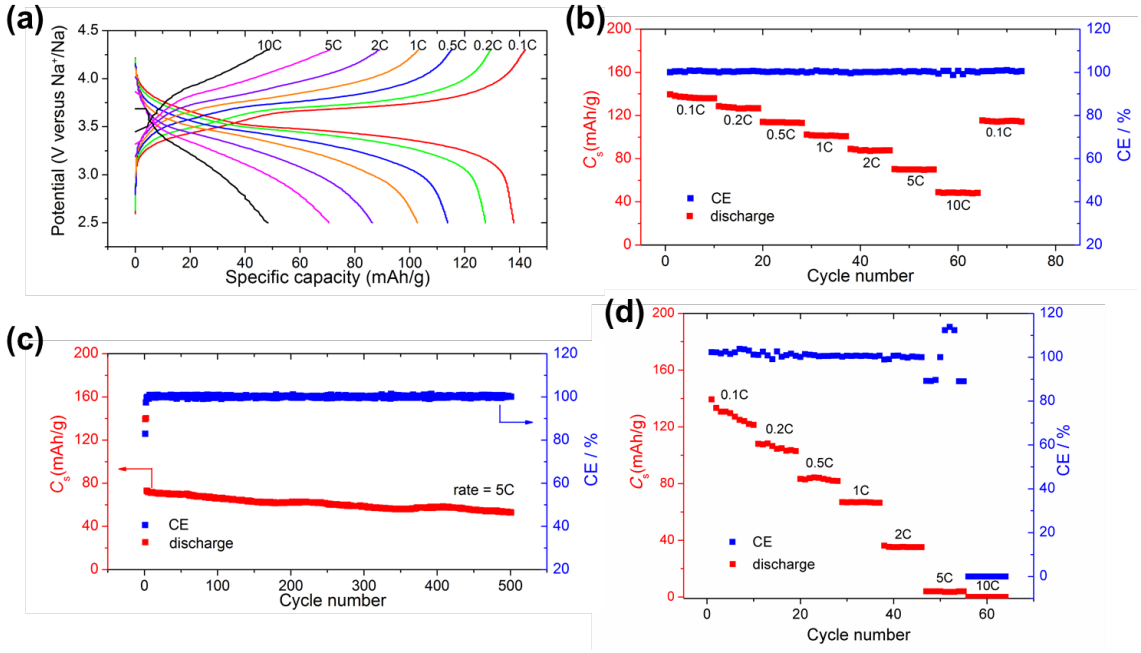

Figure 4.7 Electrochemical performance of the $VOPO_4$ nanosheets electrode in sodium cells. a) Charge/discharge profiles at various current rates from 0.1C to 10C. b) Rate capability at the C rate ranging from 0.1~10C. c) Specific capacity (*C*s) retention at 5C rate and corresponding Coulombic efficiency (CE). (d) Rate capability of sodium cells made from microcrystals electrode at the C rate ranging for comparison purposes. After 10C, the cell cannot go back to 0.1C.

To understand the possible reasons for the more pronounced capacity decay in sodium cells, microscopic morphology of the nanosheets was examined before and after long-term cycle. In both lithium and sodium cells, the nanosheets morphology remain intact, similar to that of the electrode before cycling test (Figure 4.8a). After cycles, it is found the surface of nanosheets remains clean and smooth in the lithium cell (Figure 4.8b), while the surface become rough in the sodium cell (Figure 4.8c). Therefore, the rough surface in the sodium cell may be a sign of the capacity decay and further investigation will be required to understand its physicochemical nature and electrochemical origination.

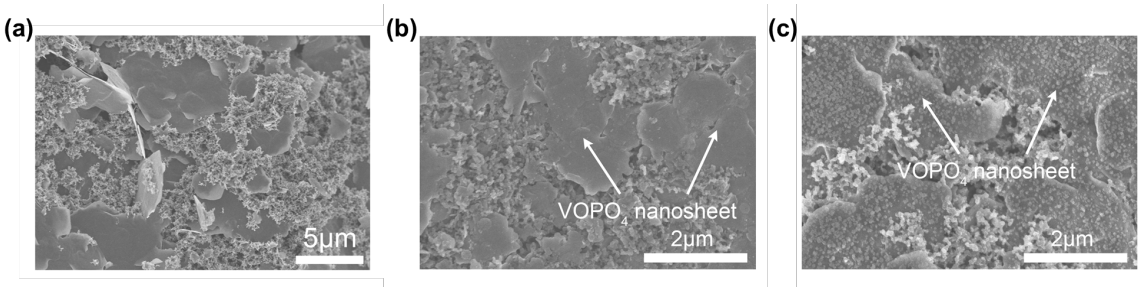

Figure 4.8 Top-view SEM images of $VOPO_4$ nanosheets electrode (a) before cycling test, (b) after 500 cycles at 5C rate in lithium storage device and (c) after 500 cycles at 5C rate in sodium storage device. Notice the nanosheet morphology remained intact during the electrode preparation and electrochemical cycling.

In summary, ultrathin $VOPO_4$ nanosheets with large surface-area-to-volume ratio have been successfully obtained via exfoliation of bulk $VOPO_4 \cdot 2H_2O$ microcrystals. The exfoliated $VOPO_4$ nanosheets deliver a high reversible capacity of 154 mAh/g at 0.1C and 74 mAh/g at 10C in lithium storage device, and it also exhibits a stable cycling life of 90% capacity retention after 500 cycles at 5C rate. Kinetic analysis confirms the Li-ion intercalation pseudocapacitive behavior in the $VOPO_4$ nanosheets and also reveals a high

contribution of capacitive contribution. Moreover, $VOPO_4$ nanosheets for the first time, display a reversible capacity of 136 mAh/g at 0.1 C and 70 mAh/g at 5C in sodium storage device, but slightly inferior cycling stability as demonstrated with 73% capacity retention after 500 cycles at 5C rate. Similar analysis reveals a Na-ion intercalation pseudocapacitive behavior in the sodium cell but with less efficient kinetics and less contribution from the capacitive process. Combining above conclusions we show that ultrathin $VOPO_4$ nanosheets is a great material platform to study fundamental charge storage mechanism. Our study also provides a direction in developing electrode materials featuring high-rate alkali-ion storage capability for EES devices and we anticipate that the demonstrated intercalation pseudocapacitive mechanism will find more applications in new material systems or old materials with proper structural engineering, such as solution-phase exfoliation strategy used in this study.

4.3 CHARGE STORAGE IN NANOSHEETS OF $NbOPO_4$ HYDRATES

In this part, Li- and Na-ion storage in nanosheets of $NbOPO_4$ hydrates, including $NbOPO_4 \cdot 2.5H_2O$ and $Nb_2(OH)_2(HPO_4)(PO_4)_2 \cdot 1.7H_2O$, were comparatively studied with exfoliated $VOPO_4 \cdot 2H_2O$ nanosheets. $NbOPO_4$ has a much larger molecular weight than $VOPO_4$, making it less appealing to be used as electrode materials for practical applications. However, it is fundamentally interesting to explore its charge storage capabilities given the slight structure difference in simple hydrate compared with $VOPO_4$ and the existence of a layer-condensed structure.

For studying charge storage in organic electrolytes, the nanosheet-based electrodes (for both $NbOPO_4$ hydrates and $VOPO_4 \cdot 2H_2O$) were prepared by re-dispersing nanosheets powder in a small amount of 2-propanol, adding Super P conductive carbon

black (15 wt% in the final electrode), and mixing in a Thinky centrifugal mixer. The obtained homogenous slurry was then drop-casted on aluminum foil and dried in the open air for at least 12 hrs. After drying, the typical mass loading of the electrodes was about 1.5 ~ 2.0 mg cm^{-2}. Charge storage of $VOPO_4 \cdot 2H_2O$ was also studied in aqueous electrolytes, and the electrodes were prepared by drop-casting the 2-propanol dispersion of nanosheets (without Super P) onto carbon paper.

The electrochemical measurements for $VOPO_4 \cdot 2H_2O$ were carried out in a three-electrode system using 1 M LiCl/NaCl as aqueous electrolytes and 1 M $LiClO_4$/$NaClO_4$ in 1:1 (v/v) ethylene carbonate and diethyl carbonate as organic electrolytes. Ag/AgCl (3 M KCl) and Ag/Ag^+ (0.01 M $AgNO_3$ in 0.1 M tetraethylammonium tetrafluoroborate in acetonitrile) were used as the reference electrodes, respectively. Platinum foil was used as the counter electrode in both cases. For the electrodes based on $NbOPO_4$ hydrates, CR2032 coin cells were assembled inside an Ar-filled glove box using metallic Li/Na as anodes and the same $LiClO_4$/$NaClO_4$ solutions as electrolytes. Celgard 2500 and Waltman glassy fiber were used as the separators for lithium and sodium cells, respectively. CV and galvanostatic charge–discharge measurements were conducted on a Bio-Logic potentiostat (VMP3) and a Neware battery tester (BTS 4000), respectively.

The electrochemical intercalation of alkali-ions in $MOPO_4$ involves electron transfer (provided by potentiostat) to the material and intercalation of ions into the its interlayer space. For hydrates, the interlayer H_2O molecules may stay inside the material with certain rearrangement or leave the material during the intercalation due to space limit. The latter may be irreversible and results in a structure charge of the host. When both charge storage and structure alteration are reversible, the general charge storage mechanism for both $NbOPO_4$ and $VOPO_4$ follows the reaction equation below:

$$MOPO_4 \cdot nH_2O + xLi^+/Na^+ + xe^- \leftrightarrow Li/Na_xMOPO_4 \cdot (n-m)H_2O + mH_2O$$

Thanks to the thin thickness of the nanosheets used in this study, the redox reactions accompanying the charge storage processes can be conveniently probed by ex situ XPS, which were performed on as-prepared nanosheet-based electrodes, and those after their first discharge (Li-ion intercalation) and first charge (Li-ion deintercalation). Samples that have undergone electrochemical measurements were sealed in an Ar-chamber before transferring for XPS characterization. For $VOPO_4 \cdot 2H_2O$ nanosheets (Figure 4.9a), the exfoliation reduces a tiny portion of the vanadium atoms to V^{4+} possibly due to the reducing ability of 2-propanol. The V XPS spectra indicates the electrochemical intercalation of Li-ion results in the reduction of V^{5+} to V^{4+}, and the deintercalation process reverses the oxidation state back to V^{5+}. Re-dispersing $NbOPO_4 \cdot 2.5H_2O$ nanosheets in 2-propanol does not induce any change in the oxidation state of niobium atoms. Other than that, similar reversible change from Nb^{5+} to Nb^{4+} and back to Nb^{5+} is clearly seen from the Nb XPS spectra (Figure 4.9b).

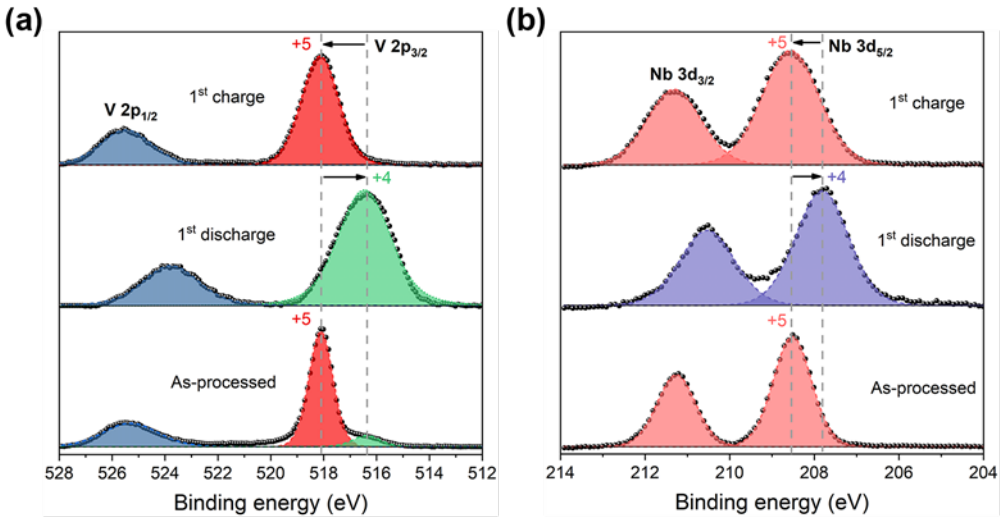

Figure 4.9 V and Nb XPS spectra of as-prepared nanosheet-based electrode, after its first discharge and after its first charge in lithium cells for (a) $VOPO_4 \cdot 2H_2O$ and (b) $NbOPO_4 \cdot 2.5H_2O$.

The most straightforward yet viable way to study this intercalation system is to examine the change of interlayer distance (manifested by the position of (001) peak) during or after charge/discharge processes by XRD. In this study, all XRD patterns were ex situ collected as in XPS. All electrodes, except for those $VOPO_4 \cdot 2H_2O$ electrodes charged/discharged in aqueous electrolytes, were sealed in an Ar-filled holder for XRD measurements. For comparison purposes, all potential values are normalized with respect to standard hydrogen electrode (SHE).

For $VOPO_4 \cdot 2H_2O$ nanosheet-based electrodes, the electrochemical intercalation of Li- and Na-ion have already been shown to be reversible in organic electrolytes in section 4.2. In this study reversibility seems to even higher possibly due to the change of electrolyte compositions. In lithium cells, the CV curves show a minor stabilization process where the smaller redox peak gradually disappears during cycling (Figure 4.10a). In sodium cells, however, the CV curves remain nearly unchanged (Figure 4.10b), indicating the high electrochemical reversibility in this case.

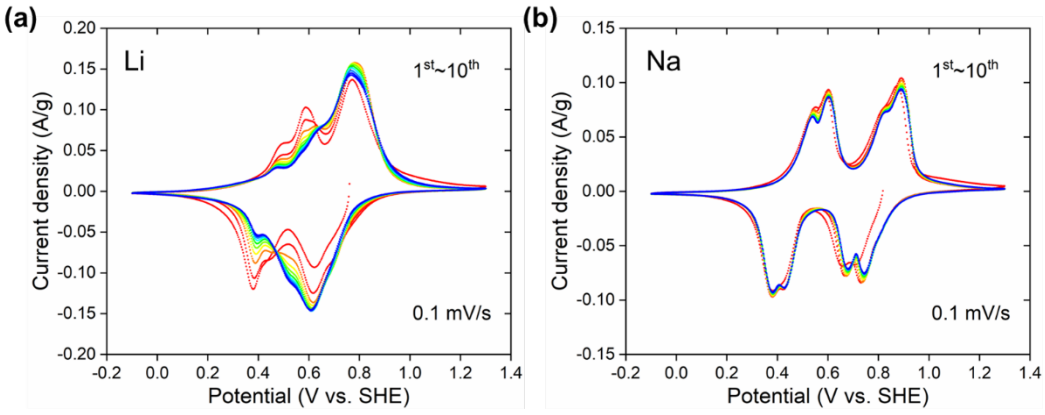

Figure 4.10 CV curves of $VOPO_4 \cdot 2H_2O$ electrodes scanned at 0.1 mV/s in (a) lithium cells and (b) sodium cells. Color of the curve changes from red to blue as cycle number increases.

The structural evolutions of $VOPO_4 \cdot 2H_2O$ during reversible Li- and Na-ion intercalation probed by XRD show very different patterns for the two ions (Figure 4.11). In both cases, interlayer distance decreases as first cycle ion intercalation proceeds. One peak is consistently observed during Li-ion intercalation but two peaks are spotted at a certain potential range during Na-intercalation, and at the end of discharge, a smaller interlayer distance is seen for Na-intercalated structure. Once charge starts, the interlayer distance recovers for both ions, but to different extents. The recovery is nearly complete for in the case of Li-deintercalation but halfway and even reverses back at the end of charge for Na-deintercalation. From second cycle onwards, the processes are completely reversible for both cases. The highly reversible process in the lithium cell indicates there is no water loss during Li-ion insertion/deinsertion into $VOPO_4 \cdot 2H_2O$, while the decreased interlayer distance upon Na-ion deinsertion implies loss of interlayer water. According to previous studies using chemical intercalation methods, the intercalation products are likely to be $LiVOPO_4 \cdot 2H_2O$ and $NaVOPO_4 \cdot H_2O$ in current electrochemical intercalation in organic electrolytes.[74, 75]

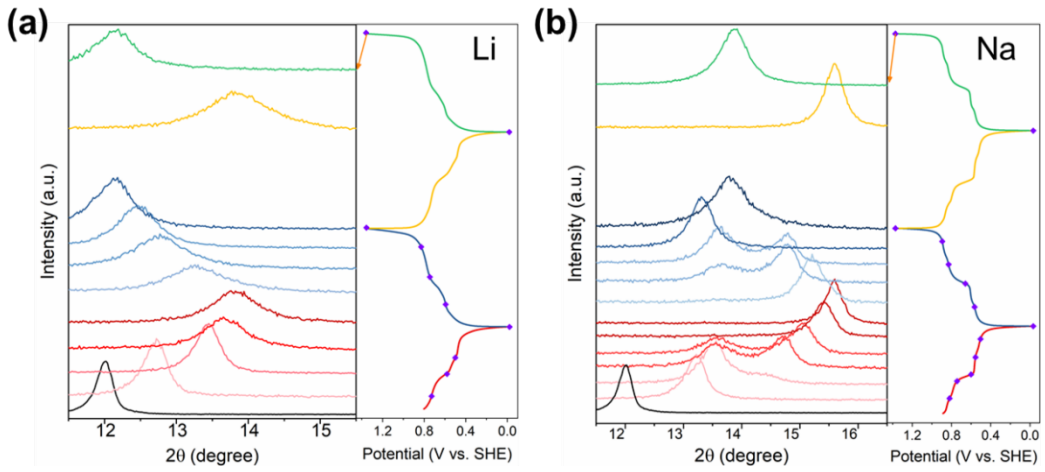

Figure 4.11 Ex situ XRD patterns of $VOPO_4 \cdot 2H_2O$ electrodes during charge/discharge in (a) lithium cells and (b) sodium cells using organic electrolytes.

Based on above results, it is interesting to see that the electrochemical reversibility is not necessarily in accordance with the structural reversibility. In particular, the high electrochemical reversibility in the sodium cell is kind of contrary to the observation made in section 4.2. While this high electrochemical reversibility may be complicated to explain, it is quite clear that why the Na-intercalated structure is not able to be converted back to the original dihydrate. As formation of the fully intercalated structure $NaVOPO_4 \cdot H_2O$ drives half of the H_2O molecules (most likely the non-coordinated ones) from the host to the electrolyte, the reverse process is thermodynamically impossible as the lost H_2O molecules are dispersed in the electrolyte solution. However, if the electrolyte contains water, or it is simply an aqueous electrolyte, the structural reversibility should be achievable as H_2O supply to restore the dihydrate phase is possible through the electrolyte. This is exactly the case that is found from electrochemical intercalation using aqueous electrolytes, in which both lithium and sodium cells exhibit reversible structural evolutions during charge/discharge (Figure 4.12).

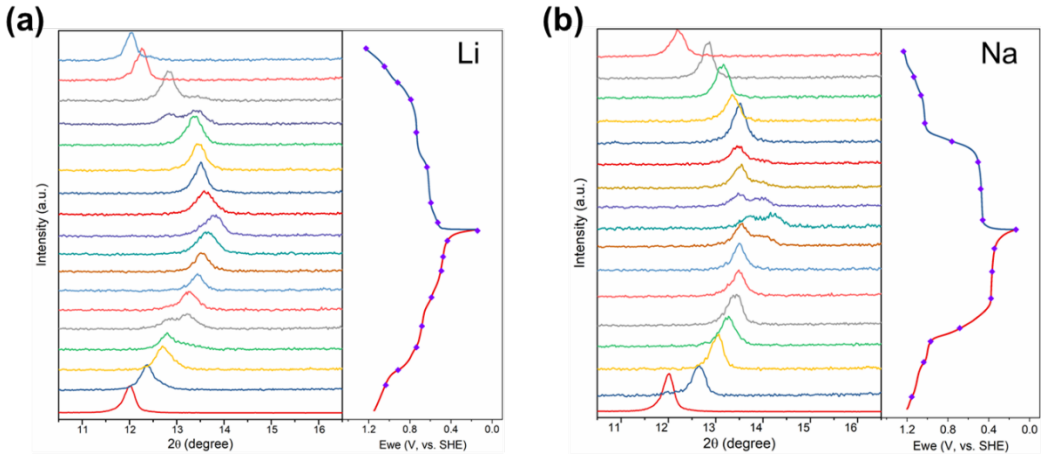

Figure 4.12 Ex situ XRD patterns of $VOPO_4 \cdot 2H_2O$ electrodes during charge/discharge in (a) lithium cells and (b) sodium cells using aqueous electrolytes.

Electrochemical intercalation in $NbOPO_4 \cdot 2.5H_2O$ was conducted in a completely different potential range because Nb^{5+} has a much lower reduction potential than V^{5+}. This also excludes the possibility of conducting the electrochemical intercalation in aqueous electrolyte. In contrast to $VOPO_4 \cdot 2H_2O$, the electrochemical intercalation of Li- and Na-ion into $NbOPO_4 \cdot 2.5H_2O$ turn out unstable in organic electrolytes (Figure 4.13). For both ions, CV curves shrink as cycle number increases. In lithium cells the cathodic peak in the CV curves gradually shifts to higher potentials while in sodium cells the peak shifts to lower potentials.

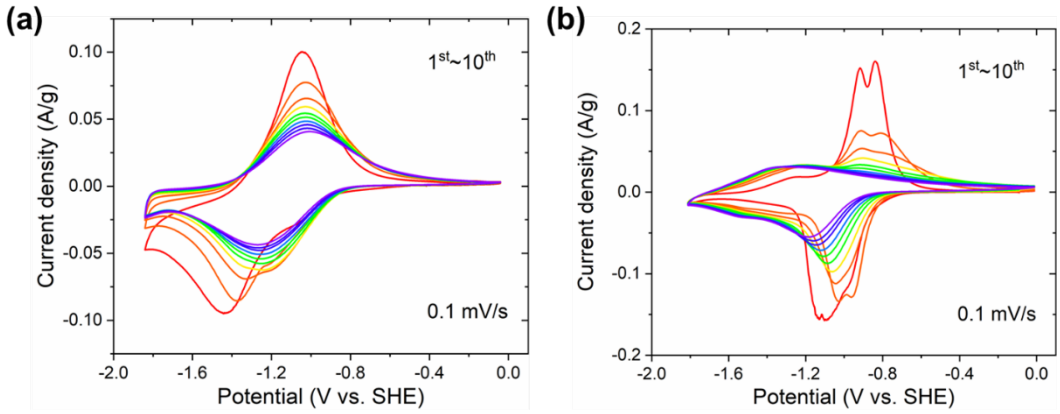

Figure 4.13 CV curves of $NbOPO_4 \cdot 2.5H_2O$ electrodes scanned at 0.1 mV/s in (a) lithium cells and (b) sodium cells. Color of the curve changes from red to blue as cycle number increases.

To understand possible degradation mechanism for the electrochemical performance in $NbOPO_4 \cdot 2.5H_2O$, similar ex situ XRD measurements used in $VOPO_4 \cdot 2H_2O$ were carried out to probe its structural evolutions during the first few charge/discharge cycles. For both Li- and Na-ion intercalation, interlayer distance decreases at the end of first discharge, but the decrease is more pronounced in the Li-ion

case. Judging by the peak positions after charge in first and subsequent cycles, it is clear that the interlayer distance of deintercalated nanosheets decreases gradually in both cases, and the extent is more severe for Li-ion. In the third cycle, the peak positions are almost identical after discharge and charge in the lithium cell, indicating the formation of a stable interlayer structure regardless of Li-ion intercalation. In contrast, Na-ion intercalation seems to induce an obvious phase transformation during the second and the fourth cycle, leading to an intercalated structure with much smaller interlayer distance. The observed structural evolutions are consistent with the electrochemical measurements in terms of the degree of change per cycle. The intercalation process for Li-ion is more benign while the redox processes and the corresponding structure changes for Na-ion are more violent. Compared with $VOPO_4 \cdot 2H_2O$, charge storage in $NbOPO_4 \cdot 2.5H_2O$ is less stable and capacity decay is expected in the cycles of galvanostatic charge and discharge.

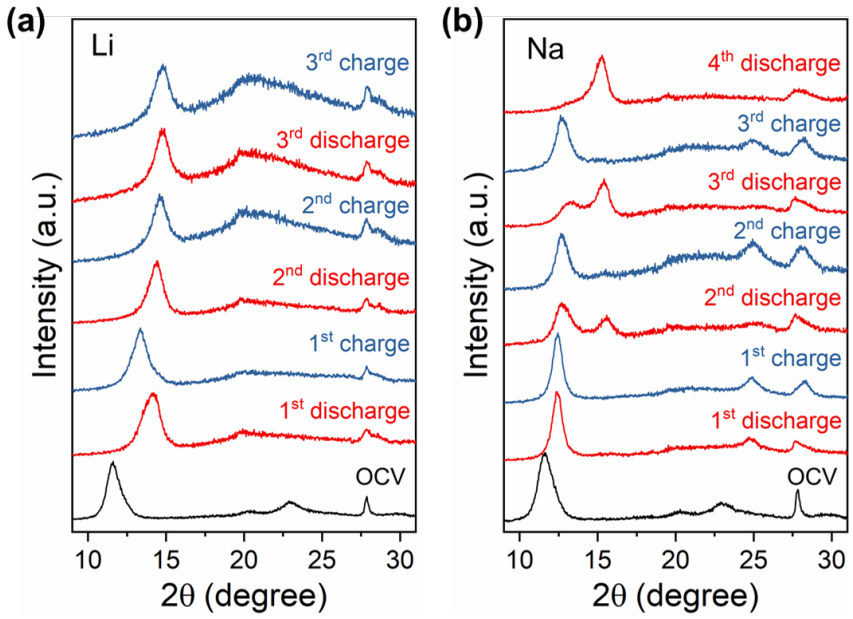

Figure 4.14 Ex situ XRD patterns of $NbOPO_4 \cdot 2.5H_2O$ electrodes during charge/discharge in (a) lithium cells and (b) sodium cells using organic electrolytes.

Several reasons could be responsible for the electrochemical/structural instability in $NbOPO_4 \cdot 2.5H_2O$, and interlayer water is likely to be the culprit in this case. On the one hand, In $NbOPO_4 \cdot 2.5H_2O$, both coordinated and non-coordinated H_2O molecules are less stable than those in $VOPO_4 \cdot 2H_2O$ as discussed in Chapter 2. The intercalation and deintercalation of alkali-ions may easily drive them out of from the host structure. On the other hand, the low reduction potential of Nb^{5+} that outside the stable electrochemical potential window of H_2O is able to cause hydrogen evolution reaction, leading to further water loss in the structure. In this regard, $Nb_2(OH)_2(HPO_4)(PO_4)_2 \cdot 1.7H_2O$ (denoted as P-$NbOPO_4$) with condensed layers by replacing coordinated H_2O molecules with PO_4 groups is a ideal structure without instability issue in H_2O. Although there is no coordinated water, P-$NbOPO_4$ still contains non-coordinated or free water inside the structure as shown by TGA. While loss of water in $NbOPO_4 \cdot 2.5H_2O$ leads to collapse of interlayer structure and detrimental effects in electrochemical performance, P-$NbOPO_4$ does not suffer from this disadvantage. As shown in Figure 4.15a, its dehydration product largely retains the original structure even when heated at elevated temperature (200 °C). The structural evolution of P-$NbOPO_4$ nanosheet-based electrodes in lithium cells probed by ex situ XRD shows emergence of the dehydrated phase after the first discharge and no further phase change in subsequent charge/discharge cycles (Figure 4.15b). The formation of the same dehydrated phase as in vacuum and heating dehydration indicates H_2O has been removed from the structure during the electrochemical measurements. The nearly unchanged XRD patterns since the first discharge manifest the high structural stability in P-$NbOPO_4$, as expected from the rigid interlayer structure benefiting from pillaring effect brought by the intercalated PO_4 groups.

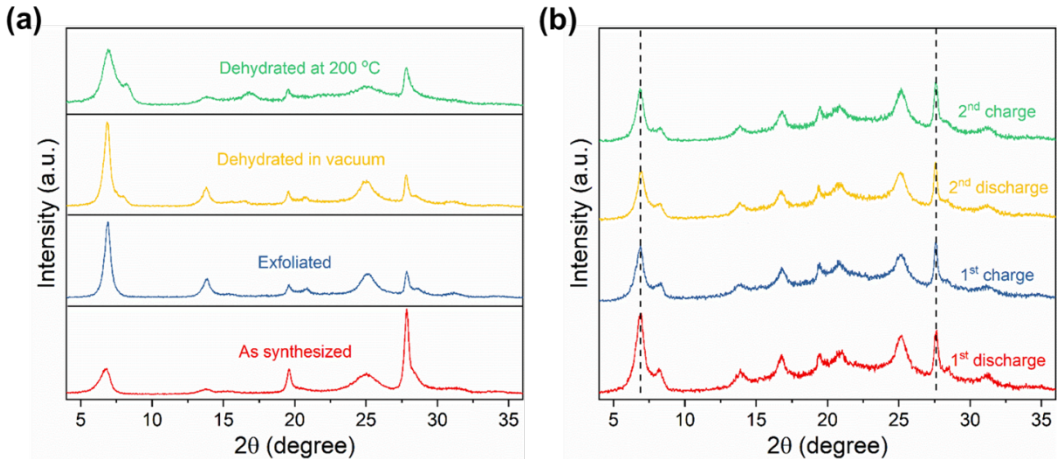

Figure 4.15 (a) XRD patterns of as-synthesized $Nb_2(OH)_2(HPO_4)(PO_4)_2 \cdot 1.7H_2O$ (P-$NbOPO_4$), its nanosheet-based electrode, dehydration products in vacuum and at 200 °C. (b) Ex situ XRD patterns of P-$NbOPO_4$ electrodes during charge/discharge in lithium cells.

Besides the structural stabilization effect, the interlayer PO_4 groups do not seem to complicate the electrochemical behavior of the main $NbOPO_4$ frame. The CV curves of P-$NbOPO_4$ are similar to those of $NbOPO_4 \cdot 2.5H_2O$, except that some redox peaks shown in the first cycle disappear in the second cycle (Figure 4.16a), and these peaks are absent in $NbOPO_4 \cdot 2.5H_2O$. A direct consequence of layer condensation by PO_4 group is the formation of Nb-OH bonds, which can be seen from the structure of P-$NbOPO_4$ in Chapter 2 and its chemical formula. The hydroxide groups are electrochemical active and are likely to be reduced during the first cathodic sweep. The nature of the product in this process is unknown, but the conversion is apparently not reversible as these peaks are no longer observed in the subsequent anodic sweep and cycles. Other than that, the electrochemical stability of P-$NbOPO_4$ is clearly seen in the galvanostatic charge–discharge cycling tests when compared with $NbOPO_4 \cdot 2.5H_2O$ (Figure 4.16b).

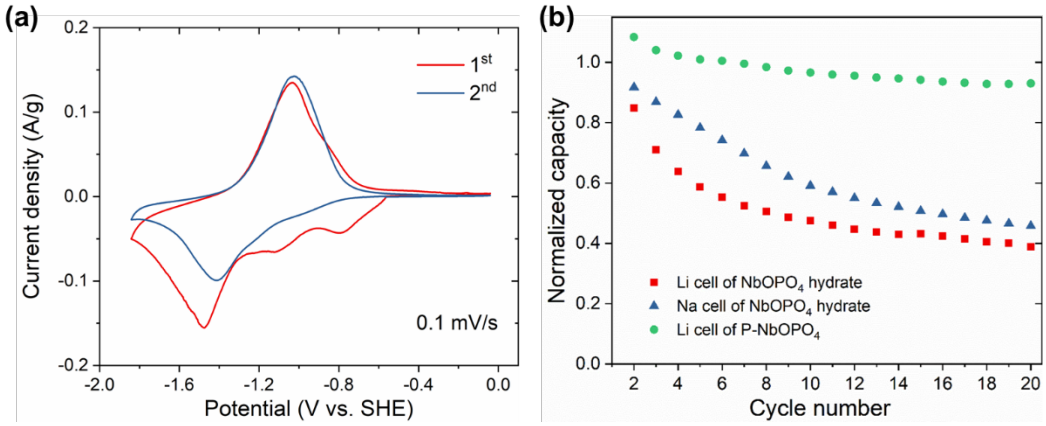

Figure 4.16 (a) CV curves of P-$NbOPO_4$ electrodes scanned at 0.1 mV/s in the lithium cell. (b) Cycling stabilities of P-$NbOPO_4$ and $NbOPO_4 \cdot 2.5H_2O$. Capacities are normalized with respect the active frame of $NbOPO_4$.

In sodium cells, the intercalation process does not proceed as smooth as in the lithium cell. The redox peak in the first cathodic sweep appears at a much lower potential in the sodium cell, and the corresponding anodic peak does not show up in the reverse sweep (Figure 4.17a). In the second cycle, the CV curve shrinks significantly, indicating much less extent of Na-ion intercalation versus the first cycle. Ex situ XRD patterns of the P-$NbOPO_4$ electrodes at several selected potentials in the first cycle reveal that, except for the dehydration induced phase change, there is no obvious structure alteration during the Na-ion intercalation and deintercalation. However, the crystallinity of P-$NbOPO_4$ becomes poor compared to the case in the lithium cell (Figure 4.17b). It should be noted that, the structure degradation is not caused by extending the scan potential to a lower value, which is need to reveal the redox peak. The pattern collected at -1.5 V (blue) shows that the degradation happens even before the major redox peak appears. Therefore, P-$NbOPO_4$ turns out not a good Na-ion storage host that suffers from irreversible charge storage processes and low structure stability.

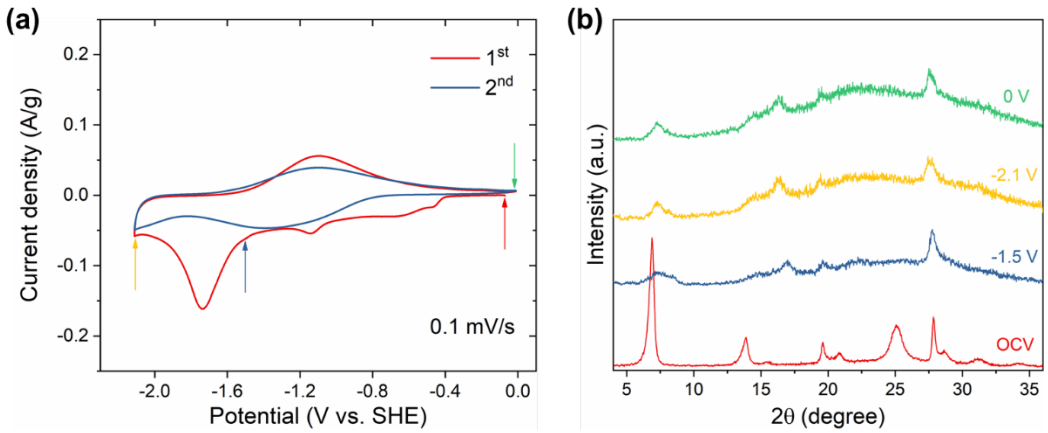

Figure 4.17 (a) CV curves of P-$NbOPO_4$ electrodes scanned at 0.1 mV/s in the sodium cell. (b) Selective ex situ XRD patterns of P-$NbOPO_4$ electrodes in the first charge/discharge cycle.

Much more characterization and theoretical modeling are needed to fully understand charge storage mechanism and kinetics in the nanosheets of $NbOPO_4$ hydrates. While the simple hydrate $NbOPO_4 \cdot 2.5H_2O$ behaviors similar to $VOPO_4 \cdot 2H_2O$, it shows inferior electrochemical performance, in particular cycling instability, due to lack of stable intercalated structures with loss of interlayer water. The derived hydrate P-$NbOPO_4$ with pillared structure exhibits much improved structure and electrochemical stabilities in lithium cells. However, its performance becomes poor in sodium cells, possibly due to the larger size of Na-ion which requires a large interlayer space, or perhaps more importantly, an unobstructed interlayer pathway for ion transport. The interlayer existing PO_4 groups are able to stabilize the layers but without too much expansion, or may be simply too bulky to block the diffusion of Na-ion. Nevertheless, the idea of forming pillared interlayer structure is of high scientific and technological importance to the development of advanced electrode materials for enhanced electrochemical properties.

4.4 INTERLAYER-EXPANDED $VOPO_4$ NANOSHEETS FOR ENHANCED NA-ION STORAGE

2D materials that are insertion-based battery electrodes may benefit most from expanded interlayer space, as the ion accessibility, storage capability, and transport kinetics are critically determined by the interlayer distance.[146] The beneficial effect due to expanded interlayer space is expected to be more pronounced in the case of larger charge-carrying ions. A straightforward method to achieve interlayer space expansion is by intercalation of a pillaring agent into the interlayer, whose spacing can be controlled according to the size of the intercalated agent.[147] However, the application of this strategy needs to be rationalized with clear understanding of the corresponding intercalation chemistry of the original layered materials.

The ferrocene intercalated $VOPO_4$ can be considered as an extention of conventional $VOPO_4$ material with unique structral modifications. The nearly one third increase of interlayer distance (from 7.41 Å to 9.79 Å) is able to facilite more facile mass transport inside this layered structure. More interestingly, electorchemical properties of ferrocene, which itself alone is known to be active, as intercalant in the strucutre remains unknown. These may be quite relevant features in various energy-related applications.[14] Inspired by above ideas, we proceed to briefly examine the electrochemical properties of this organic-inogranic superlattice with different α values (Figure 4.18a). When tested in lithium cells, CV curves (Figure 4.18b) of selected intercalation products reveal several intriguing observations. First, a reduced peak separation of vanadium redox reaction can be seen in intercalated $VOPO_4$ when compared with non-intercalated one. This is likely due to a decreased polarization as a result of increased interlayer distance. Second, as extent of intercalation (or the value of α) increases, a new pair of redox peaks emerge while redox peaks of $VOPO_4$ diminish significantly. We attribute the new redox peaks to oxidation and reduction of interlayer residing ferrocene, which is unexpectedly

electrochemical active in such confined structure. The deactivation of $VOPO_4$ can be understood for following reasons. In ferrocene intercalated $VOPO_4$, due to the redox intercalation mechanism, ferrocene molecule exists in the form of ferrocenium ion, which is positively charged and repels further intake of alkali-ion. On the other hand, the highly ordered superlattice structure, may not favor the access of charge carrier to the vanadium centers. Nevertheless, above observations manifest a type of material with dual centers of electrochemical activity, which can be varied in an inversely correlated but controllable manner.

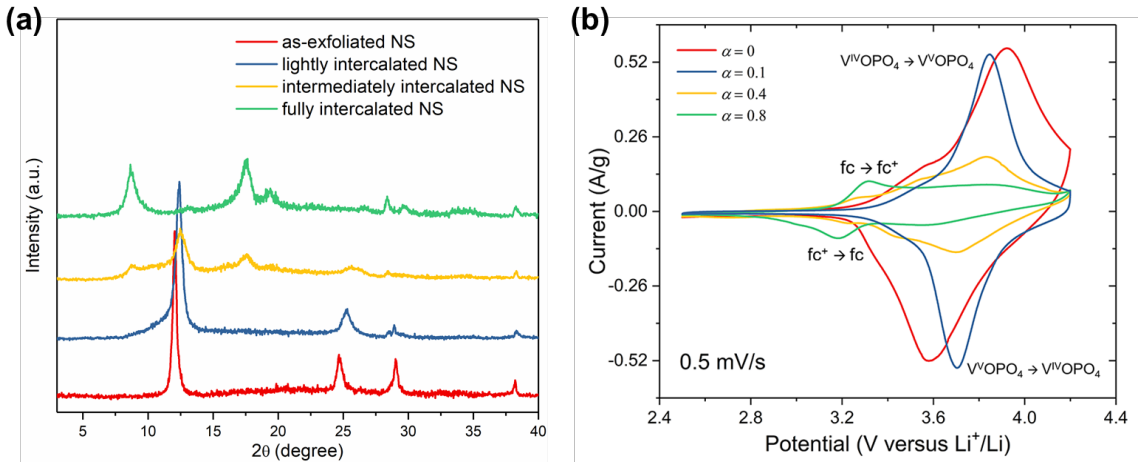

Figure 4.18 (a) XRD patterns of nanosheets (NS) loaded electrodes with different extents of intercalation. (b) CV curves of selected intercalation products with various α values.

The setback in ferrocene intercalated $VOPO_4$ indicates expanding interlayer distance must be realized without sacrificing charge storage capabilty. Next we develop an effective interlayer engineering strategy to improve the Na-ion transport in $VOPO_4$ nanosheets via controlled organic intercalation. As a proof-of-concept, triethylene glycol (TEG) and tetrahydrofuran (THF) are chosen as the intercalants to demonstrate the feasibility of this interlayer engineering strategy and its advantageous features for

improving Na-ion transport and storage. The concept for the developed general synthesis of 2D TEG and THF intercalated $VOPO_4$ nanosheets is illustrated in Figure 4.19. The intercalation compounds were obtained by a facile displacement reaction, and the intercalation process is suitable for large-scale production. In brief, $VOPO_4{\cdot}2H_2O$ bulk microcrystals were first employed as the starting material for the intercalation (Figure 4.19a), and mixed with 2-propanol and the organic intercalants, i.e. TEG or THF solvents (Figure 4.19b). In a typical intercalation process, 100 mg $VOPO_4{\cdot}2H_2O$ was dispersed in 7 mL 2-propanol solvent, and then 8 mL organic intercalants, like TEG and THF, were added into the $VOPO_4$ dispersion. After magnetic stirring under 110 °C for 2 days, a blue-greenish and a dark green product were obtained for TEG and THF, respectively. The as-obtained powders were further washed with 2-propanol for three times, and dried in vacuum at 80 °C for overnight. The as-obtained $VOPO_4$ samples in the form of nanosheets with intercalated organic molecules exhibited different and controllable interlayer distances, due to the different chemical structures of the TEG and THF molecules. TEG and THF can uniformly replace the water molecules in the bulk microcrystals and intercalate in the layers through the hydrogen bonds formed between the intercalants and $VOPO_4$ layers (Figure 4.19c). The intercalated molecules can be stabilized by these hydrogen bonds, as observed the similar case of intercalants in graphic intercalation compounds.[148, 149] We proposed the possible bonding structures of the TEG and THF molecules with the $VOPO_4$ layers in Figure 4.19d. TEG molecules were aligned between the $VOPO_4$ layers because the final product exhibited the large interlayer distance. It should be pointed out that the intercalated organic molecules, unlike ferrocene in the fc-$VOPO_4$ system, do not occupy the interlayer space reserved for positively charged ions as they are nearly neutral in nature. This feature is particular advantageous for not interfering further charge storage inside the material.

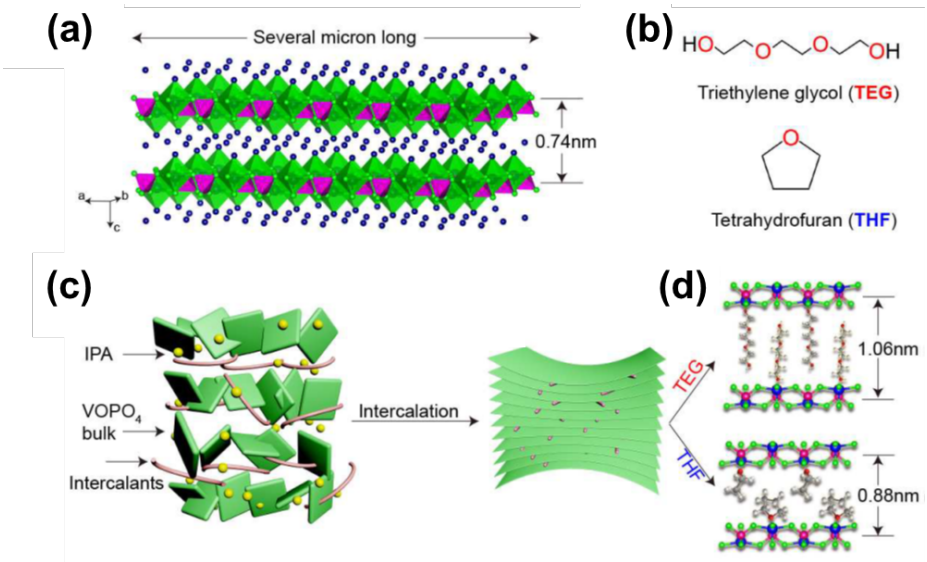

Figure 4.19 Design of organic intercalated $VOPO_4$ with expanded interlayer distance. (a) Crystal structure of the intrinsic $VOPO_4 \cdot 2H_2O$ nanosheets. (b) Chemical structure of the TEG and THF intercalants. (c) Schematic illustration of the intercalation process and the intercalated structure. (d) The bonding structure of the TEG and THF in $VOPO_4$ nanosheets.

The interlayer distances of TEG and THF intercalated $VOPO_4$ were studied with XRD and cross-sectional TEM. As shown in Figure 4.20a, the diffraction peaks corresponding to the interlayer spacing shift to lower angles after the intercalation of TEG and THF molecules. This shift indicates a gradually increased interlayer distance according to Bragg's formula ($d = 0.5\lambda/sin(\theta)$). The interlayer distance of pristine $VOPO_4 \cdot 2H_2O$ bulk microcrystal is calculated to be 0.74 nm. Upon intercalation of organic molecules, the spacings further increase to 0.88 nm for THF intercalated $VOPO_4$ nanosheets (THF-$VOPO_4$) and 1.06 nm for TEG intercalated $VOPO_4$ nanosheets (TEG-$VOPO_4$), corresponding to 20 and 43 % increase, respectively. The calculated spacing values were cross-validated by TEM observation. Figure 4.20b showed the typical STEM

image of TEG-$VOPO_4$ nanosheets with flat surface and ultrathin thickness. Similar morphology and thickness can be obtained in the THF-$VOPO_4$ nanosheets. Focused ion beam (FIB) was used to cut the nanosheets for the cross-sectional TEM characterization. Cross-sectional TEM of the TEG-VOPO4 nanosheets in Figure 4.20c and d shows the well-defined layered structures with ~7 atomic layers and an interlayer distance of ~1 nm, which is consistent with the value obtained from the XRD patterns.

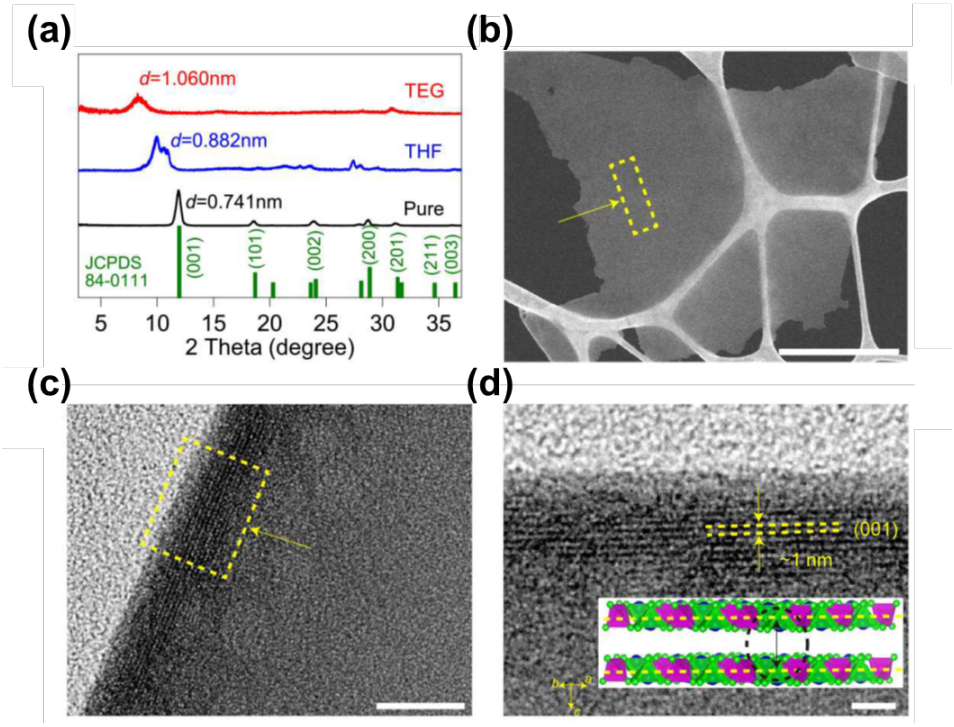

Figure 4.20 Structural characterization of the organic molecule intercalated $VOPO_4$ nanosheets. (a) XRD patterns of pure $VOPO_4 \cdot 2H_2O$, THF and TEG intercalated $VOPO_4$. (b) Typical STEM image of the TEG-$VOPO_4$ nanosheets. Scale bar: 500 nm. (c) Cross-sectional TEM image of 2D TEG-$VOPO_4$ nanosheets. Scale bar: 20 nm. (d) Enlarged picture of the cross-sectional TEM, showing an interlayer distance of ~1 nm. A crystallographic model of the layered structure is shown here, highlighting the (001) planes. Scale bar: 5 nm.

Further characterization gives insights into the chemical composition and structural properties of the interlayer expanded $VOPO_4$ nanosheets. Raman spectra shown in Figure 4.21a verifies the structural properties of the pure $VOPO_4 \cdot 2H_2O$ microcrystals, THF and TEG intercalated $VOPO_4$ nanosheets. The bands at 937 cm^{-1} in the curve of pure sample can be assigned to the symmetric O-P-O stretching modes.[150, 151] Obviously, the symmetry of O-P-O stretching modes is strongly correlated to regional microstructures and very sensitive to the hydrogen bonding between the interlayered H_2O molecules and V atoms. With the intercalation of THF and TEG molecules and removal of the interlayer H_2O, the hydrogen bonds formed between the O atoms of P-O bond in the layer and H_2O are broken, inducing the mitigation of the steric hindrance and the shift of O-P-O stretching modes to lower energy (lower wavenumbers). While the peaks of the symmetric bending vibrations of O-P-O, V-O and V=O stretching mode show little shift in peak positions. Pure $VOPO_4$ spectrum shows a sharp band at 995 cm^{-1} corresponding to a vanadyl V=O stretching vibration, which appears to be particularly sensitive to the atoms coordinated to vanadium within an octahedral arrangement in the host lattice structure. The position of V=O stretching vibration shifts from 995 cm^{-1} in the dihydrate form to 1031 and 1021 cm^{-1} respectively, after the intercalation of TEG and THF molecules into $VOPO_4$. These positions observed in these bands correspond to the coordination of oxygen atoms of TEG and THF to vanadium, respectively.[152] The Raman results indicate that the intercalated $VOPO_4$ samples are found most probably not to contain trapped water, and the intercalated $VOPO_4$ nanosheets maintain the integrity of the in-plane layered $VOPO_4$ structure without obvious structural deformations. TGA of the pure, TEG and THF intercalated $VOPO_4$ samples reveal the weight loss (Figure 4.21b). Pure $VOPO_4 \cdot 2H_2O$ shows a weight loss of ~18%, indicating the loss of the two structural water molecules in the layers. The intercalated samples show weight loss of

~25% and ~30% for THF and TEG intercalated $VOPO_4$ nanosheets, indicating that 0.3 THF molecule and 0.4 TEG molecule per $VOPO_4$ unit has been intercalated.

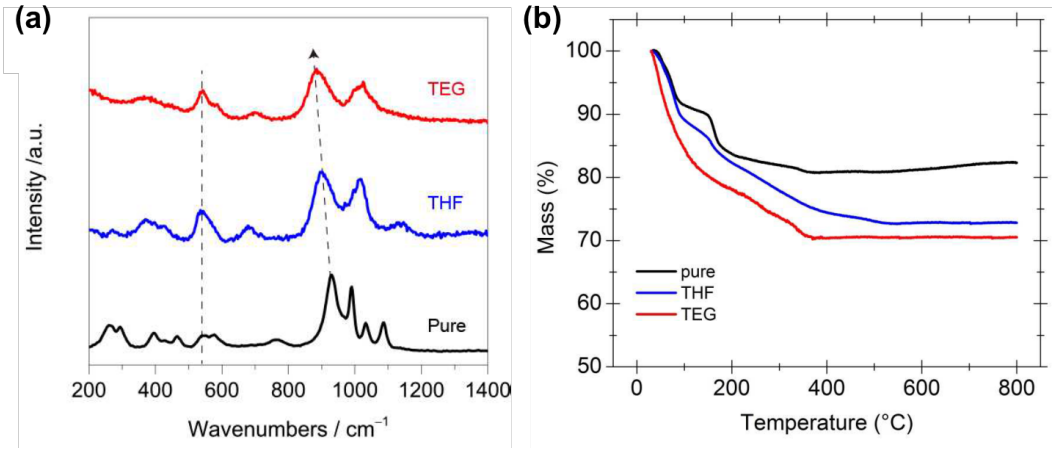

Figure 4.21 (a) Raman spectra and (b) TGA of the pure $VOPO_4 \cdot 2H_2O$ microcrystals and THF and TEF intercalated $VOPO_4$ nanosheets.

To further unravel the chemical bonding/configuration between the organic intercalants and the $VOPO_4$ host layers, synchrotron-based XAS characterization was conducted. Considering the polarity or the dielectric property of the ligand can affect the chemical value of the center metal, XAS, that is sensitive to the partial electronic structure and the local geometry around the selected absorber, in an ideal tool to monitor the change of the chemical configuration of the $VOPO_4$ nanosheet to determine the interaction between vanadium and the different intercalants, such as H_2O, TEG and THF. Figure 4.22a shows the vanadium K-edge X-ray absorption near-edge spectroscopy (XANES) of the $VOPO_4$ nanosheets intercalated with different molecules. The XANES spectra of the vanadium foil and VO_2 were also measured to calibrate the X-ray energy. It is easy to find the edge shifts to the lower energy with the order of H_2O > TEG > THF. That means the chemical value of vanadium in the samples gradually decreases with the

same order. The changes of chemical value in these samples are also reflected by the pre-edge feature of the XANES. The XANES of $VOPO_4{\cdot}2H_2O$ presents an obvious pre-edge peak at 5472.0 eV, labeled by *b*. Besides the peak *b*, the other pre-edge peak, labeled by *a*, appears at 5470.5 eV for the $VOPO_4$-THF. Pre-edge peak at this position is a typical fingerprint of the V^{4+} oxidation state, as shown by the pre-edge peak of VO_2 reference. The energy shift of 1.5 eV indicates the V oxidation state in $VOPO_4{\cdot}2H_2O$ sample is about V^{5+}. Higher oxidation state of the vanadium means the stronger electronegativity of the coordinated molecule for this case. It is known that the electronegativity of TEG is less than that of H_2O but stronger than that of THF. This coherence between the oxidation state of the center vanadium and the electronegativity of the ligand molecules suggests the organic molecules TEG and THF have been successfully intercalated into the $VOPO_4$ nanosheet and coordinated into vanadium.

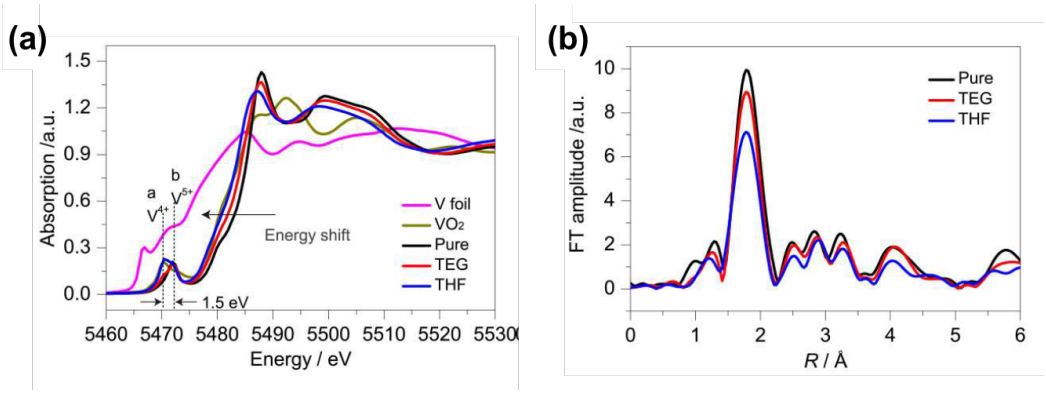

Figure 4.22 (a) K-edge X-ray absorption near-edge spectroscopy (XANES) and (b) extended X-ray absorption fine structure (EXAFS) of the $VOPO_4$ nanosheets intercalated with different molecules.

Inspection of the extended X-ray absorption fine structure (EXAFS) at vanadium K-edge was also performed to check if any rearrangement occurs for the local atomic

environment around the vanadium ion. Figure 4.22b shows the *k*3-weighted Fourier transforms (FT) of the EXAFS oscillations of three prepared samples. All of these FT curves present similar pair distribution functions until the distance of 6 Å, which indicates the integrity of the local structure around vanadium ion is conserved after the intercalation of organic molecules. There are three types of coordinated oxygen atoms in the intercalated $VOPO_4$ nanosheet: 1) the singly coordinated oxygen atom, with a short V-O bond of ~1.57 Å along the *c* axis (perpendicular to the layer); 2) the four-fold coordinated oxygen atoms bridged phosphorus atoms, with V-O bond of ~1.97 Å; 3) an oxygen atom from water or organic molecules out of layers, with a large bond distance of ~2.23 Å. FT curves of these samples only show a strong peak at ~1.79 Å (no phase corrections) and show the four-fold coordinated oxygen atoms from PO_4^{3-} dominates the V-O pair distribution. The position of this peak almost does not change, but its intensity gradually decreases with the order of H_2O > TEG > THF. It means the average distances of V-O bonds of these samples are the same, but the distortion of V-O bonds becomes larger and larger with the intercalation of TEG and THF. This trend is consistent with the change of the chemical value of vanadium ions revealed by XANES spectra discussed above. This is due to the weaker electronegativity of TEG and THF results in the larger dynamics of the coordinated oxygen atoms from the organic group.

To examine electrochemical properties of the 2D TEG and THF intercalated $VOPO_4$ nanosheets, CV, rate capability and cycling stability were measured. Figure 4.23a shows the CV curves of the TEG, THF intercalated $VOPO_4$ nanosheets and the control pure $VOPO_4$ nanosheets at the scan rate of 0.1 mV s^{-1}. All of the three samples exhibit two sharp redox peaks, corresponding to the sodiation/desodiation processes, in the scan range of 2.5 ~ 4.3 V. Figure 4.23b shows the rate performance of the TEG and THF intercalated $VOPO_4$ nanosheets and the pure $VOPO_4$ control sample. Three electrodes are

able to deliver similar capacities of ~151, 149 and 151 mAh g^{-1} at the current density of 0.1C. The capacities are similar because the major contribution to the capacity is from diffusion-controlled process. As the charge/discharge rate increases, three electrodes deliver different capacities indicating their different rate capabilities. As shown in Figure 4.23b, the TEG and THF intercalated $VOPO_4$ nanosheets are able to deliver reversible capacities of 155, 143, 132, 119, 107, 100, 89, 74 mAh g^{-1} and 149, 140, 126, 114, 103, 89, 78, 68 mAh g^{-1}at C rates of 0.1, 0.2, 0.5, 1, 2, 5, 10 and 20. Both samples show better rate performance than the pure $VOPO_4$ nanosheets. The reasons are attributed to the expanded interlayer distances of the TEG and THF intercalated $VOPO_4$ nanosheets, which opens up the inner surfaces for Na-ion storage and facilitates the Na-ion transport between the layers. In addition, Figure 4.23c shows the cycling stability of the three nanosheet electrodes. TEG and THF intercalated $VOPO_4$ nanosheets deliver an average reversible capacity of approximately 88 and 68 mAh g^{-1} at a current rate of 5C and sustain for 500 cycles, showing a capacity retention rate of 88% and 76%. Those values are higher than that of the pure $VOPO_4$ nanosheets (51%).

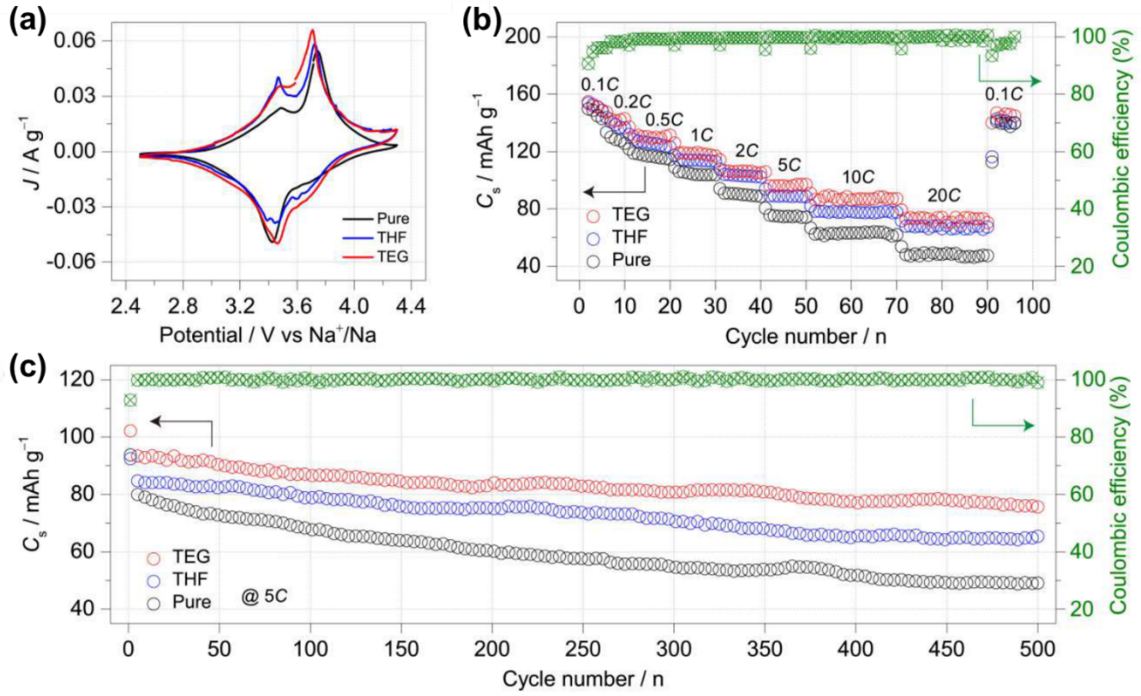

Figure 4.23 Na-ion storage properties of 2D TEG and THF intercalated $VOPO_4$ nanosheets. (a) CV curves of the TEG, THF intercalated $VOPO_4$ nanosheets and the control pure $VOPO_4$ nanosheets at the scan rate of 0.1 mV s^{-1}. (b) Rate performance of the TEG, THF intercalated $VOPO_4$ nanosheets and the control pure $VOPO_4$ nanosheets from the C rates of 0.1C to 20C. (c) Long-term cycling stability and Coulombic efficiency of the TEG, THF intercalated $VOPO_4$ nanosheets and the control pure $VOPO_4$ nanosheets at 5C for over 500 cycles.

A major issue of interlayer expansion strategy via intercalation is whether the intercalated structure could be preserved during electrochemical cycling. Both the intercalated $VOPO_4$ nanosheets show reasonably good electrochemical stability. For TEG the stability in terms of the organic intercalants and morphology was verified by XRD and morphology characterization before and after 500 cycles test (Figure 4.24). This further confirms the inherent stability of the intercalants in the electrodes.

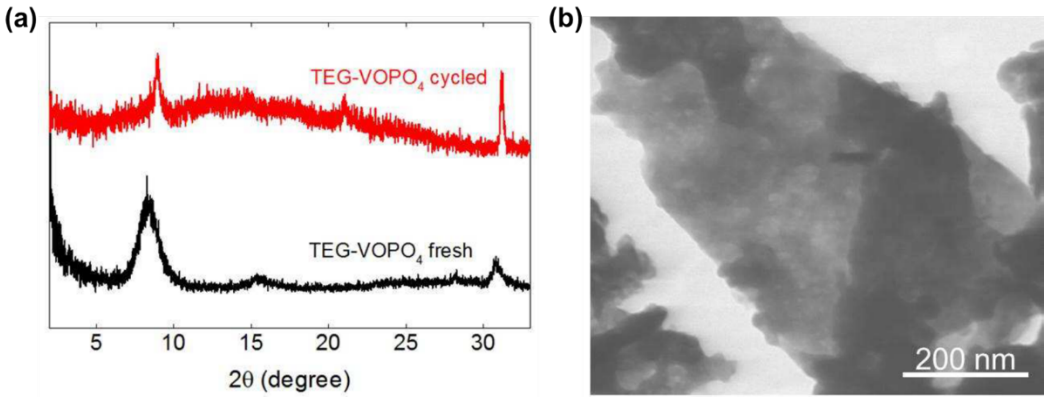

Figure 4.24 (a) XRD pattern and (b) TEM image of the TEG-intercalated $VOPO_4$ nanosheets after cycling tests.

To explore the reasons for the improved electrochemical characteristics for Na-ion storage in intercalated $VOPO_4$ nanosheets, CV measurements at various scan rates were carried out to further understand the electrochemical kinetics using the same analysis used in exfoliated $VOPO_4$ nanosheets previously. For TEG-$VOPO_4$, CV curves at various scan rates from 0.02 to 0.2 mV s^{-1} display similar shapes and a gradual broadening of the peaks can be observed (Figure 4.25a). By plotting log i vs log υ , b-values as the slopes of 0.82 and 0.87 were determined for cathodic and anodic peaks (Figure 4.25b), and capacity contributed by the capacitive process was calculated to be, for example ~70.6%, at scan rate 0.5 mV s^{-1} (Figure 4.25c). Figure 4.25d shows the ratio between the capacitive and diffusion currents at other scan rates. The quantitative results show that the capacitive contribution gradually increases with the increasing scan rate.

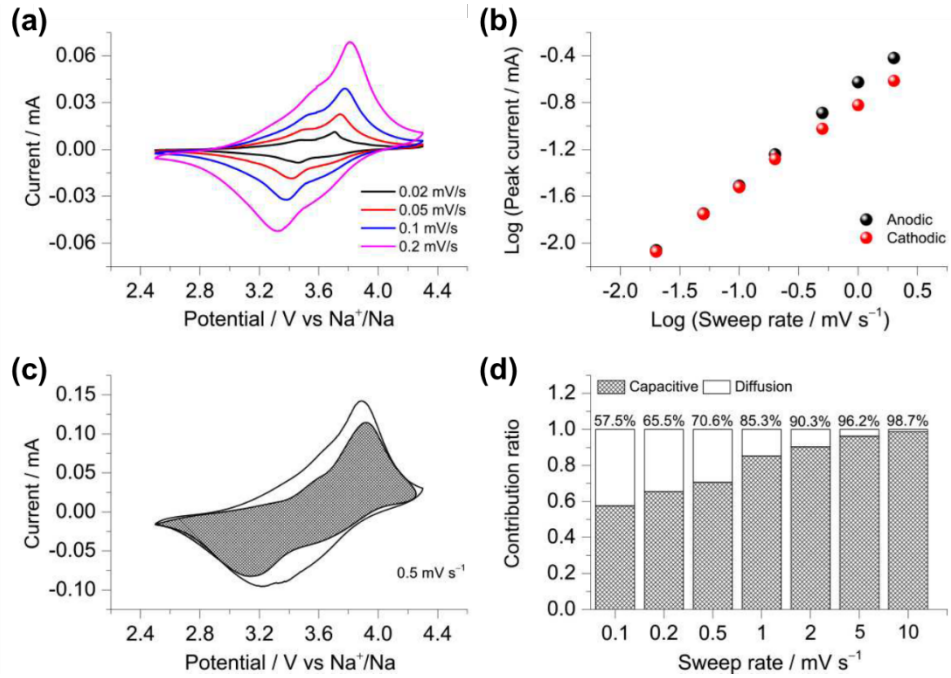

Figure 4.25 Kinetic analysis of TEG intercalated $VOPO_4$ nanosheets for Na-ion storage. (a) CV curves at various scan rates from 0.02 to 0.2 mV s^{-1}. (b) *b*-value evaluation using the relationship between peak current and scan rate. (c) Separation of the capacitive and diffusion currents at a scan rate of 0.5 mV s^{-1}. (d) Contribution ratio of the capacitive and diffusion-controlled processes at various scan rates.

Table 4.1 summarizes key parameters determined from kinetic analysis for pure and organic intercalated $VOPO_4$ nanosheets in both Li- and Na-ion storage devices. The calculated *b*-values and capacitive contributions clearly demonstrate the unique characteristics of intercalation pseudocapacitance in all cases. This advantageous storage behavior verifies the reasons for the improved rate capability and cycling stability in TEG and THF intercalated $VOPO_4$ nanosheets. More importantly, improved kinetics in intercalated nanosheets compared with pure nanosheets has been found for Na-ion storage.

	CV scan range (mV/s)	*b*-value cathodic/anodic	Capacitive contribution at 0.1 mV/s	Polarization between charge/discharge at 0.02 mV/s (mV)
$VOPO_4$ (Li)	0.02 ~ 2	0.86/0.92	70.1%	130
$VOPO_4$ (Na)	0.02 ~ 20	0.68/0.71	43.5%	340
TEG-$VOPO_4$ (Na)	0.02 ~ 10	0.82/0.87	57.5%	244
THF-$VOPO_4$ (Na)	0.02 ~ 10	0.73/0.79	52.1%	270

Table 4.1 Summary of key kinetic parameters of pure and TEG/THF intercalated $VOPO_4$ nanosheets in Li- and Na-ion storage devices.

To validate our structural design and gain fundamental insight into the intercalation effect on the enhanced electrochemical performance, we further performed DFT calculations for the diffusion behavior of Na-ions in the pure and TEG intercalated $VOPO_4$ nanosheets. Computationally, the mobility of Na-ions in $VOPO_4$ nanosheets can be deduced from their migration barriers. In this context, Na-ion migration simulations in the original and modified $VOPO_4$ structures were carried out using the climbing-image nudged elastic band (CI-NEB) method as implemented in VASP software.[153, 154] Two possible diffusion pathways (P1 and P2) are identified in $VOPO_4$ nanosheets (Figure 4.26a), and the pure $VOPO_4$ nanosheets prefer the P1 pathway for Na-ion migration, whereas the TEG intercalated $VOPO_4$ nanosheets with enlarged interlayer distance is in favor of P2. Especially, compared with the pure $VOPO_4$ nanosheets (E_{ba} = ~ 0.72 eV), Na-ion diffusion over TEG intercalated $VOPO_4$ nanosheets exhibits a much lower E_{ba} of ~ 0.22 eV (Figure 4.26b). Since the diffusion energy barrier describes the minimum energy which must be overcome for the Na-ion diffusion in the $VOPO_4$ layers, the values of the energy barriers are closely related to the difficulty of the Na-ion transport.

Therefore, the increased interlayer distances should be the essential reason for the enhanced electrochemical performance in the intercalated $VOPO_4$ nanosheets. Our simulation results not only provide the theoretical evidence for the greatly improved rate capability and cycling stability in the TEG and THF intercalated $VOPO_4$ nanosheets, but also strongly suggest that interlayer-expansion strategy is effective to improve the diffusion kinetics of large cations (such as Na-ion) in layer-structured hosts.

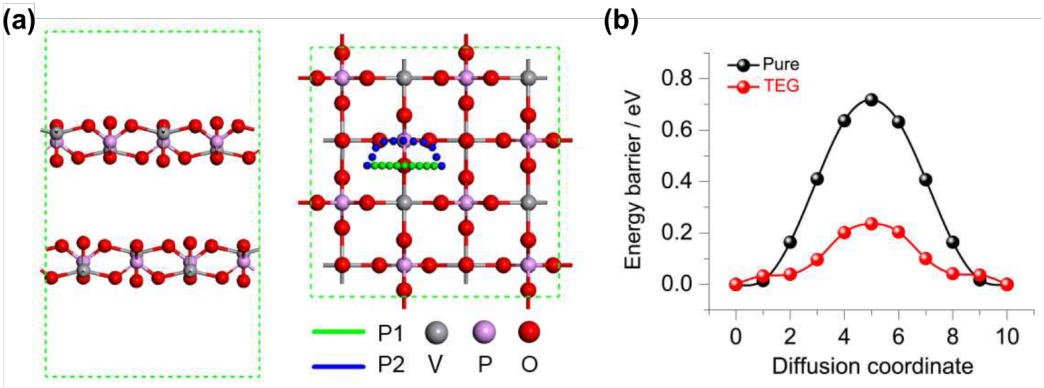

Figure 4.26 DFT calculations of Na-ion transport in pure and TEG intercalated $VOPO_4$ nanosheets. (a) Views of geometric structures of $VOPO_4$ nanosheets (left) and diffusion pathways of Na-ion (right). (b) Diffusion barrier (minimum energy path) profiles of Na-ion transport in pure and the TEG intercalated $VOPO_4$ nanosheets.

To conclude, we have demonstrated controlled interlayer engineering of ultrathin $VOPO_4$ nanosheets with significantly improved Na-ion transport and storage characteristics achieved by an effective organic intercalation. The intercalated $VOPO_4$ nanosheets show expanded interlayer distance, and because of the different structures of the organic molecular intercalants, TEG and THF intercalated $VOPO_4$ nanosheets exhibits expanded interlayer distance of 1.06 nm and 0.88 nm, respectively. Synchrotron-based XAS, for the first time, was used to study the chemical bonding between the

organic intercalants and the $VOPO_4$ host layers. The XAS results show that the organic intercalants are successfully intercalated into individual $VOPO_4$ layer. Due to the expanded interlayer spacing in combination with the uniform intercalation of intercalants in $VOPO_4$, the interlayer-engineered $VOPO_4$ nanosheets show enhanced Na-ion transport kinetics, as well as much improved rate capability and cycling stability for Na-ion storage, compared with the pure $VOPO_4$ nanosheets without intercalation of organic molecules. DFT calculations of the energy barriers validate the observation of superior Na-ion transport in 2D TEG intercalated $VOPO_4$ nanosheets. Specifically, the energy barrier for Na-ion transport in TEG intercalated $VOPO_4$ nanosheets (0.22 eV) is reduced by two thirds of the pure $VOPO_4$ nanosheets (0.72 eV). The success of intercalation strategy in this case, combined with the setback from fc-$VOPO_4$ system, implies that a deeper understanding of the intercalated structure is required to generalize the design principle, even for the same intercalation host.

4.5 CONCLUSION

2D layered materials are ideal candidates to be explored as charge storage hosts for EES devices. A set of chemical and physical properties are needed to achieve high electrochemical activities that are required for their energy storage applications. Many old material systems that previously suffered from their poor intrinsic properties can be engineered to exhibit much improved electrochemical performance with proper structural modifications. The nanostructuring of $VOPO_4 \cdot 2H_2O$ microcrystals by means of exfoliation has been demonstrated to produce ultrathin nanosheets with outstanding alkali-ion storage capabilities. Though such miniaturization strategy seems promising with the rapid development of corresponding synthetic methods, it is still difficult to

predict the effectiveness of such strategy among the broad spectrum of 2D nanomaterials. At the heart of this insufficiency is the lack of interpretation on their charge storage mechanisms. The interesting charge storage properties in the nanosheets of $NbOPO_4$ hydrates illustrate the complex interplay between the intercalated ions and interlayer structures.

A special structural feature of 2D layered materials, the interlayer space, provides a unique engineering option toward tuning their charge storage properties. The interlayer space can be opened up toward more storage via intercalation, but it has to be done in a careful and raitonal way. This concept has been demonstrated by intercalation of small organic molecules in $VOPO_4$ nanosheets showing enhanced rate capability and cylcing stability for Na-ion storage. The general synthesis of the organic intercalated $VOPO_4$ nanosheets can be extended to other organic molecules, such as amines and alcohols, as well as to other 2D layered materials. Our results may also bring a unique perspective in structural design of energy storage electrode materials for enabling future generation of large-scale energy storage systems beyond Li^+, such as Na^+, K^+, Mg^{2+}, and Al^{3+}.

Chapter 5: Concluding remarks

5.1 DISSERTATION SUMMARY

In this dissertation, research to advance the understanding of intercalation chemistry and charge storage mechanism in 2D layered materials, as well as application of these materials as electrode materials in electrochemical energy storage devices, has been presented. This research was conducted under the background that the society is on the verge of transition to a renewable-energy-powered sustainable future. Batteries, as a key energy storage technology for renewables, that are now electrifying phones, laptops, and even electric vehicles, are deemed to power houses, cities, and our lives in the future. Developing revolutionary battery technologies needs to venture deep inside the battery, thus it is imperative to study the electrode materials and associated fundamental physicochemical processes in minute detail.

Intercalation chemistry of layered materials is the cornerstone of commercial lithium-ion batteries, and it is still an active field with new developments and fruitful applications. This work is composed of two parts concerning two important questions in this field, for which previous research has not been able to provide satisfactory answers. The first part discusses solvent effects in intercalation chemistry. For a specific guest-host system, it has been known that thermodynamics of its solution-phase intercalation is highly solvent dependent. However, much less has been explored in kinetic effect of the solvent. A typical question in this regard is why the intercalation reaction is much faster in certain solvents. The second part discusses charge storage properties of pre-intercalated layered materials. While much research effort has been devoted to the ion transport/storage in traditional layered materials, very little has been known for charge storage in layered materials with pre-intercalated molecules via chemical syntheses or

structural engineering strategies. A critical question to ask in these materials is how ions are transported and stored in the occupied interlayer spaces.

The material system used in this work, $MOPO_4$ (M=V, Nb) hydrates, serves as an ideal platform to study above mentioned fundamental questions. $VOPO_4 \cdot 2H_2O$ is a host capable of incorporating ferrocene into its interlayer space, and kinetics of this intercalation reaction is highly solvent dependent. This solvent effect has not been recognized previously, making interpretation of intercalated structure and determination of guest configuration difficult. In a comparative study of the intercalation in two solvents, a much faster intercalation kinetics has been found in 2-propanol over the conventionally used acetone, leading to a complete phase transformation and almost fully intercalated structure that has never been reported. Theoretical modeling of this structure has successfully revealed the orientation and distribution of ferrocene molecules inside the host, matching perfectly to the experimental results. Inspired by the observed solvent dependent intercalation, a systematic study of the intercalation kinetics in a variety of solvents has been conducted with an emphasis on primary alcohols, in which the intercalation rate follows a volcano shape with respect to the number of carbons. The subsequent discovery of exfoliation phenomena in pure solvents and a similar solvent dependence in this process leads to the conclusion that fast intercalation kinetics is induced by strong solvent-host interaction. Finally, the role of solvent in this intercalation system is understood at atomic level as a synergistic effect of intralayer interactions, interlayer expansion, and layer sliding with valuable inputs from theoretical modeling.

$MOPO_4$ hydrates in the form of nanosheets are promising electrode materials for storing alkali-ions. The study of their charge storage properties is possible because we are able to produce the nanosheets of $NbOPO_4$ hydrates via a bottom-up solution synthesis and that of $VOPO_4 \cdot 2H_2O$ via a top-down approach based on liquid exfoliation. These

hydrates can be considered as pre-intercalated layered materials due to the presence of crystal water, and in the case of $NbOPO_4$, a PO_4 group intercalated structure exists to make this material system more interesting and more complicated. By probing structural evolutions during the reversible intercalation of alkali-ions, the intriguing role of H_2O molecule and PO_4 group has been revealed in the charge storage properties of these pre-intercalated materials. In particular, the pillaring effect of PO_4 group in preserving interlayer stability of $NbOPO_4$ during electrochemical cycling has been recognized. $VOPO_4$ does not form such pillared structure during its chemical synthesis, however, the same concept has been demonstrated via a controlled organic intercalation to achieve a pre-intercalated and interlayer expanded structure with improved charge storage capability.

Although the research presented in this dissertation has been focused on a specific material system, the insights provided into fundamental aspects of intercalation chemistry and the concepts developed for structural engineering of layered materials shall make a meaningful contribution to the field of materials science and engineering.

5.2 FUTURE DIRECTIONS

To fully exploit its potential in energy storage, the research of 2D layered materials should go both down to single nanosheet level for fundamental studies and up to macroscopic assemblies for practical applications (Figure 5.1). When their thickness is confined to mono- or few-layer, 2D layered materials usually exhibit unprecedented physical and chemical properties, many of which are beneficial toward effective and efficient charge transport and storage. Another intriguing feature of 2D materials is their ability to form heterostructures exhibiting exotic properties originated from the

heterointerfaces. As molecular-scale manipulation of electronic and ionic charge accumulation in materials is of critical importance to their electrochemical properties, the structural diversity of 2D layered materials enables the interfacial properties of composites to be optimized toward rationally designed energy storage devices.[155] On the other hand, the scalable and sustainable manufacture of thick electrode films with high energy and power densities is of critical importance for the large-scale application of 2D layered materials toward practical energy storage devices. Strategies are need to achieve designed electrode structure with precise control of ion transport in the assembly of individual nanosheets.[156]

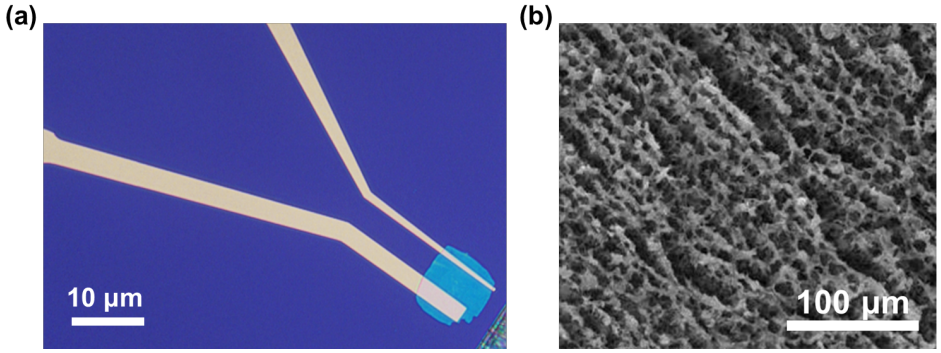

Figure 5.1 Possible future directions of exploiting 2D layered materials in energy storage, taking $VOPO_4$ as an example. (a) Single-nanosheet or heterostructure based electrochemical device for studying fundamental material properties. (b) Large-scale assembly of nanosheets toward high power/energy.

To conclude this dissertation, the study of 2D layered materials on fundamental intercalation chemistry and charge storage properties will remain very important topics and will continue to be an indispensable part of materials science going forward.

References

1. Whittingham, M. S.; Jacobson, A. J. *Intercalation Chemistry*, Academic Press, New York, USA **1982**.
2. Schöllhorn, R. *Angew Chem. Int. Ed. Engl.* **1980,** 19, 983-1003.
3. Lerf, A. *Dalton Trans.* **2014,** 43, 10276-10291.
4. Dresselhaus, M. S. *Intercalation in layered materials,* Plenum Press, New York, USA **1986**.
5. Schafhaeutl, C. *J. Prakt. Chem.* **1840,** 21, 129-157.
6. Whittingham, M. S. *Chem. Rev.* **2004,** 104, 4271-4302.
7. Schubert, U.; Hüsing, N. *Synthesis of Inorganic Materials*, Wiley-VCH Verlag & Co. KGaA, Weinheim, Germany **2012**.
8. Geim, A. K.; Novoselov, K. S. *Nat. Mater.* **2007,** 6, 183-191.
9. Xu, M.; Liang, T.; Shi, M.; Chen, H. *Chem. Rev.* **2013,** 113, 3766-3798.
10. Nicolosi, V.; Chhowalla, M.; Kanatzidis, M. G.; Strano, M. S.; Coleman, J. N. *Science* **2013,** 340, 1226419.
11. Wang, H.; Yuan, H.; Sae Hong, S.; Li, Y.; Cui, Y. *Chem. Soc. Rev.* **2015,** 44, 2664-2680.
12. Wan, J.; Lacey, S. D.; Dai, J.; Bao, W.; Fuhrer, M. S.; Hu, L. *Chem. Soc. Rev.* **2016,** 45, 6742-6765.
13. Lee, H. J.; Shin, J.; Choi, J. W. *Adv. Mater.* **2018,** 30, 1705851.
14. Zhu, Y.; Peng, L.; Fang, Z.; Yan, C.; Zhang, X.; Yu, G. *Adv. Mater.* **2018,** 30, 1706347.
15. Goodenough, J. B. *Energy Environ. Sci.* **2014,** 7, 14-18.
16. Lu, L.; Han, X.; Li, J.; Hua, J.; Ouyang, M. *J. Power Sources* **2013,** 226, 272-288.
17. Augustyn, V.; Simon, P.; Dunn, B. *Energy Environ. Sci.* **2014,** 7, 1597-1614.
18. Olivetti, E. A.; Ceder, G.; Gaustad, G. G.; Fu, X. *Joule* **2017,** 1, 229-243.
19. Nitta, N.; Wu, F.; Lee, J. T.; Yushin, G. *Mater. Today* **2015,** 18, 252-264.
20. Peng, L.; Zhu, Y.; Chen, D.; Ruoff, R. S.; Yu, G. *Adv. Energy Mater.* **2016,** 6, 1600025.
21. Bonaccorso, F.; Colombo, L.; Yu, G.; Stoller, M.; Tozzini, V.; Ferrari, A. C.; Ruoff, R. S.; Pellegrini, V. *Science* **2015,** 347, 1246501.
22. Zhang, H. *ACS Nano* **2015,** 9, 9451-9469.
23. Tang, Y.; Zhang, Y.; Li, W.; Ma, B.; Chen, X. *Chem. Soc. Rev.* **2015,** 44, 5926-5940.
24. Abraham, A.; Housel, L. M.; Lininger, C. N.; Bock, D. C.; Jou, J.; Wang, F.; West, A. C.; Marschilok, A. C.; Takeuchi, K. J.; Takeuchi, E. S. *ACS Cent. Sci.* **2016,** 2, 380-387.
25. Wan, J.; Bao, W.; Liu, Y.; Dai, J.; Shen, F.; Zhou, L.; Cai, X.; Urban, D.; Li, Y.; Jungjohann, K.; Fuhrer, M. S.; Hu, L. *Adv. Energy Mater.* **2015,** 5, 1401742.
26. Xiong, F.; Wang, H.; Liu, X.; Sun, J.; Brongersma, M.; Pop, E.; Cui, Y. *Nano Lett.* **2015,** 15, 6777-6784.

27. Novoselov, K. S.; Jiang, D.; Schedin, F.; Booth, T. J.; Khotkevich, V. V.; Morozov, S. V.; Geim, A. K. *Proc. Natl. Acad. Sci.* **2005,** 102, 10451-10453.
28. Novoselov, K. S.; Geim, A. K.; Morozov, S. V.; Jiang, D.; Zhang, Y.; Dubonos, S. V.; Grigorieva, I. V.; Firsov, A. A. *Science* **2004,** 306, 666-669.
29. Bhimanapati, G. R.; Lin, Z.; Meunier, V.; Jung, Y.; Cha, J.; Das, S.; Xiao, D.; Son, Y.; Strano, M. S.; Cooper, V. R.; Liang, L.; Louie, S. G.; Ringe, E.; Zhou, W.; Kim, S. S.; Naik, R. R.; Sumpter, B. G.; Terrones, H.; Xia, F.; Wang, Y.; Zhu, J.; Akinwande, D.; Alem, N.; Schuller, J. A.; Schaak, R. E.; Terrones, M.; Robinson, J. A. *ACS Nano* **2015,** 9, 11509-11539.
30. Tao, L.; Cinquanta, E.; Chiappe, D.; Grazianetti, C.; Fanciulli, M.; Dubey, M.; Molle, A.; Akinwande, D. *Nat. Nano.* **2015,** 10, 227.
31. Tan, C.; Zhang, H. *Nat. Commun.* **2015,** 6, 7873.
32. Dou, Y.; Zhang, L.; Xu, X.; Sun, Z.; Liao, T.; Dou, S. X. *Chem. Soc. Rev.* **2017,** 46, 7338-7373.
33. Fiori, G.; Bonaccorso, F.; Iannaccone, G.; Palacios, T.; Neumaier, D.; Seabaugh, A.; Banerjee, S. K.; Colombo, L. *Nat. Nano.* **2014,** 9, 768.
34. Mak, K. F.; Shan, J. *Nat. Photonics* **2016,** 10, 216.
35. Schaibley, J. R.; Yu, H.; Clark, G.; Rivera, P.; Ross, J. S.; Seyler, K. L.; Yao, W.; Xu, X. *Nat. Rev. Mater.* **2016,** 1, 16055.
36. Anichini, C.; Czepa, W.; Pakulski, D.; Aliprandi, A.; Ciesielski, A.; Samorì, P. *Chem. Soc. Rev.* **2018,** 47, 4860-4908.
37. Anasori, B.; Lukatskaya, M. R.; Gogotsi, Y. *Nat. Rev. Mater.* **2017,** 2, 16098.
38. Peng, L.; Fang, Z.; Zhu, Y.; Yan, C.; Yu, G. *Adv. Energy Mater.* **2018,** 8, 1702179.
39. Mueller, T.; Hautier, G.; Jain, A.; Ceder, G. *Chem. Mater.* **2011,** 23, 3854-3862.
40. Tietze, H. *Aust. J. Chem.* **1981,** 34, 2035-2038.
41. Čapková, P.; Vácha, J.; Votinský, J. *J. Phys. Chem. Solids* **1992,** 53, 215-218.
42. Tachez, M.; Theobald, F.; Bordes, E. *J. Solid State Chem.* **1981,** 40, 280-283.
43. Jordan, B.; Calvo, C. *Can. J. Chem.* **1973,** 51, 2621-2625.
44. Ladwig, G. *Z. Anorg. Allg. Chem.* **1965,** 338, 266-278.
45. Gautier, R.; Audebrand, N.; Furet, E.; Gautier, R.; Fur, E. L. *Inorg. Chem.* **2011,** 50, 4378-4383.
46. Mizuno, N.; Hatayama, H.; Misono, M. *Chem. Mater.* **1997,** 9, 2697-2698.
47. Johnson, J. W.; Johnston, D. C.; Jacobson, A. J.; Brody, J. F. *J. Am. Chem. Soc.* **1984,** 106, 8123-8128.
48. Shpeizer, B. G.; Ouyang, X.; Heising, J. M.; Clearfield, A. *Chem. Mater.* **2001,** 13, 2288-2296.
49. Hahn, R. B. *J. Am. Chem. Soc.* **1951,** 73, 5091-5093.
50. Longo, J. M.; Kierkegaard, P. *Acta Chem. Scand.* **1966,** 20, 72-78.
51. Beneke, K.; Lagaly, G. *Inorg. Chem.* **1983,** 22, 1503-1507.
52. Bruque, S.; Martinez-Lara, M.; Moreno-Real, L.; Jimenez-Lopez, A.; Casal, B.; Ruiz-Hitzky, E.; Sanz, J. *Inorg. Chem.* **1987,** 26, 847-850.

53. Zima, V.; Vlček, M.; Beneš, L.; Casciola, M.; Massinelli, L.; Palombari, R. *Chem. Mater.* **1996,** 8, 2505-2509.
54. Zima, V.; Beneš, L.; Melánová, K.; Casciola, M.; Cruccolini, A. *J. Solid State Chem.* **2005,** 178, 1778-1785.
55. Kinomura, N.; Kumada, N. *Inorg. Chem.* **1990,** 29, 5217-5222.
56. Harrison, W. T. A.; Hsu, K.; Jacobson, A. J. *Chem. Mater.* **1995,** 7, 2004-2006.
57. Peascoe, R.; Clearfield, A. *J. Solid State Chem.* **1991,** 95, 289-299.
58. Dupré, N.; Gaubicher, J.; Le Mercier, T.; Wallez, G.; Angenault, J.; Quarton, M. *Solid State Ionics* **2001,** 140, 209-221.
59. Kubota, M. *J. Radioanal. Chem.* **1982,** 75, 39-49.
60. Wang, S.; Quan, W.; Zhu, Z.; Yang, Y.; Liu, Q.; Ren, Y.; Zhang, X.; Xu, R.; Hong, Y.; Zhang, Z.; Amine, K.; Tang, Z.; Lu, J.; Li, J. *Nat. Commun.* **2017,** 8, 627.
61. Jehng, J.-M.; Wachs, I. E. *J. Raman Spectrosc.* **1991,** 22, 83-89.
62. Jehng, J. M.; Wachs, I. E. *Chem. Mater.* **1991,** 3, 100-107.
63. Beneš, L.; Melánová, K.; Svoboda, J.; Zima, V. *J. Inclusion Phenom. Macrocyclic Chem.* **2012,** 73, 33-53.
64. Beneš, L.; Zima, V. *J. Inclusion Phenom.* **1994,** 20, 381-391.
65. Beneš, L.; Melánová, K.; Zima, V.; Kalousová, J.; Votinský, J. *Inorg. Chem.* **1997,** 36, 2850-2854.
66. Melánová, K.; Beneš, L.; Zima, V.; Vahalová, R.; Kilián, M. *Chem. Mater.* **1999,** 11, 2173-2178.
67. Kinomura, N.; Toyama, T.; Kumada, N. *Solid State Ionics* **1995,** 78, 281-286.
68. Nakato, T.; Furumi, Y.; Terao, N.; Okuhara, T. *J. Mater. Chem.* **2000,** 10, 737-743.
69. Melánová, K.; Beneš, L.; Zima, V.; Votinský, J. *J. Solid State Chem.* **2001,** 157, 50-55.
70. Čapková, P.; Trchová, M.; Zima, V.; Schenk, H. *J. Solid State Chem.* **2000,** 150, 356-362.
71. Johnson, J. W.; Jacobson, A. J.; Brody, J. F.; Rich, S. M. *Inorg. Chem.* **1982,** 21, 3820-3825.
72. Yatabe, T.; Nakano, M.; Matsubayashi, G. *J. Mater. Chem.* **1998,** 8, 699-703.
73. Benš, L.; Votinský, J.; Kalousová, J.; Handlíř, K. *Inorg. Chim. Acta* **1990,** 176, 255-259.
74. Johnson, J. W.; Jacobson, A. J. *Angew. Chem. Int. Ed. Engl.* **1983,** 22, 412-413.
75. Jacobson, A. J.; Johnson, J. W.; Brody, J. F.; Scanlon, J. C.; Lewandowski, J. T. *Inorg. Chem.* **1985,** 24, 1782-1787.
76. Ramos-Barrado, J. R.; Criado, C.; Rodríguez-Castellón, E.; Olivera-Pastor, P.; Jiménez-López, A. *Solid State Ionics* **1997,** 97, 213-216.
77. Zima, V.; x; tězslav; Beneš, L.; x; Melánová, K.; Svoboda, J. *J. Solid State Chem.* **2004,** 177, 1173-1178.
78. Lara, M. M.; Lopez, A. J.; Real, L. M.; Bruque, S.; Casal, B.; Ruiz-Hitzky, E. *Mater. Res. Bull.* **1985,** 20, 549-555.
79. Dines, M. B. *Science* **1975,** 188, 1210-1211.

80. Schäfer-Stahl, H.; Abele, R. *Angew. Chem. Int. Ed. Engl.* **1980,** 19, 477-478.
81. Rodríguez-Castellón, E.; Jiménez-Ĺopez, A.; Martínez-Lara, M.; Moreno-Real, L. *J. Inclusion Phenom.* **1987,** 5, 335-342.
82. Santiago, M. E. B.; Declet-Flores, C.; Díaz, A.; Vélez, M. M.; Bosques, M. Z.; Sanakis, Y.; Colón, J. L. *Langmuir* **2007,** 23, 7810-7817.
83. O'Hare, D.; Evans, J. S. O.; Wiseman, P. J.; Prout, K. *Angew. Chem. Int. Ed. Engl.* **1991,** 30, 1156-1158.
84. Wong, H.-V.; Evans, J. S. O.; Barlow, S.; Mason, S. J.; O'Hare, D. *Inorg. Chem.* **1994,** 33, 5515-5521.
85. Matsubayashi, G.; Ohta, S. *Chem. Lett.* **1990,** 19, 787-790.
86. Davidson, A.; Villeneuve, G.; Fournes, L.; Smith, H. *Mater. Res. Bull.* **1992,** 27, 357-366.
87. Jeon, N. J.; Noh, J. H.; Kim, Y. C.; Yang, W. S.; Ryu, S.; Seok, S. I. *Nat. Mater.* **2014,** 13, 897-903.
88. Wan, C.; Gu, X.; Dang, F.; Itoh, T.; Wang, Y.; Sasaki, H.; Kondo, M.; Koga, K.; Yabuki, K.; Snyder, G. J.; Yang, R.; Koumoto, K. *Nat. Mater.* **2015,** 14, 622-627.
89. Li, Z.; Zhao, Y.; Mu, K.; Shan, H.; Guo, Y.; Wu, J.; Su, Y.; Wu, Q.; Sun, Z.; Zhao, A.; Cui, X.; Wu, C.; Xie, Y. *J. Am. Chem. Soc.* **2017,** 139, 16398-16404.
90. Wang, C.; He, Q.; Halim, U.; Liu, Y.; Zhu, E.; Lin, Z.; Xiao, H.; Duan, X.; Feng, Z.; Cheng, R.; Weiss, N. O.; Ye, G.; Huang, Y.-C.; Wu, H.; Cheng, H.-C.; Shakir, I.; Liao, L.; Chen, X.; Goddard Iii, W. A.; Huang, Y.; Duan, X. *Nature* **2018,** 555, 231.
91. Reichardt, C.; Welton, T.; Welton, T. *Solvents and solvent effects in organic chemistry*, Wiley-VCH Verlag & Co. KGaA, Weinheim, Germany, **2011**.
92. Dresselhaus, M. S.; Dresselhaus, G. *Adv. Phys.* **1981,** 30, 139-326.
93. Augustyn, V.; Gogotsi, Y. *Joule* **2017,** 1, 443-452.
94. Shih, C.-J.; Lin, S.; Strano, M. S.; Blankschtein, D. *J. Am. Chem. Soc.* **2010,** 132, 14638-14648.
95. Liu, Y.; Merinov, B. V.; Goddard, W. A. *Proc. Natl. Acad. Sci.* **2016,** 113, 3735-3739.
96. Evans, J. S. O.; Price, S. J.; Wong, H.-V.; O'Hare, D. *J. Am. Chem. Soc.* **1998,** 120, 10837-10846.
97. Khawam, A.; Flanagan, D. R. *J. Phys. Chem. B* **2006,** 110, 17315-17328.
98. Draxl, C.; Nabok, D.; Hannewald, K. *Acc. Chem. Res.* **2014,** 47, 3225-3232.
99. Hafner, J. *J. Comput. Chem.* **2008,** 29, 2044-2078.
100. Perdew, J. P.; Burke, K.; Ernzerhof, M. *Phys. Rev. Lett.* **1996,** 77, 3865-3868.
101. Hendricks, S.; Teller, E. *J. Chem. Phys.* **1942,** 10, 147-167.
102. Johnston, D. C.; Frysinger, S. P. *Phys. Rev. B* **1984,** 30, 980-984.
103. Wu, C.; Lu, X.; Peng, L.; Xu, K.; Peng, X.; Huang, J.; Yu, G.; Xie, Y. *Nat. Commun.* **2013,** 4, 2431.
104. Ludwig, T.; Guo, L.; McCrary, P.; Zhang, Z.; Gordon, H.; Quan, H.; Stanton, M.; Frazier, R. M.; Rogers, R. D.; Wang, H.-T.; Turner, C. H. *Langmuir* **2015,** 31, 3644-3652.

105. Choi, J.; Zhang, H.; Du, H.; Choi, J. H. *ACS Appl. Mater. Interfaces* **2016,** 8, 8864-8869.
106. Wu, Y.; Liu, N. *Chem* **2018,** 4, 438-465.
107. Cohn, A. P.; Share, K.; Carter, R.; Oakes, L.; Pint, C. L. *Nano Lett.* **2016,** 16, 543-548.
108. Yoon, G.; Kim, H.; Park, I.; Kang, K. *Adv. Energy Mater.* **2017,** 7, 1601519.
109. Peng, L.; Zhu, Y.; Peng, X.; Fang, Z.; Chu, W.; Wang, Y.; Xie, Y.; Li, Y.; Cha, J. J.; Yu, G. *Nano Lett.* **2017,** 17, 6273-6279.
110. Atkins, A. J.; Bauer, M.; Jacob, C. R. *Phys. Chem. Chem. Phys.* **2013,** 15, 8095-8105.
111. Kovtyukhova, N. I.; Wang, Y.; Berkdemir, A.; Cruz-Silva, R.; Terrones, M.; Crespi, V. H.; Mallouk, T. E. *Nat. Chem.* **2014,** 6, 957-963.
112. Jung, Y.; Zhou, Y.; Cha, J. J. *Inorg. Chem. Front.* **2016,** 3, 452-463.
113. Yamamoto, N.; Hiyoshi, N.; Okuhara, T. *Chem. Mater.* **2002,** 14, 3882-3888.
114. Divigalpitiya, W. M. R.; Frindt, R. F.; Morrison, S. R. *Science* **1989,** 246, 369-371.
115. Kresse, G.; Furthmüller, J. *Phys. Rev. B* **1996,** 54, 11169-11186.
116. Blöchl, P. E. *Phys. Rev. B* **1994,** 50, 17953-17979.
117. Grimme, S.; Antony, J.; Ehrlich, S.; Krieg, H. *J. Chem. Phys.* **2010,** 132, 154104.
118. Monkhorst, H. J.; Pack, J. D. *Phys. Rev. B* **1976,** 13, 5188-5192.
119. Sinclair, R. C.; Suter, J. L.; Coveney, P. V. *Adv. Mater.* **2018,** 30, 1705791.
120. Sun, Y.; Wu, C.; Xie, Y. *J. Nanopart. Res.* **2010,** 12, 417-427.
121. Park, N.-G.; Kim, K. M.; Chang, S. H. *Electrochem. Commun.* **2001,** 3, 553-556.
122. Allen, C. J.; Jia, Q.; Chinnasamy, C. N.; Mukerjee, S.; Abraham, K. M. *J. Electrochem. Soc.* **2011,** 158, A1250-A1259.
123. Shahul Hameed, A.; Nagarathinam, M.; Reddy, M. V.; Chowdari, B. V. R.; Vittal, J. J. *J. Mater. Chem.* **2012,** 22, 7206-7213.
124. Harrison, K. L.; Bridges, C. A.; Segre, C. U.; Varnado, C. D.; Applestone, D.; Bielawski, C. W.; Paranthaman, M. P.; Manthiram, A. *Chem. Mater.* **2014,** 26, 3849-3861.
125. Dupré, N.; Gaubicher, J.; Angenault, J.; Quarton, M. *J. Solid State Electrochem.* **2004,** 8, 322-329.
126. Aricò, A. S.; Bruce, P.; Scrosati, B.; Tarascon, J.-M.; van Schalkwijk, W. *Nat. Mater.* **2005,** 4, 366-377.
127. Wen, Y.; He, K.; Zhu, Y.; Han, F.; Xu, Y.; Matsuda, I.; Ishii, Y.; Cumings, J.; Wang, C. *Nat. Commun.* **2014,** 5, 4033.
128. Hu, Z.; Wang, L.; Zhang, K.; Wang, J.; Cheng, F.; Tao, Z.; Chen, J. *Angew. Chem. Int. Ed.* **2014,** 53, 12794-12798.
129. Trasatti, S.; Buzzanca, G. *J. Electroanal. Chem. Interfacial Electrochem.* **1971,** 29, A1-A5.
130. Simon, P.; Gogotsi, Y.; Dunn, B. *Science* **2014,** 343, 1210-1211.
131. Augustyn, V.; Come, J.; Lowe, M. A.; Kim, J. W.; Taberna, P.-L.; Tolbert, S. H.; Abruña, H. D.; Simon, P.; Dunn, B. *Nat. Mater.* **2013,** 12, 518-522.

132. Augustyn, V.; White, E. R.; Ko, J.; Gruner, G.; Regan, B. C.; Dunn, B. *Mater. Horiz.* **2014,** 1, 219-223.
133. Chen, C.; Wen, Y.; Hu, X.; Ji, X.; Yan, M.; Mai, L.; Hu, P.; Shan, B.; Huang, Y. *Nat. Commun.* **2015,** 6, 6929.
134. Eda, G.; Yamaguchi, H.; Voiry, D.; Fujita, T.; Chen, M.; Chhowalla, M. *Nano Lett.* **2011,** 11, 5111-5116.
135. Ling, C.; Zhang, R.; Mizuno, F. *J. Mater. Chem. A* **2014,** 2, 12330-12339.
136. Whittingham, M. S.; Song, Y.; Lutta, S.; Zavalij, P. Y.; Chernova, N. A. *J. Mater. Chem.* **2005,** 15, 3362-3379.
137. Wang, J.; Polleux, J.; Lim, J.; Dunn, B. *J. Phys. Chem. C* **2007,** 111, 14925-14931.
138. Azmi, B. M.; Ishihara, T.; Nishiguchi, H.; Takita, Y. *J. Power Sources* **2003,** 119–121, 273-277.
139. Zhao, Y.; Peng, L.; Liu, B.; Yu, G. *Nano Lett.* **2014,** 14, 2849-2853.
140. Yabuuchi, N.; Kubota, K.; Dahbi, M.; Komaba, S. *Chem. Rev.* **2014,** 114, 11636-11682.
141. Moreau, P.; Guyomard, D.; Gaubicher, J.; Boucher, F. *Chem. Mater.* **2010,** 22, 4126-4128.
142. Berthelot, R.; Carlier, D.; Delmas, C. *Nat. Mater.* **2011,** 10, 74-80.
143. Naeyaert, P. J. P.; Avdeev, M.; Sharma, N.; Yahia, H. B.; Ling, C. D. *Chem. Mater.* **2014,** 26, 7067-7072.
144. Ong, S. P.; Chevrier, V. L.; Hautier, G.; Jain, A.; Moore, C.; Kim, S.; Ma, X.; Ceder, G. *Energy Environ. Sci.* **2011,** 4, 3680-3688.
145. Islam, M. S.; Fisher, C. A. J. *Chem. Soc. Rev.* **2014,** 43, 185-204.
146. Park, M.; Zhang, X.; Chung, M.; Less, G. B.; Sastry, A. M. *J. Power Sources* **2010,** 195, 7904-7929.
147. Luo, J.; Zhang, W.; Yuan, H.; Jin, C.; Zhang, L.; Huang, H.; Liang, C.; Xia, Y.; Zhang, J.; Gan, Y.; Tao, X. *ACS Nano* **2017,** 11, 2459-2469.
148. Schmidt, C.; Rosen, M. E.; Caplan, D. F.; Pines, A.; Quinton, M. F. *J. Phys. Chem.* **1995,** 99, 10565-10572.
149. Wang, C.; Zhang, X.; Xu, Z.; Sun, X.; Ma, Y. *ACS Appl. Mater. Interfaces* **2015,** 7, 19601-19610.
150. Beneš, L.; Melánová, K.; Trchová, M.; Čapková, P.; Matějka, P. *Eur. J. Inorg. Chem.* **1999,** 1999, 2289-2294.
151. Yan, B.; Liao, L.; You, Y.; Xu, X.; Zheng, Z.; Shen, Z.; Ma, J.; Tong, L.; Yu, T. *Adv. Mater.* **2009,** 21, 2436-2440.
152. Trchová, M.; Čapková, P.; Matějka, P.; Melánová, K.; Beneš, L.; Uhlířová, E. *J. Solid State Chem.* **1999,** 148, 197-204.
153. Kresse, G.; Hafner, J. *Phys. Rev. B* **1993,** 47, 558-561.
154. Henkelman, G.; Uberuaga, B. P.; Jónsson, H. *J. Chem. Phys.* **2000,** 113, 9901-9904.

155. Bediako, D. K.; Rezaee, M.; Yoo, H.; Larson, D. T.; Zhao, S. Y. F.; Taniguchi, T.; Watanabe, K.; Brower-Thomas, T. L.; Kaxiras, E.; Kim, P. *Nature* **2018,** 558, 425-429.
156. Xia, Y.; Mathis, T. S.; Zhao, M.-Q.; Anasori, B.; Dang, A.; Zhou, Z.; Cho, H.; Gogotsi, Y.; Yang, S. *Nature* **2018,** 557, 409-412.